Coupled Resonant Coil Sensors for Remote

Passive Monitoring Applications

by

Sharmistha Bhadra

A Thesis submitted to the Faculty of Graduate Studies of

The University of Manitoba

in partial fulfillment of the requirements of the degree of

Master of Science

Department of Electrical and Computer Engineering

University of Manitoba

Winnipeg

Abstract

The thesis describes development and application of coupled resonant coil sensors, which is of growing interest for remote monitoring applications. An interrogation technique, which improves the accuracy and interrogation range of coupled resonant coil sensors, is introduced. The method uses time-domain gating to produce measurements that are dominated by the response of the sensor coil and are immune to surrounding object interference. For application in structural health monitoring a low cost embeddable coupled coil sensor, which is able to monitor the corrosion potential of reinforcement steel is presented. Results of an accelerated corrosion test using the sensor indicate that corrosion potential can be monitored with a resolution less than 10 mV and a sensitivity of 0.76 kHz/mV. The last part describes a coupled-coil pH sensor based on pH electrode potential measurement. A linear response over a 4 to 10 pH dynamic range and 50 kHz/pH sensitivity are achieved with a 0.1 pH resolution and 30 s response time.

Acknowledgement

this thesis to my parents, who never let me lose sight of my goal. I hope my successful

completion of this thesis will make them proud.

Table of Contents

List of Tables

List of Figures

List of Copyrighted Material for which Permission was Obtained

- Andringa, M. M., Neikrik, D. P., Dickerson, N. P., & Wood, S. L. (2005). Unpowered wireless corrosion sensor for steel reinforced concrete. *IEEE Sensors* , (pp. 155-158). Reprinted with permission from IEEE Intellectual Property Rights Office, July 24, 2010. Used in page 75 of this thesis (as Figure 6.8)

- Roctest corrosion sensor. (n.d.). *Concrete corrosion sensor*. Retrieved January 16, 2010, from http://www.roctest.com/modules/AxialRealisation/img_repository/files/documents/SensCore-161010.pdf. Reprinted with permission from Roctest, August 2, 2010. Used in page 74 of this thesis (as Figure 6.7).

- Roctest humidity sensor. (n.d.). *Concrete humidity sensor*. Retrieved November 06, 2009, from http://www.smartec.ch/PDF/SDS%2016.1011%20SensCore%20Humidity%20and%20Temperature%20Sensor.pdf. Reprinted with permission from Roctest, August 2, 2010. Used in page 57 of this thesis (as Figure 5.2).

- Song, H., & Saraswathy, V. (2007). Corrosion monitoring of reinforced concrete structures - a review. *International Journal of Electrochemical Science , 2*, 1-28. Reprinted with permission from M. Antonijevic of International Journal of Electrochemical science, July 22, 2010. Used in pages 66, 67, 68, 69, 73 of this thesis (as Figure 6.1, Figure 6.2, Figure 6.3, Figure 6.4, and Figure 6.6).

- Zheng, Z., Sun, X., & Lei, Y. (2009). Monitoring corrosion of reinforcement in concrete structures via fiber Bragg grating sensors. *Front. Mech. Eng. , 4* (3), 316–319. Reprinted with permission from Springer publishing, July 21, 2010. Used in page 72 of this thesis (as Figure 6.5).

- Wroblewski, W. (2005). *Field effect transistors (FETs) as transducers in electrochemical sensors.* Retrieved May 6, 2010, from http://csrg.ch.pw.edu.pl/tutorials/isfet/. Reprinted with permission from Prof. dr hab. Wojciech Wroblewski, July 23, 2010. Used in page 99 of this thesis (as Figure 7.2).

Nomenclature

RFID: Radio-Frequency Identification

SAW: Surface Acoustic Wave

SHM: Structural Health Monitoring

SNR: Signal to Noise Ratio

μ_0: Permittivity of Free Space

ε_0: Permeability of Free Space

Cl^-: Chloride Ions

OCP: Open Circuit Potential

LPR: Linear Polarization Resistance

CW: Continuous Wave

f_0: Resonant Frequency

Q: Quality Factor

Chapter 1: Introduction

1.1 Motivation and Thesis Overview

Development of sensor technology is of growing interest to researchers. Reduced costs for electronic devices and the possibility of miniaturizing sensor systems have led to an increasing demand for process and condition monitoring in industry, logistics and transportation. As wired sensors need a fixed wired connection between the sensor and the evaluation unit, they are not appropriate for a wide variety of applications, such as testing the environmental conditions inside sealed, opaque containers such as food packages, and biological *in vivo* experiments such as the monitoring of bloodstream chemistry. Therefore wireless sensor technology is rapidly growing. Wireless sensors not only eliminate the cost of wire and wire installation, they also help to gain access to quantities that cannot be measured by other means. For example, long term data monitoring within a living organism can hardly be done with using wires. Moreover, they offer advantages in applications where extreme environmental conditions can be expected.

The current state on wireless sensing technology offers both active and passive wireless sensors. Active sensors can provide relatively long range but require internal batteries. As batteries require frequent replacement, this type of sensor has a short life time and does not afford permanent embedding in a structure. Passive sensors have reduced transmission distances but do not require any local power source [Nowak et al., 2006]. They are very advantageous for applications where changing batteries or

connecting wires between the sensor and the interrogator unit is difficult e.g. health monitoring of civil infrastructure, biomedical and clinical monitoring and environmental sensing. Some of the more widely used wireless passive sensors are magnetoelastic sensor, surface acoustic wave sensor and inductively coupled coil sensor. They are briefly described below.

1.1.1 Magnetoelastic Sensor

Magnetoelastic sensors are typically made of amorphous ferromagnetic ribbons or wires, mostly amorphous iron and nickel-based alloys such as $Fe_{40}Ni_{38}Mo_4B_{18}$ (Metglas brand 2826MB) and $Fe_{81}B_{13.5}Si_{3.5}C_2$ (Metglas 2605SC) [Cai & Grimes, 2000], that have a high mechanical tensile strength (~1000-1700 MPa) and a low material cost, allowing them to be used on a disposable basis. In addition, these Metglas ribbons have a high magnetoelastic coupling coefficient, as high as 0.98 and magnetostriction on the order of 10^{-5} [Hernando et al., 1988], [Modzelewski et al., 1981], [O'Handley, 2000]. The operation of these devices is based on the excitation of a longitudinal elastic wave in the sensor by an externally applied alternating current (AC) magnetic field. As a result of this excitation, the sensor mechanically vibrates at its mechanical resonant frequency. The high magnetoelastic coupling allows efficient conversion between magnetic and elastic energies and vice versa. Through the inverse magnetoelastic effect, this mechanical vibration of the sensor in turn generates a time varying magnetic flux which oscillates at the sensor's mechanical resonance and can be monitored with a pick-up coil. If the frequency of the applied AC magnetic field is equal to the mechanical resonant frequency of the sensor, the conversion of the magnetic energy into elastic energy is maximal. The

sensor is designed in a way so that its mechanical resonance is a function of the parameter of interest such as pressure, temperature, liquid density. So by tracking the mechanical resonant frequency of the sensor, the parameter of interest can be monitored. The time-domain signal from the sensor is converted into the frequency domain by performing a Fast Fourier Transform (FFT), and the resonant frequency is determined. The resonant frequency of the transiently excited sensor can also be determined by counting the zero crossings of the sensor response for a given time period. Alternatively, the magnetoelastic sensors can be interrogated in the frequency domain by sweeping the frequency and recording the measured response amplitude at each incremental frequency [Loiselle & Grimes, 2000], [Grimes et al., 1999], [Grimes et al., 2002]. They have the advantages of not requiring a power source on the sensors, low cost and having higher resistance to environmental moisture. These properties allow them for use in civil engineering and geo-technological applications. Some shortcomings of magnetoelastic sensors are higher power consumption, notice-able sensor errors, hysteresis and nonlinearity [Vojtko, 2007]. Magnetoelastic sensors are used to measure a wide range of environmental parameters including pressure [Kouzoudis & Grimes, 2000], [Grimes, Stoyanov et al., 1999], humidity [Grimes & Kouzoudis, 2000], [Jain et al., 2000], temperature [Jain et al., 2000], liquid viscosity and density [Grimes et al., 2000], and chemicals such as carbon dioxide [Cai et al., 2000], ammonia [Cai, Jain et al., 2000], and pH [Jain et al., 2001].

1.1.2   Surface acoustic wave RF sensor

The materials commonly employed for SAW devices are quartz (SiO_2), lithiumniobate ($LiNbO_3$), and lithiumtantalate ($LiTaO_3$). New high temperature materials, berlinite ($AlPO_4$), lithium tetraborate ($Li_2B_4O_7$), langasite ($La_3Ga_5SiO_{14}$), and galliumorthophosphate ($GaPO_4$), are applicable up to 1000° C. Due to the high operational frequency and the high dynamic range for the excitation of surface acoustic waves, it is possible to transfer energy to a SAW device using an RF signal. SAW sensors operate from 25 to 500 MHz. A SAW device is connected to an antenna to form a SAW RF sensor for remote measurements. While propagating along the surface the SAW is exposed to the influence of the parameter of interest and hence the responded signal contains information about the parameter of interest. There are two main principles of operation. One of the possibilities is to use a device with one interdigital transducer and reflector. The interdigital transducer is connected to an antenna and can receive the interrogation signal (pulse) and excites a SAW. The SAW excited by the interdigital transducer propagates along the surface of the substrate (e. g. quartz) and is reflected by the reflectors travelling back to the interdigital transducer. The reflected signal is reconverted in an electrical signal by the interdigital transducer and transferred back to the interrogation unit. The space between the interdigital transducer and the reflector is covered by a special coating that reacts with the parameter of interest. As the SAW propagation is affected by this coating, the delay time between the transferred and the received interrogation signal contains the information about the parameter of interest. The other principle of operation is the usage of SAW resonators. Resonators have lower

losses when interrogated and therefore a longer interrogation distance. The resonator type SAW device has one or two interdigital transducers which are placed between two reflectors forming a standing wave. This leads to a resonant behaviour. When the interdigital transducer of a resonator is connected to an antenna, a burst signal can excite the resonator to oscillations. After the interrogation signal is switched off, the resonator will oscillate on its own resonance frequency. The resonator gives this oscillation back to the interrogation unit via the antenna. The surface of the resonator is influenced by using a coating material and a mass loading occurs because of the adsorption or absorption of the material to be measured. Due to the mass loading, the resonant frequency is influenced by material to be measured and thus contains information about it [Pohl, 2000], [Buff, 2002]. The amplitude of the oscillation depends on the frequency inside the burst. The amplitude is the largest when the frequency inside the burst matches the resonance frequency of the resonator. The main advantages of SAW sensors are that they are passive and small in size with a minimal volume of substrate. Due to small size they can response very fast to changes in parameter of interest. The small dimensions also make it possible to get a signal even when only a very small amount of parameter of interest is available. Moreover the SAW will be not influenced by magnetic fields. This makes them suitable for measurements near conductors for high currents or fast alternating currents where other methods fail [Buff, 2002]. The mostly used type of surface acoustic waves in these sensors is the Rayleigh mode wave. One disadvantage of these sensors is that Rayleigh waves are surface-normal waves, making them poorly suited for liquid sensing. When a SAW sensor is contacted by a liquid, the resulting

compressional waves cause an excessive attenuation of the surface wave. SAW RF sensors have been used for a lot of applications such as monitoring the tire pressure as well as the friction between the tire and the road surface [Pohl & Seifert, 1996], monitoring humidity, pressure and position [Smith & Hinson-Smith, 2006].

1.1.3 Inductively coupled coil sensor

Inductively coupled coil sensors operate by using a resonant coil whose resonant frequency (and possibly quality factor) is a function of the measurand. One coil, the sensor coil, is placed in the medium being monitored and the other one is used as an external interrogator coil. The inductive sensor coil is connected in parallel or in series with a capacitive (and possibly resistive) element to form a resonant circuit. The interrogator coil is inductively coupled with the sensor coil and its purpose is to track the changes in the sensor coil's resonant frequency (and possibly quality factor). They are in common use for their important advantages: not requiring a power source on the sensors, simplicity of operation and design, and wide frequency range. Coupled coil sensors are found in many applications e.g., corrosion detection [Andringa et al., 2005], monitoring water content in civil engineering materials [Ong et al., 2008], strain measurement [Butler et al., 2002], moisture measurement [Harpster et al., 2002] and food quality monitoring [Ong et al., 2002].

SAW RF sensors and inductively coupled coil sensors are most commonly used in passive RFID (Radio-frequency identification) tags. RFID is an emerging technology that makes use of wireless communication and has been promoted as the replacement technology for the optical bar-code. The protocol typically covers the 2 mm - 2 m read

range. There are many distinct protocols used in the various RFID systems, some using the lower end of the spectrum (0.14 MHz) and others using the super high frequency (SHF) at 5.875 GHz [Ruiz-Garcia et al., 2009].

The main focus of this research is on inductively coupled coil sensors. Development of coupled coil sensors is of growing interest to researchers for different SHM and biomedical applications. The existing techniques for interrogating these sensors require small interrogation distance for accuracy and are sensitive to background environment. The first part will introduce a new interrogation technique, time-domain gating, which improves the interrogation range with accuracy and eliminates surrounding object interference.

The next part will present a coupled coil sensor for detecting surface corrosion of reinforcement steel. Corrosion of reinforcement steel is the predominant factor for premature deterioration of concrete construction worldwide. Most of the methods for corrosion monitoring require installing analog probes into the concrete. These require inspectors to tour a structure and manually connect a reader into each probe by hand. The demand of having an inspector on site increases the cost and causes safety risk [Song & Saraswathy, 2007]. There is a need for wireless embeddable corrosion monitoring system. Several wireless embeddable corrosion sensors are commercially available. Almost all are based on an active powered wireless communication protocol and thus are expensive [Virginia Technologies, Inc.], [Roctest corrosion sensor]. The sensor presented here is embeddable and simple in design, making it an inexpensive batteryless option for remote long-term monitoring of corrosion state of reinforcement steel.

7

The last part will demonstrate a coupled coil pH sensor based on pH electrode potential measurement. pH is an important chemical parameter that is measured for concrete structures, soil, water, food, blood, urine and related clinical specimen, and many chemical reactions. Improper pH can cause serious consequences in different applications. For example, pH in the blood must be maintained. All other organs and fluids fluctuate in their range in order to keep the blood a strict pH between 7.35 and 7.45 (slightly alkaline). This process is called homeostasis. The body makes constant adjustments in tissue and fluid pH to maintain this very narrow pH range in the blood. If the blood becomes too acidic it takes some of the alkaline forming elements from the enzymes in the small intestine to stay balanced. The small intestine then becomes too acidic to digest foods optimally. The pancreas, gallbladder and liver are then forced to make up for this deficiency in order to metabolize foods properly. This has a direct bearing on metabolic enzyme production, which is literally involved in every biochemical reaction in the body. The result may be lowered immune function, fatigue, hormonal imbalances, absorption and digestive problems, etc.

The most common methods for the measurement of pH are the pH combination electrode and ion sensitive field effect transistor (ISFET). pH combination electrode and ISFET require a direct wired connection to the meter electrically [Reagecon, 2005], [Wroblewski, 2005]. This method is not suitable where electrical connection to the measurement point is impossible or inconvenient, or continuous monitoring is required. Development of wireless passive sensors is important for chemical sensing. Most of the wireless passive pH sensors developed to date are based on pH sensitive polymer. The

common drawbacks of these sensors are the long response time and the highly non-linear response [Horton et al., 2009], [Jain et al., 2001], [Sridhar & Takahata, 2009]. The pH sensor developed in this research has an improved response time and linear response over a wide dynamic range with high sensitivity and resolution. Thus the sensor has the potential to be very useful for long term remote pH monitoring applications.

1.2   Thesis Organization

This thesis is organized as follows:

- Chapter 2 presents the operating principle of coupled coil sensors and the existing interrogation technique for them.

- Chapter 3 introduces the new interrogation technique, time-domain gating. It discusses the theory of a mass-spring-friction second order vibration system, system operation, circuit theory and instrumentation.

- Chapter 4 shows the simulation and experimental results for time-domain gating with a C_P-G_P sensitive sensor. It also presents a comparison of the interrogation range/accuracy between the time-domain gating and the existing interrogation technique, the effect of the surroundings and measurement of ΔC_P and ΔG_P of the sensor.

- Chapter 5 presents a coupled coil sensor for monitoring moisture content inside a remote environment. Importance of measuring moisture content inside civil structures, existing methods for this purpose, and the experiment to measure relative humidity with the sensor are discussed.

- Chapter 6 presents a coupled coil sensor for detecting surface corrosion of reinforcement steel. It discusses the importance of corrosion monitoring, current techniques available for corrosion monitoring, the operation and description of the sensor, DC calibration, accelerated corrosion test and the sensor performance.

- Chapter 7 presents a coupled coil pH sensor based on pH electrode potential measurement. It discusses the importance of pH measurement, current techniques available for pH measurement, the operation and description of the sensor, experiment and the sensor performance.

- Chapter 8 describes the conclusion and future work.

Chapter 2: Coupled Coil Sensor

2.1 Sensor Operation

One type of coupled coil sensor is based on a passive LC coil resonator whose resonant frequency or quality factor is a function of the measurand. In the sensor unit, an inductive coil is connected in parallel with a capacitive element. Fig. 2.1 shows the equivalent circuit diagram of the sensor unit.
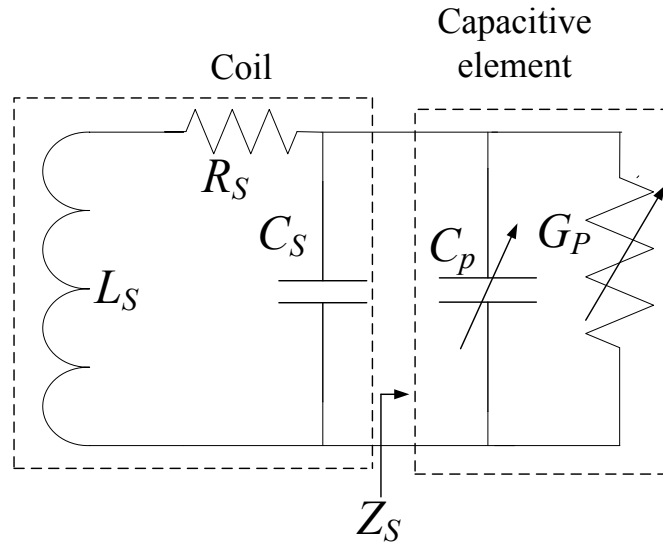
Figure 2.1. Equivalent circuit diagram of the sensor unit.

Here L_S is the coil inductance, R_S is the coil series resistance and C_S is the self capacitance of the coil, C_P is the capacitance of the capacitive element and G_P is the shunt conductance of the capacitive element. R_S and G_P are considered as losses. The capacitive element's impedance is given by

$$Z_s = \left(G_p + j\omega C_p \right)^{-1}. \tag{2.1}$$

Fig. 2.2 shows the equivalent circuit diagram of the sensor unit when coupled to an interrogator coil and a voltage is applied across the interrogator coil.
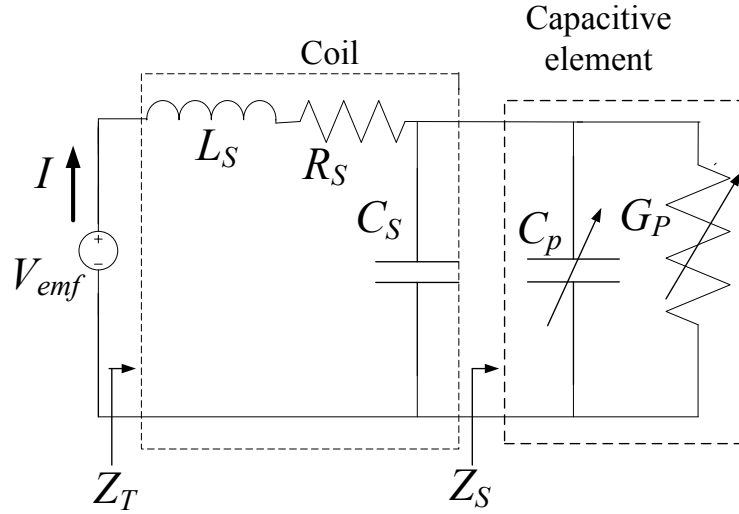
Figure 2.2. Equivalent circuit diagram of the sensor unit when coupled to an interrogator coil.

If losses are small, $G_P << \omega\, C_P$, the total sensor impedance, Z_T, can be approximated by

$$Z_T \cong j\omega L_S + \frac{1}{j\omega\left(C_s + C_p\right)} + R_s + \frac{G_p}{\omega^2\left(C_s + C_p\right)^2} .$$ (2.2)

The imaginary part of Z_T goes to zero when

$$\omega = \frac{1}{\sqrt{L_s\left(C_p + C_s\right)}} \quad \text{only if losses } (R_S,\ G_p) \text{ are small.}$$ (2.3)

This frequency is the resonant frequency, ω_0, of the sensor. If $C_S << C_P$, then eqn. 2.3 is given by

$$\omega_0 = \frac{1}{\sqrt{L_s C_p}} \ .$$
(2.4)

By changing L_S or C_P in response to the change of a measurand and then by sensing the change of resonant frequency, the measurand can be monitored.

Another parameter of interest is the quality factor, Q, of the sensor which can be derived from eqn. 2.2 as

$$Q = \omega_0 \left(\frac{R_s}{L_s} + \frac{G_p}{C_p + C_s} \right)^{-1} \ .$$
(2.5)

Eqn. 2.5 shows that R_S or G_P can be changed in response to the change of the measurand instead of L_S or C_P. In that case the measurand can be monitored by determining the change of sensor's quality factor. The most common technique for monitoring the measurand is changing L_S or C_P with the change of measurand and tracking the change of sensor's resonant frequency.

2.2   Existing Interrogation Techniques for Coupled Coil Sensor

Changes in the sensor coil's resonant frequency and quality factor are most commonly detected remotely by measuring the induced change in the impedance of an interrogator coil inductively coupled to the sensor coil [Nowak et al., 2006] as shown in Fig. 2.3.
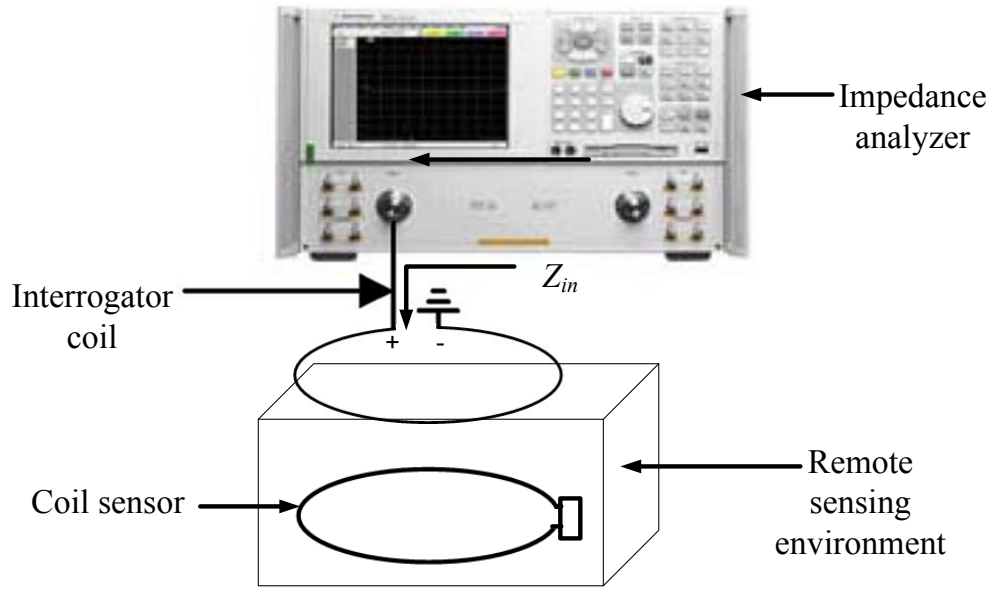
Figure 2.3. Impedance measurement interrogation technique for coupled coil sensor.

2.2.1 Impedance measurement circuit Model

Fig. 2.4 shows the equivalent circuit of the impedance measurement system. In this circuit model, the mutual capacitance between the coils is very small and is neglected. The interrogator coil is designed so that the self-resonant frequency is much higher than that of the sensor.
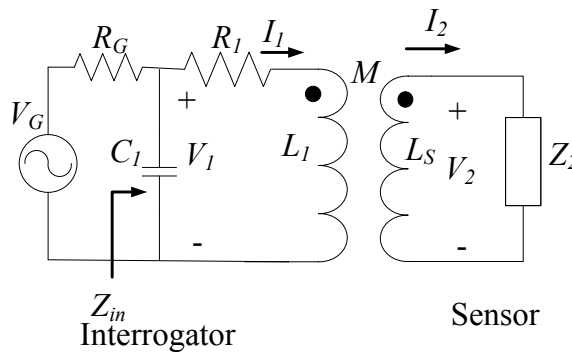
Figure 2.4. Equivalent circuit of impedance measurement system.

14

The impedance analyzer source, V_G, produces a time-varying current, I_1, which passes through the interrogator coil, L_1. This current generates a time-varying magnetic flux which links the loop in the sensor coil, L_s. According to Lenz's law, a resulting current, I_2 is induced in the sensor loop given by

$$I_2 = \frac{-j\omega M}{Z_2 + j\omega L_S} I_1 = \frac{-j\omega M}{Z_T} I_1,$$

(2.6)

where ω is the source frequency, $Z_T = Z_2 + j\omega L_S$ is the total sensor impedance, $Z_2 = R_S + (1/(j\omega(C_S + C_P) + G_P))$, and M is the mutual coupling between the sensor coil and the interrogator coil. For $R_G << 1/j\omega C_1$, C_1 is neglected and the voltage across the interrogator coil, V_1 is given by

$$V_1 = R_1 + j\omega L_1 I_1 + \frac{\omega^2 M^2}{Z_T} I_1.$$

(2.7)

The current through the interrogator coil, I_1, is given by

$$I_1 = \frac{1}{R_G + R_1 + j\omega L_1 + \frac{\omega^2 M^2}{Z_T}} V_G, \quad I_1 = \frac{Z_T}{Z_T Z_R + \omega^2 M^2} V_G,$$

(2.8)

where $Z_R = R_G + R_1 + j\omega L_1$. Further, the impedance seen by the impedance analyzer Z_{in}, is given from eqn. 2.7 as

$$Z_{in} = R_1 + j\omega L_1 + \frac{\omega^2 M^2}{Z_T}.$$

(2.9)

From the relationship above, it appears that the sensor interaction can be seen as a load ΔZ_{in} placed in series with the interrogator coil where

$$\Delta Z_{in} = \frac{\omega^2 M^2}{Z_T} \tag{2.10}$$

2.2.2 Drawbacks

This technique is affected by the response of the interrogator coil and objects in the surrounding environment. For example, if a section of rebar is placed in close proximity to the interrogator, the interrogator coil impedance, $(R_1 + j\omega L_1)$ in eqn. 2.9, increases which increases the background Z_{in}. As the interrogation distance increases, the response from the sensor coil decreases rapidly and only the interrogator coil self impedance, which is sensitive to the surrounding environment, dominates. If the section of rebar is placed next to the sensor, Z_T in eqn. 2.9 is changed which results in shifting the resonant frequency. Thus, this interrogation technique requires a small separation distance between the sensor and the interrogator, and is sensitive to the surrounding environment.

2.2.3 Implementation

For the impedance measurement interrogation technique the response spectrum was measured with an Agilent 4294A impedance analyzer. The interrogator coil was constructed of insulated wire of 1.2 mm diameter and contains 5 turns of 5.1 cm diameter, producing measured values L_1=2.35 μH, R_1=334.13 mΩ and a self-resonant frequency, f_{res}=28.32 MHz. In this case, the resonant frequency was obtained from the maximum of the real part of the impedance. To remove the impedance of the interrogator coil, a background subtraction, using the measured impedance of the interrogator coil

when the sensor was absent, was implemented prior to measuring the sensor response (Ong et al., 2008). Fig. 2.5 and Fig. 2.6 show the experimental setup and impedance frequency response for a test coil sensor (L_S=65.48 µH, R_S= 11.72 Ω , C_S=0.32 pF, C_P=32.9 pF and G_P=195.30 nS), respectively. In this case the distance between the sensor coil and the interrogator coil was R=10cm, the bandwidth of the impedance analyzer was 39.8 Hz and the SNR was 53.19 dB.
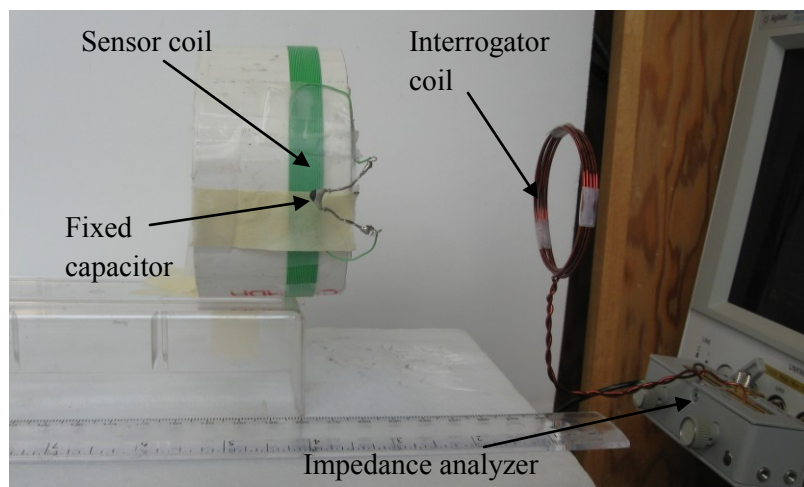
Figure 2.5. Experimental setup for test coil sensor using impedance measurement technique.
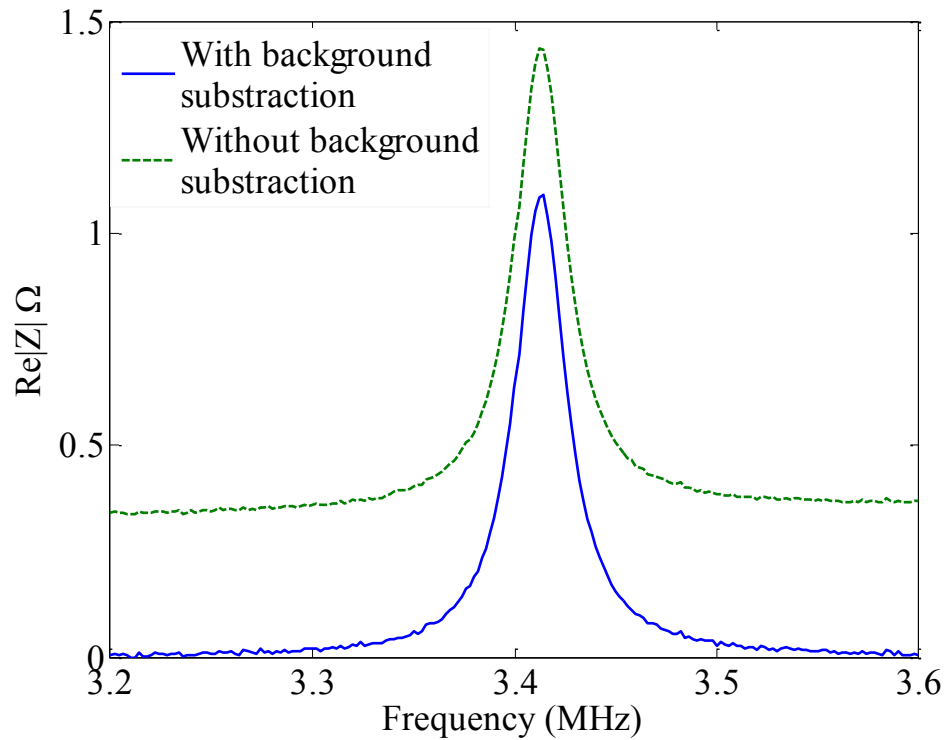
Figure 2.6. Impedance frequency response for test coil sensor.

From this impedance frequency response, the resonant peak was determined using a quadratic curve-fitting algorithm. The accuracy of this curve fitting algorithm depends on the frequency step and the SNR. For greater accuracy, a smaller frequency step and higher SNR are needed [Robinson & Clegg, 2005]. The MATLAB® program in Appendix A.1 implements this quadratic curve fitting technique.

Chapter 3: Time-domain Gating

3.1 Introduction

This is an interrogation method which makes use of time-domain gating to eliminate the response from the interrogator coil, the exciting signal and surrounding objects. In this technique the sensor is first excited by a sine wave pulse and then the transient response, or ring-down at the natural frequency of the sensor resonator, from the sensor is monitored and analyzed. This results in a measurement dominated by the response of the sensor coil, enabling detection of the sensor's resonant frequency far more precisely at an extended separation distance. A sine wave pulse excitation is used to excite the sensor into the resonant state since near the resonant frequency, it transfers more energy than using an impulse to excite the sensor. Exciting the sensor with an interrogation pulse and then analyzing the transient response of the sensor were previously used as an interrogation technique for a wireless corrosion sensor operating at radio frequency [Wang, 2008] and as a rapid method of determining resonant frequency and quality factor of magnetoelastic sensors [Zeng et al., 2002], [Zeng & Grimes, 2004].

3.2 Mass-Spring-Friction Second Order System Model

In time-domain gating the coupled resonant coil sensor can be modeled as an equivalent mass-spring-friction second order vibration system described by [Zeng et al., 2002], [Zeng & Grimes, 2004]

$$m\frac{d^2y(t)}{dt^2} + c\frac{dy(t)}{dt} + ky(t) = f(t), \qquad (3.1)$$

where m is the mass, c is the friction coefficient, k is the spring constant, $y(t)$ is the displacement, and $f(t)$ is the applied force. Eqn. 3.1 can be rewritten as

$$\frac{d^2y(t)}{dt^2} + 2\zeta\omega_n\frac{dy(t)}{dt} + \omega_n^2 y(t) = \omega_n^2 x(t), \qquad (3.2)$$

where $\omega_n = \sqrt{k/m}$ is the natural frequency, $\zeta = c/2m\omega_n$ is the damping factor, and $x(t) = f(t)/k$ is the external excitation. Let $X(s)$ and $Y(s)$ be the Laplace transforms of $x(t)$ and $y(t)$, respectively. From the Laplace transform of eqn. 3.2 we get

$$Y(s) = \frac{\omega_n^2 X(s)}{s^2 + 2\xi\omega_n s + \omega_n^2} + \frac{y'(0) + (s + 2\xi\omega_n)y(0)}{s^2 + 2\xi\omega_n + \omega_n^2}. \qquad (3.3)$$

The characteristic equation can be derived as

$$s^2 + 2\zeta\omega_n s + \omega_n^2 = 0. \qquad (3.4)$$

For $x(t>0)=0$, eqn. 3.3 can be written as

$$Y(s) = \frac{y'(0) + (s + 2\xi\omega_n)y(0)}{s^2 + 2\xi\omega_n + \omega_n^2}. \qquad (3.5)$$

For a damped oscillatory sensor ($0<\zeta<1$), the damped oscillation is given by

$$y(t) = A\exp(-\zeta\omega_n t)\cos(\omega_d t - \phi), \qquad (3.6)$$

where,

$$A = \sqrt{y(0)^2 + \left(\frac{\xi\omega_n y(0) + y'(0)}{\omega_d}\right)^2} . \tag{3.7}$$

$$\phi = \tan^{-1}\frac{\xi\omega_n y(0) + y'(0)}{\omega_d y(0)} . \tag{3.8}$$

A, ϕ, and ω_d are the amplitude, phase angle and frequency of the damped oscillation respectively. ω_d and ω_n are related by

$$\omega_d = \sqrt{1-\zeta^2}\,\omega_n . \tag{3.9}$$

The quality factor, Q is related to the damping factor, ζ by

$$Q = \frac{1}{2\zeta\sqrt{1-\zeta^2}} . \tag{3.10}$$

For a small damping factor ($Q \gg 1$, $\zeta \ll 1$),

$$\omega_d \cong \omega_n \cong \omega_0 . \tag{3.11}$$

$$Q = \frac{\omega_n}{2\tau} , \tag{3.12}$$

where $\tau = \zeta\omega_n$ is the time constant of the exponentially decaying sinusoid. For a sensor with small damping factor, ω_d will be close to the resonant frequency, ω_0 of the sensor. Therefore, the transient response from the sensor decays exponentially with a time constant, τ and oscillates at the resonant frequency, ω_0 of the sensor. Fig. 3.1 and Fig. 3.2 shows equivalent circuit model and the transient response from a test coil sensor

21

(L_S=65.48 μH, R_S= 11.72 Ω, C_S=0.32 pF, C_P=32.9 pF and G_P=195.30 nS), respectively. The sensor coil was excited by a step-function sinusoid $x(t)=V_{amp}sin(\omega_0 t)\ u(-t)$. From the equivalent circuit model the parameters of mass-spring-friction second order vibration system were extracted as m=65.48x10^{-6}H, k=3.01x10^{10}F^{-1}, ζ=4.311x10^{-3}, ω_n=2.1441x10^7 rad, Q=115.98. The transient response from the sensor was observed with an oscilloscope. An exponentially decaying sinusoid ($Ae^{-t/\tau}\ sin(2\pi f_0+\phi)$) was fitted to this received signal where, A=0.0229V, τ=1.1x10^{-5}s, f_0=3.4125x10^6 Hz, and ϕ=0.86 rad. This yields a Q=117.92, and ω_0=2.1441x10^7 rad.
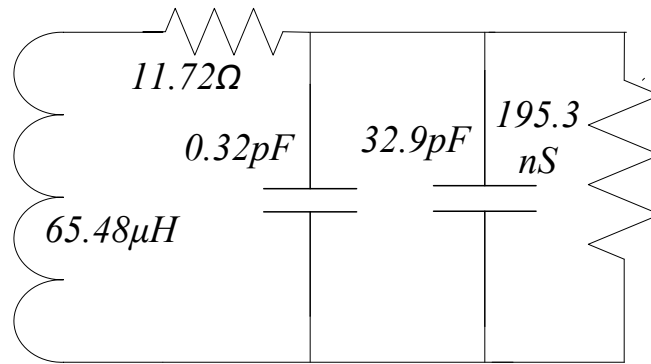
Figure 3.1. Equivalent circuit model of the sensor coil.
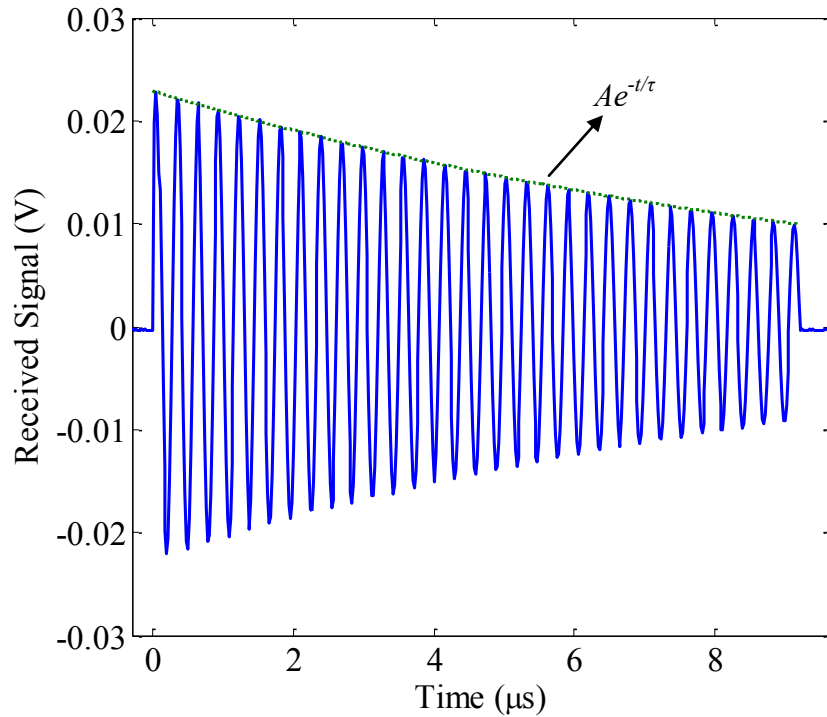
Figure 3.2. Transient response from the test coil sensor.

3.3 Time-Domain Interrogation System Description

A block diagram of the time-domain gating system is shown in Fig. 3.3. During operation, the interrogator first energizes the sensor through inductive coupling between the interrogator coil and the sensor coil. This is the transmit mode (with SW1 and SW3 set to drive the interrogator coil) at frequency ω. After enough time has elapsed to allow the induced energy in the sensor coil to reach equilibrium, the system switches to the receive mode. Here the sensor excitation is switched off using SW1 and SW3 and energy stored in the sensor is coupled back from the sensor to the interrogator. A delay is introduced when the system switches from the transmit mode to receive mode to eliminate the effects of unwanted reflections from objects in the environment and to

dampen the transient response of the interrogator coil. This is done using SW2 where a short delay related to the Q of the interrogator coil is used. Both SW2 and SW3 are used to isolate the signal generator in the receive mode. The received signal is an exponentially decaying sinusoidal signal that oscillates at the damped oscillation frequency of the sensor. The rate of decay of the received signal depends on the quality factor of the sensor. The amplitude of the received signal depends on the excitation frequency. The amplitude is the largest when the excitation frequency, ω matches the resonant frequency of the sensor. By monitoring the received signal on an oscilloscope both ω_0 and τ can be measured. Alternatively, by sweeping the frequency of the exciting signal and monitoring the maximum amplitude of the received signal, the resonant frequency of the sensor can be determined.
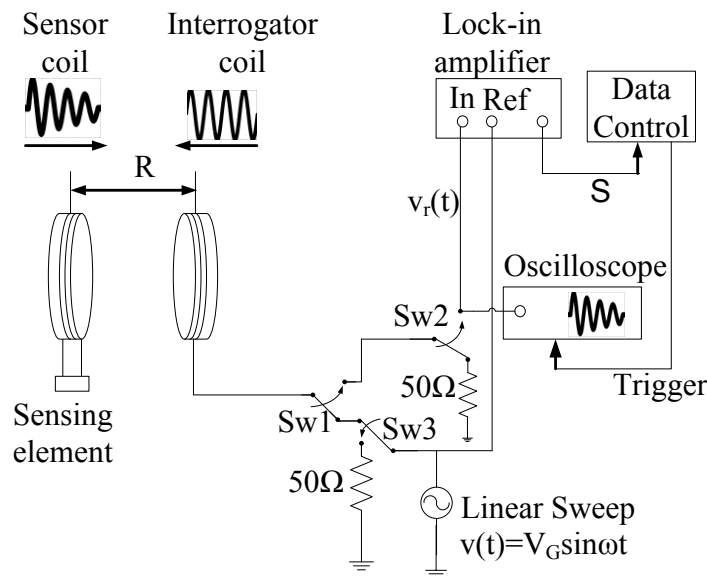
Figure 3.3. Block diagram of time-domain gating system.

3.4 Equivalent Circuit Model
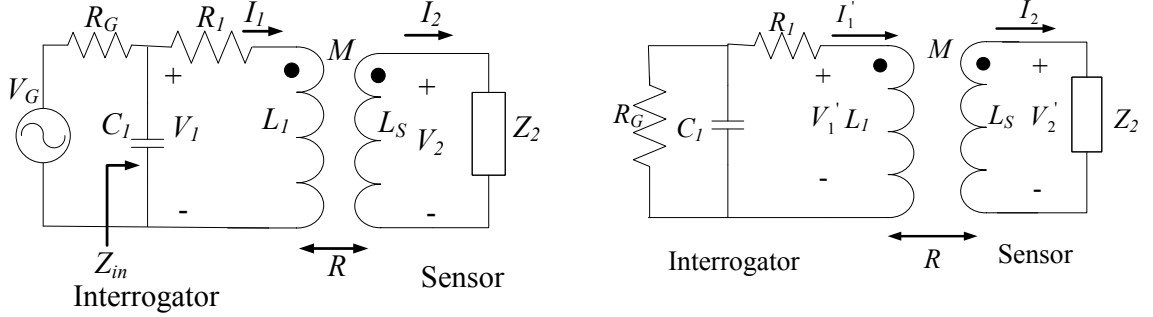
Figure 3.4. Transmit mode equivalent circuit. **Figure 3.5.** Receive mode equivalent circuit.

Phasor analysis will be used to determine the amplitude of the received signal from the sensor. Fig. 3.4 and Fig. 3.5 show the equivalent circuits of the system in transmit mode and receive mode, respectively. In these circuit models, the mutual capacitance between the coils is very small and is neglected. The interrogator coil is designed so that the self-resonant frequency is much higher than that of the sensor and for $R_G \ll 1/j\omega C_1$, C_1 is neglected. The interrogator source, V_G, produces a time-varying current, I_1, which passes through the interrogator coil, L_1. This current generates a time-varying magnetic flux which links the loop in the sensor coil, L_s. Using Lenz's law, a resulting current, I_2, is induced in the sensor loop given by

$$I_2 = \frac{-j\omega M}{Z_2 + j\omega L_S} I_1 = \frac{-j\omega M}{Z_T} I_1, \tag{3.13}$$

where ω is the source frequency, $Z_T = Z_2 + j\omega L_S$ is the total sensor impedance. For a sensor as described by Fig. 2.1, $Z_2 = R_S + (1/(j\omega(C_S + C_P) + G_P))$. Here M is the mutual coupling

25

between the sensor coil and the interrogator coil. As the self capacitance, C_1, of the interrogator coil is very small, the voltage across the interrogator coil, V_1 is given by

$$V_1 = R_1 + j\omega L_1 I_1 + \frac{\omega^2 M^2}{Z_T} I_1.$$

(3.14)

The current through the interrogator coil, I_1, is given by

$$I_1 = \frac{1}{R_G + R_1 + j\omega L_1 + \frac{\omega^2 M^2}{Z_T}} V_G, \quad I_1 = \frac{Z_T}{Z_T Z_R + \omega^2 M^2} V_G,$$

(3.15)

where $Z_R = R_G + R_1 + j\omega L_1$ is the interrogator impedance. Further, the impedance seen by the source, Z_{in}, is given from eqn. 3.14 as

$$Z_{in} = R_1 + j\omega L_1 + \frac{\omega^2 M^2}{Z_T}.$$

(3.16)

When the interrogator switches to receive mode, the current induced in the sensor coil oscillates near its resonant frequency, ω_0, and decays with time constant τ. Provided $1/\tau << \omega_0$ (or $Q >> 1$) for the sensor and the delay between transmit and received mode is small, phasor analysis can be continued. The current passing through the sensor, I_2', when the excitation is turned off is approximated as

$$I_2' \approx I_2.$$

(3.17)

Referring to Fig. 3.4, the current induced in the interrogator coil, I_1', will be

$$I_1' = \frac{-j\omega_0 M}{R_G + R_1 + j\omega_0 L_1} I_2' = \frac{-j\omega_0 M}{Z_R|\omega_0} I_2'. \tag{3.18}$$

In the receive mode, the voltage developed at the interrogator coil, V_1', can be expressed by combining eqns. 3.13, 3.17 and 3.18 as

$$V_1' = R_G I_1' = \frac{\omega_0 \omega M^2 R_G}{Z_T Z_R|\omega_0} I_1. \tag{3.19}$$

Combining eqns. 3.15 and 3.19 then yields the received signal (at frequency ω_0)

$$V_1' = \frac{\omega_0 \omega M^2 R_G}{(Z_T Z_R + \omega^2 M^2) Z_R|\omega_0} V_G. \tag{3.20}$$

Under small coupling assumption

$$\left(\frac{\omega^2 M^2}{Z_T|\omega} << Z_R|\omega\right) \text{ then } V_1' \cong \frac{R_G V_G}{Z_R|\omega_0 Z_R|\omega}\left(\frac{\omega\omega_0 M^2}{Z_T|\omega}\right). \tag{3.21}$$

V_1' is maximum when $\omega \sim \omega_0$ and $|Z_T|\omega_0|$ is minimum. In order to determine the resonant frequency, ω_0, the source frequency, ω, is swept near ω_0 and the maximum received signal, V_1', is obtained using a peak fitting algorithm.

The signal from the sensor in the receive mode always oscillates at the resonant frequency, ω_0, of the sensor, but the lock-in amplifier in Fig. 3.3 is locked to the exciting signal's frequency, ω. Thus, the detected signal, S, as a function of frequency is maximized when $\omega = \omega_0$. However, the response does not directly provide the Q of the sensor. To obtain the Q, the received signal in the time-domain is observed using an

oscilloscope and fitted with a function of the form $Ae^{-t/\tau} \sin(2\pi f_0 + \phi)$ with unknown parameters A, τ, f_0, and ϕ. From τ and f_0, Q is determined using eqn. 3.12.

3.5   Coil Modeling and Signal Vs Distance

From eqn. 3.20, it can be seen that for a fixed exciting frequency the signal from the sensor under the small coupling condition, $Z_T Z_R >> \omega^2 M^2$, will be proportional to M^2. Thus the mutual inductance, M of a coupled coil system is of interest. The self inductance, L, of any coil can be approximated in terms of the loop radius, r, the wire radius, r_w, and the number of turns, n, as [Tesche, Ianoz, & Karlsson, 1997]

$$L = n^2 \mu_0 \sqrt{r(r - r_w)}\left[\left(\frac{2}{k} - k\right)K(k) - \frac{2}{k}E(k)\right], \qquad (3.22)$$

where

$$k^2 = \frac{4r(r - r_w)}{(2r - r_w)(2r - r_w)}. \qquad (3.23)$$

$K(.)$ and $E(.)$ are the complete elliptic integrals, defined as

$$K(k) = \int_0^{\pi} \frac{d\phi}{\sqrt{1 - k^2 \sin^2 \phi}}. \qquad (3.24)$$

$$E(k) = \int_0^{\pi} \frac{d\phi}{\sqrt{1 - k^2 \sin^2 \phi}}. \qquad (3.25)$$

When the sensor coil is constructed, first the range of resonant frequencies of the sensor is chosen. The range of capacitance value of the capacitive element is known. From the

resonant frequency and capacitance value range, the sensor coil desired inductance is found. Generally the resonant frequency of the interrogator is much higher than that of the sensor. Once the resonant frequency of the interrogator coil is chosen, the desired inductance of the coil is found from the resonant frequency (considering the capacitance is negligible). After the desired inductance is found for the coils, the designer makes decision on number of turns, radius of the wire and radius of the coil to achieve it according to eqn. 3.22. Decisions on number of turns, radius of the wire and radius of the coil are influenced by application area of the sensor.

For two concentric coils, the mutual coupling, M, can be expressed in terms of separation distance between the centers of two coils, R, the loop radius of the interrogator coil, r_1, the number of turns of the interrogator coil, n_1, the loop radius of the sensor coil, r_2, and the number of turns of the sensor coil, n_2, as [Tesche, Ianoz, & Karlsson, 1997]

$$M = n_1 n_2 \mu_0 \sqrt{r_1 r_2} [(\frac{2}{k_1} - k_1) K(k_1) - \frac{2}{k_1} E(k_1)], \tag{3.26}$$

where

$$k_1^{\,2} = \frac{4 r_1 r_2}{R^2 + (r_1 + r_2)^2}. \tag{3.27}$$

When the coils are separated by a large distance, $(r_1+r_2)<<R$, eqn. 3.25 can be expressed by

$$M = \frac{n_1 n_2 \mu_0 \pi r_1^{\,2} r_2^{\,2}}{2 R^3}. \tag{3.28}$$

From eqn. 3.28 it can be seen that

$$M \propto \frac{1}{R^3}.$$

(3.29)

Eqn. 3.29 indicates that the path loss of the transmit-receive coupled coil system is proportional to $V_I^{'}/V_G \propto 1/R^6$ and is thus expected to decrease rapidly with distance.

3.6 Instrumentation

A photograph of the time-domain gating interrogation system is shown in Fig. 3.6. The interrogator coil used in our test system was the same as the interrogator coil described in section 2.2.3. A programmable signal generator (Stanford Research Systems DS345) was used to provide a swept frequency signal to the interrogator coil. High isolation bi-directional absorptive SPDT switches (ZASW-2-50DR+) were used for the switches. Switching between the transmit and receive mode was done by these switches. Connection layout for the switches is shown Fig. 3.7.
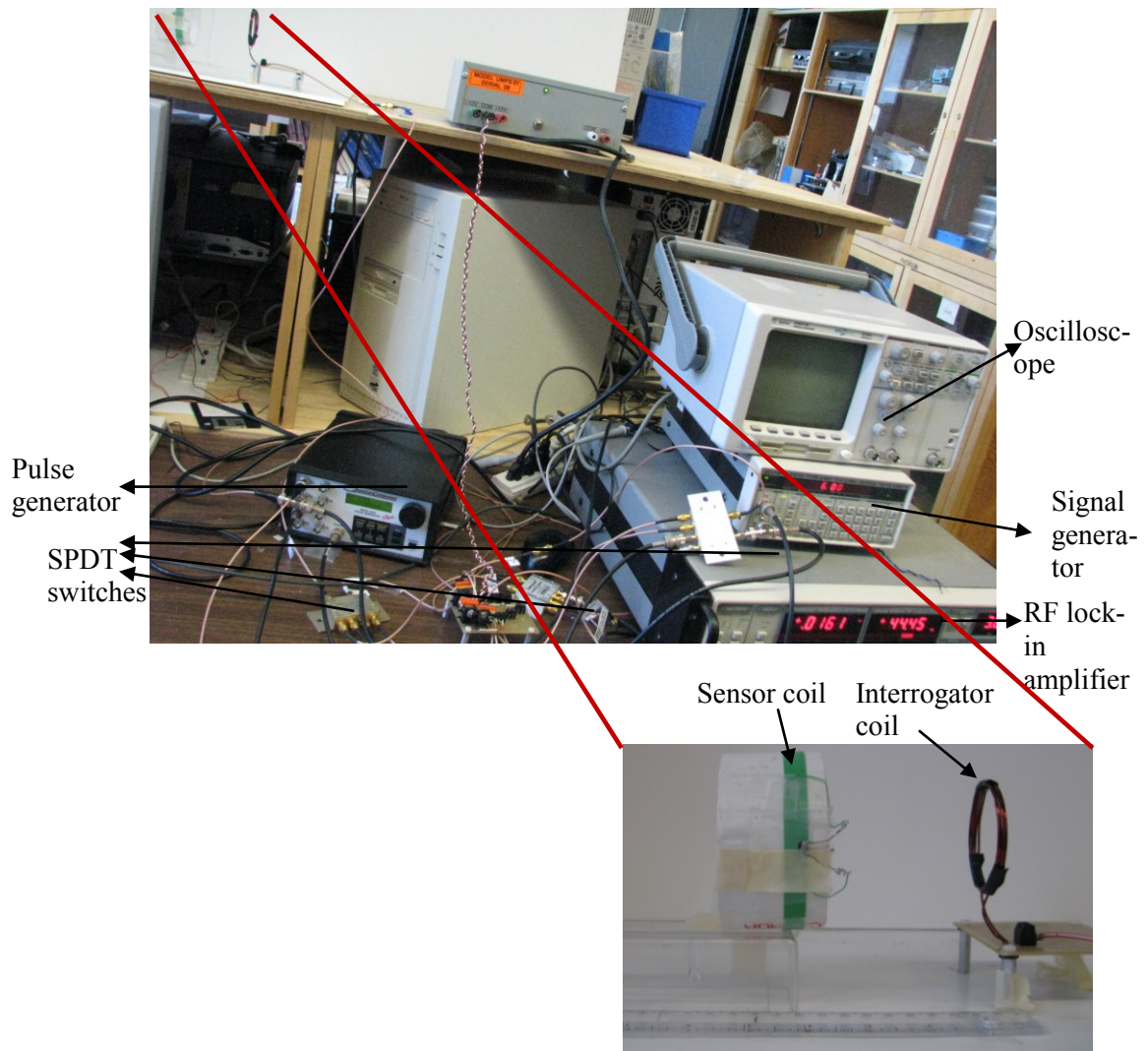
Figure 3.6. Instrumentation for time-domain gating technique.
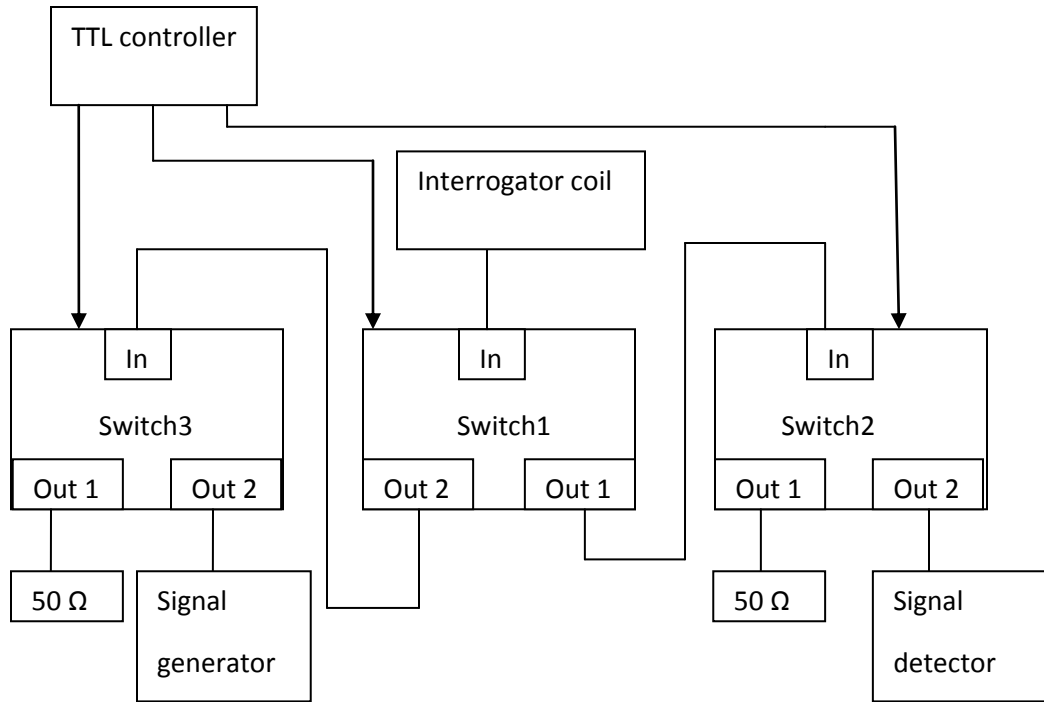
Figure 3.7. Connection layout for the switches.

A pulse generator (Quantum Composers Model 9618) provided the required controlling signals for these switches. The controlling signals are shown in Fig. 3.8. Fig. 3.9 and Fig. 3.10 shows examples of voltage signal across the sensor coil and the detected signal across the detector, respectively.
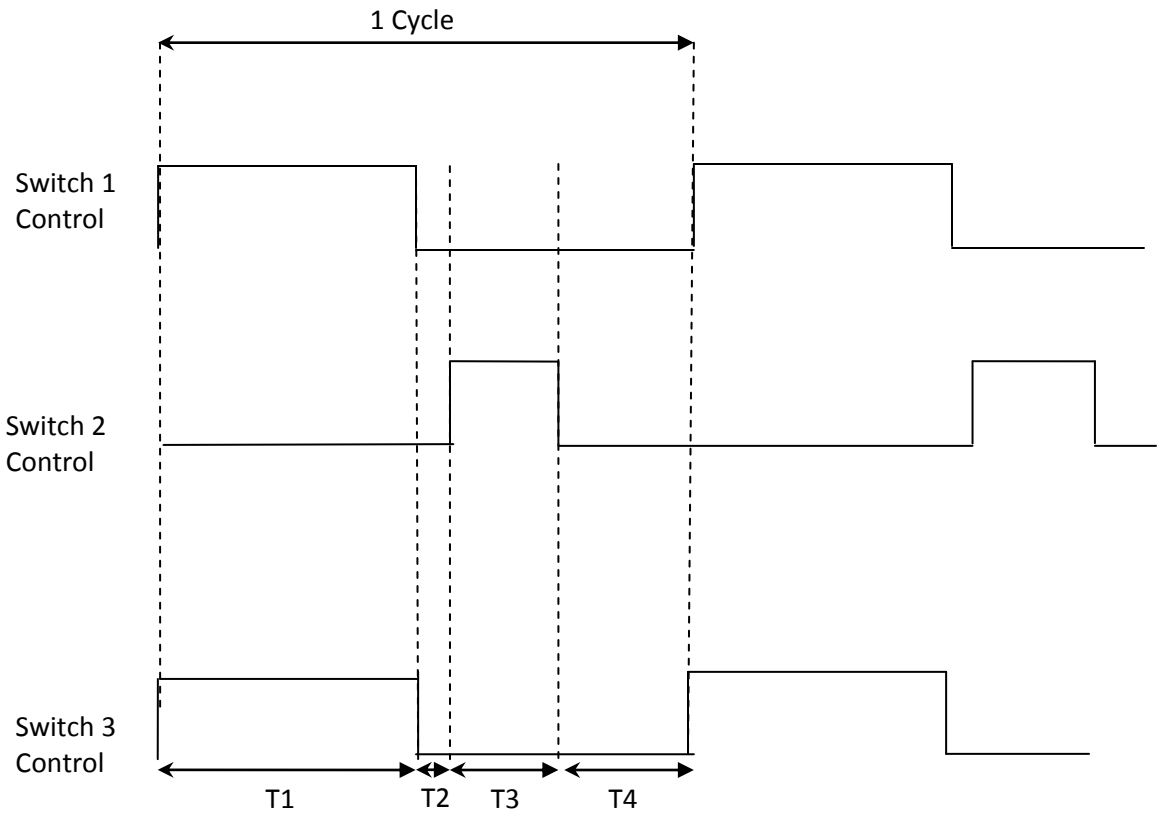
Figure 3.8. Controlling signals for the switches.
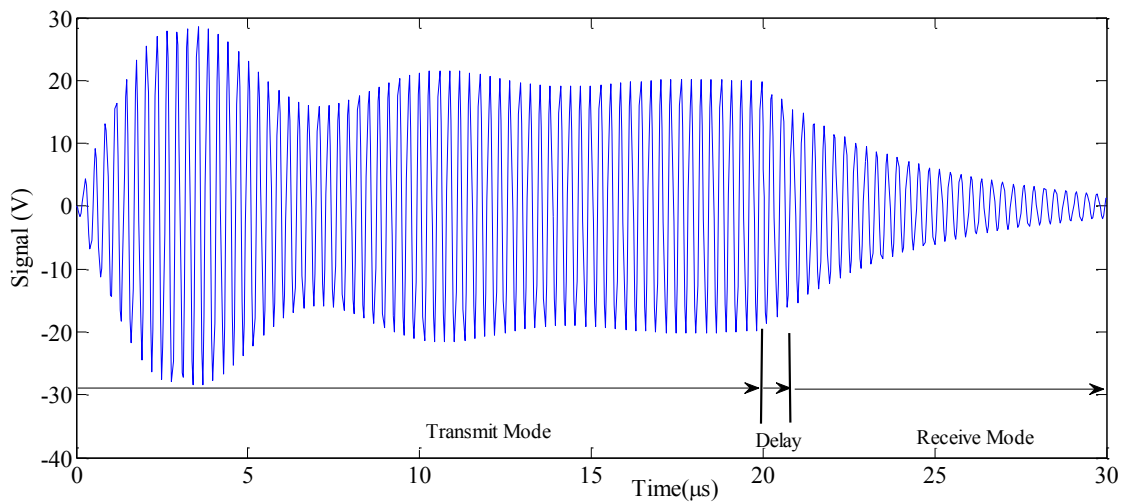
Figure 3.9. Example of voltage signal across the sensor coil.
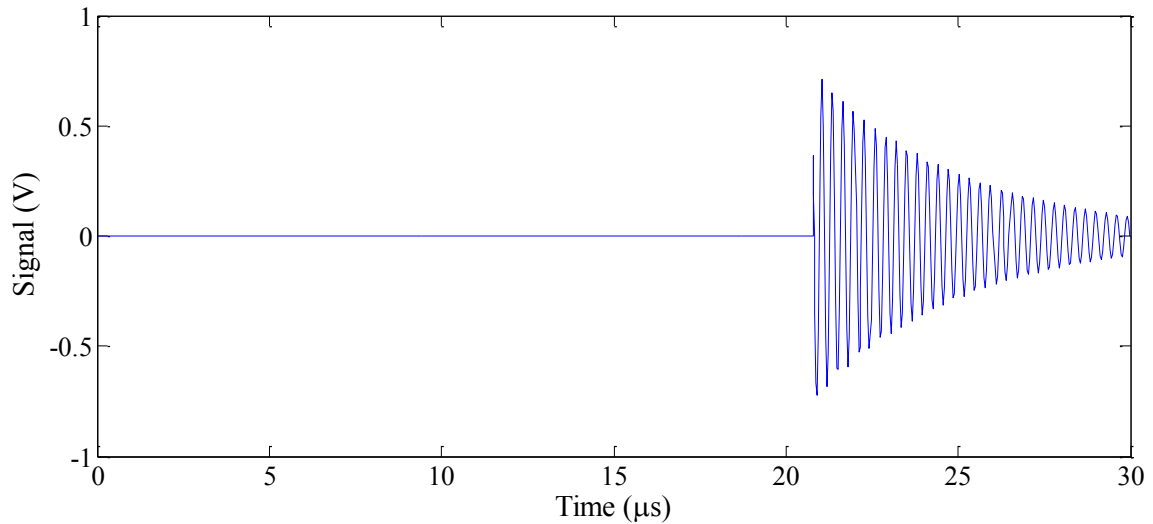
Figure 3.10. Example of detected signal across the detector.

The system is in transmit mode for T1 seconds and in receive mode for T3 seconds. The delay between the transmit and receive mode is T2 seconds. The transmit-receive cycle is repeated in every (T1+T2+T3+T4) seconds. An RF lock-in amplifier (Stanford Research Systems SR844) was used as the detector. The time-domain received signal was also observed with an Agilent 54621A oscilloscope. A computer program, developed in LabVIEW® 7.1, controlled the swept frequency of the signal generator, and recorded the output from the lock-in-amplifier through the General Purpose Interface Bus. The user manual to use this program is presented in Appendix B.1. Sweeping the frequency and measuring the response, S, the resonant peak of the sensor was determined using a quadratic curve-fitting algorithm (Robinson & Clegg, 2005). This quadratic curve fitting technique was implemented using a MATLAB® program in Appendix A.1. In all tests the sensor coil center was aligned concentrically with that of the interrogator coil to get the best response. In chapter 4, results for a specific test coil sensor is given.

34

Chapter 4: C_P-G_P Sensitive Sensor

The sensor coil was a simple parallel LC circuit including parasitic. It was used to test the theories of time-domain gating method established in chapter 3 and compare the time-domain gating method with impedance measurement technique. Tests were also done to measure change in f_0 and Q with the time-domain gating method by changing the C_P and G_P of the sensor.

4.1 Description of the Sensor

A simple test sensor coil was made of wire of 0.55 mm diameter and contains 19 turns of 8.4 cm diameter, producing L_S=65.48 µH, R_S= 11.72 Ω and C_S=0.32 pF. These values were measured using an Agilent parameter analyzer. This coil was connected in parallel with a fixed capacitor of C_P=32.9 pF and G_P=195.30 nS. The theoretical values for f_0 = 3.4124 MHz and Q=115.98 were found using eqn. 2.3 and eqn. 2.5 respectively. The coil sensor is shown in Fig. 4.1. The sensor coil was energized for T1=20 µs in the transmit mode. A delay of T2=0.8 µs was introduced between the transmit and receive mode. The signal from the sensor was received for T3=9.2 µs. The period for this transmit- receive sequence was T1+T2+T3+T4=40 µs. For the tests in this chapter the same interrogator coil described in section 2.2.3 was used where L_I=2.35 µH, R_I=0.334 Ω, C_I=13.43 pF.
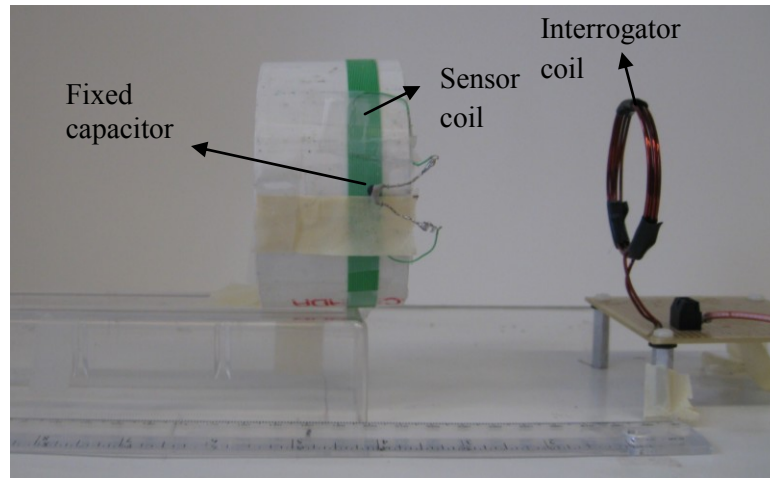
Figure 4.1. C_P-G_P sensitive coil sensor.

4.2 Pspice™ Simulation of Time-domain Gating

The sensor was simulated for time-domain gating system using PSpice™ student version. Lumped element inductors, capacitors, resistors were used to model the coil and the capacitor. Timing was done using voltage controlled switches. The mutual inductive coupling between the coils was set to M=0.17. The circuit schematic is shown in Fig. 4.2. Fig. 4.3 and Fig. 4.4 show the simulated voltage across the sensor coil for source frequencies, f= 3.4125 MHz and f= 1.7 MHz, respectively. From the simulation results it can be seen that for either excitation frequency the signal from the sensor in the receive mode is an exponentially decaying signal which oscillates near the resonant frequency of the sensor. Thus the simulation matches the theory established in section 3.2. However, the amplitude is much larger when $f{\sim}f_0$. Fig. 4.5 and Fig. 4.6 show the simulated voltage across the interrogator coil for source frequencies, f= 3.4125 MHz and f= 1.7 MHz, respectively. The received signal from the sensor in receive mode for different source

frequencies was detected using a lock-in amplifier model. The model was developed using MATLAB®/Simulink by Predrag Drljaca and is available for downloading in MATLAB Central file exchange website [MathWorks, 2002. The Simulink schematic of the model is shown Appendix A.3. Fig. 4.7 shows the spectrum obtained using the lock-in amplifier as a detector.
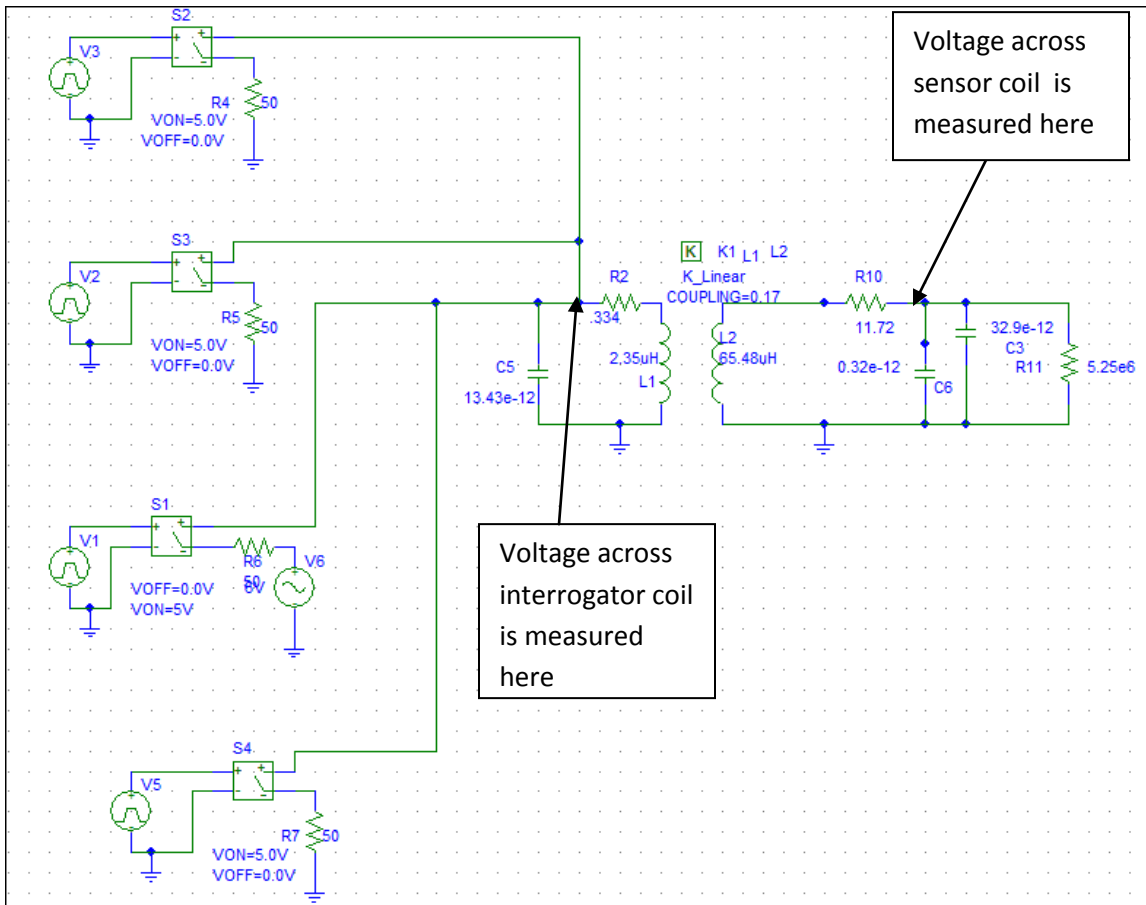
Figure 4.2. Circuit schematic for the time-domain gating technique. (Note that component labels are different in this circuit schematic)
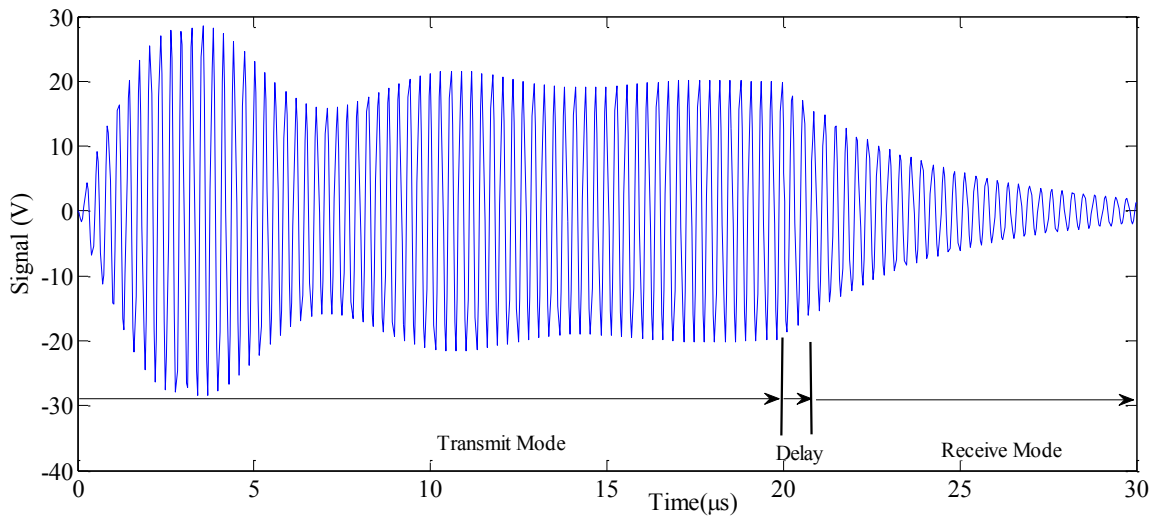
Figure 4.3. Voltage across the sensor coil in simulation for source frequency=3.4125 MHz. From this figure f_0 simulated =3.4124 MHz.
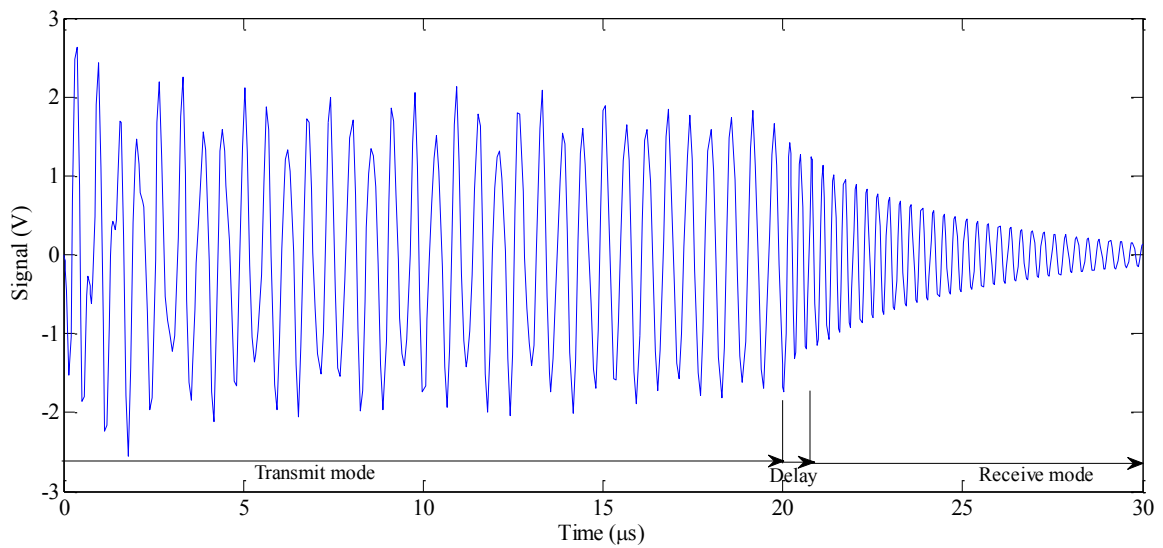
Figure 4.4. Voltage at the sensor coil in simulation for source frequency=1.7 MHz. From this figure f_0 simulated =3.4124 MHz.
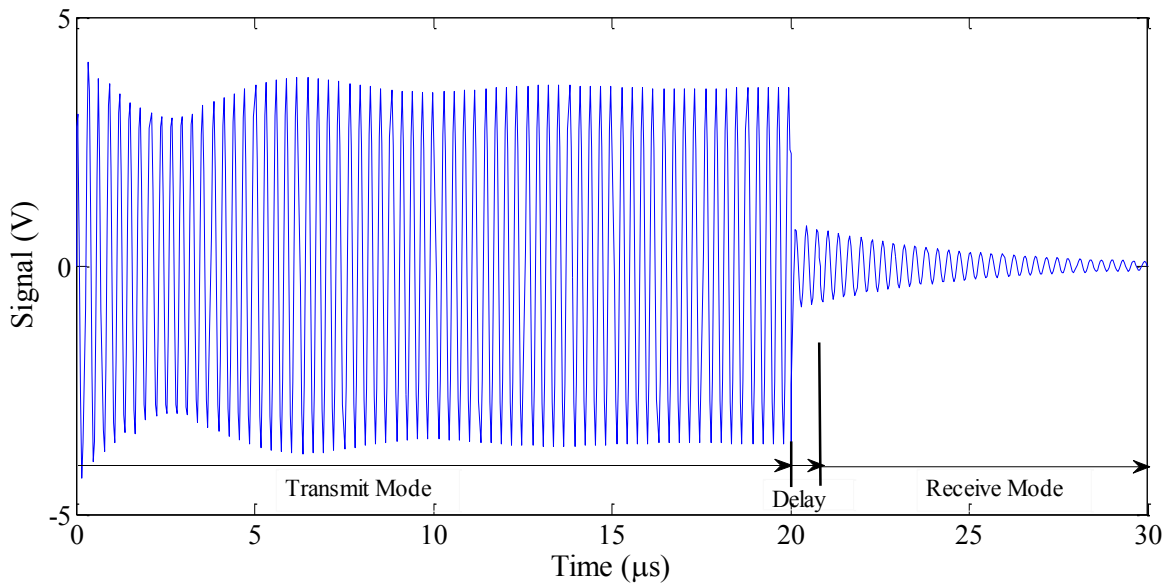
Figure 4.5. Voltage across the interrogator coil in simulation for source frequency=3.4125 MHz. From this figure f_0 simulated =3.4124 MHz.
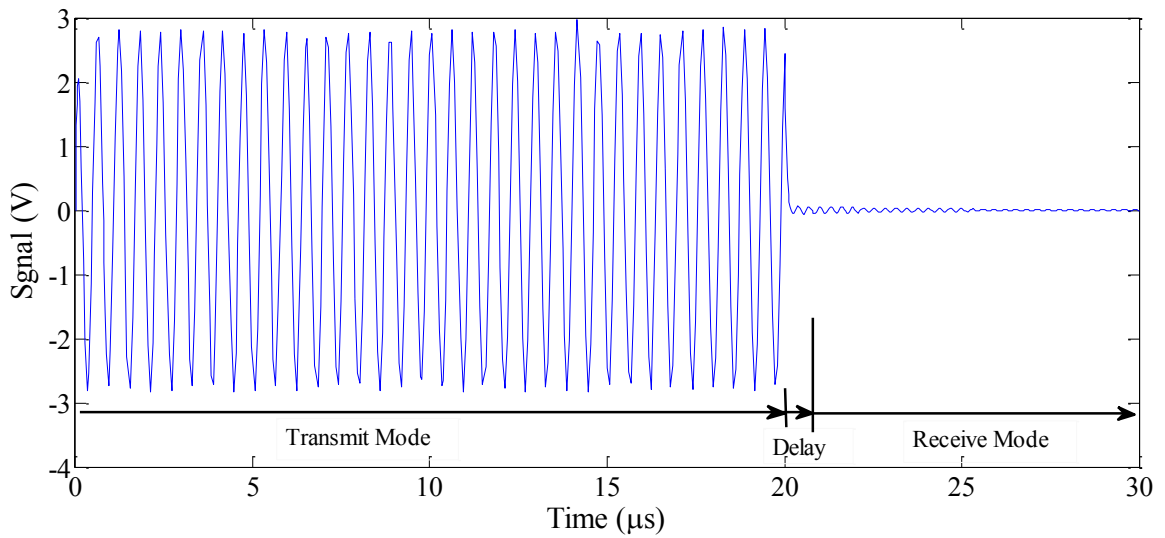
Figure 4.6. Voltage at the interrogator coil in simulation for source frequency=1.7 MHz.

From this figure f_0 simulated =3.4124 MHz.
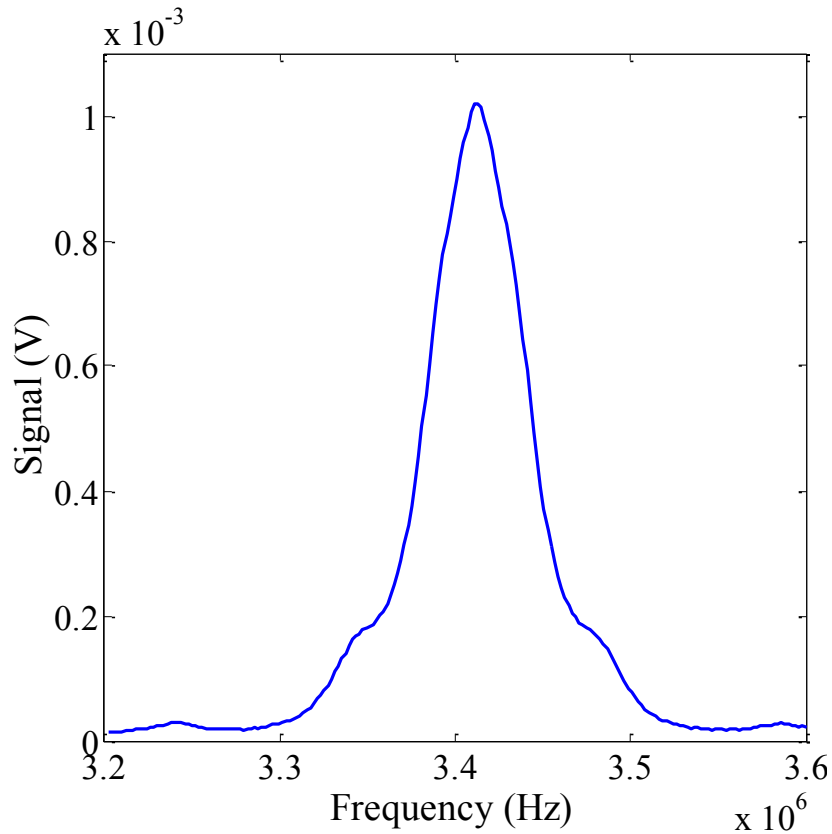
Figure 4.7. Simulated spectrum measured with the lock-in amplifier model. From this figure f_0 simulated =3.4122 MHz.

4.3 Signal at Different Distances for Time-Domain Gating Interrogation Technique

Using the interrogation system described in section 3.6, the received signal was measured for different separation distances. Fig. 4.8 shows the time-domain signal, $v_r(t)$, from the sensor in receive mode for a distance, $R=$ 10 cm and source frequency, $f=3.4122$ MHz. This exponentially decaying signal was observed with the oscilloscope. An exponentially decaying sinusoid ($Ae^{-t/\tau} sin(2\pi f_0+\phi)$) was fitted to this received signal where, $A=0.0229$ V, $\tau=1.1\times10^{-5}$ s, $f_0=3.4125\times10^6$ Hz, and $\phi=0.86$ rad. This yields a

Q=118. The response spectrum, S, as measured with the lock-in amplifier, for different separation distances is plotted in Fig. 4.9.
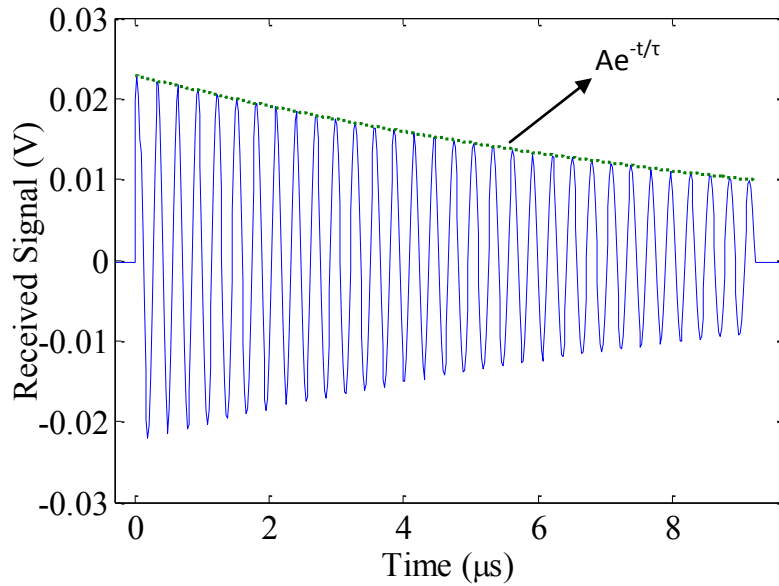
Figure 4.8. Signal from the sensor in receive mode (f_0=3.4125x10^6 Hz , Q=118).

From the peak of the response spectrum, the resonant frequency was determined. The bandwidth of the system was 41.67 Hz. 201 evenly distributed measurement points were taken between 3.2 MHz to 3.6 MHz. For each frequency point, the response was measured only once. For this bandwidth and measurement setup, an SNR at resonance of 34.93 dB is achieved for a distance of 25 cm. The noise was measured by keeping the source frequency constant at f_0 for 100 samples and then using the RMS of the signal. Noise voltages for all distances were very close. Table 4.1 lists the resonant frequency and SNR at resonance for different separation distances. The results demonstrate 352 parts per million accuracy at 25 cm.

Table 4.1. Resonant frequency and SNR for different distances for time-domain gating.

Distance (cm)	Resonant Frequency (MHz)	SNR (dB)
10	3.4125	76.58
15	3.4125	57.09
17	3.4125	53.50
20	3.4124	46.73
22	3.4123	41.80
25	3.4113	34.93
30	3.4102	27.63
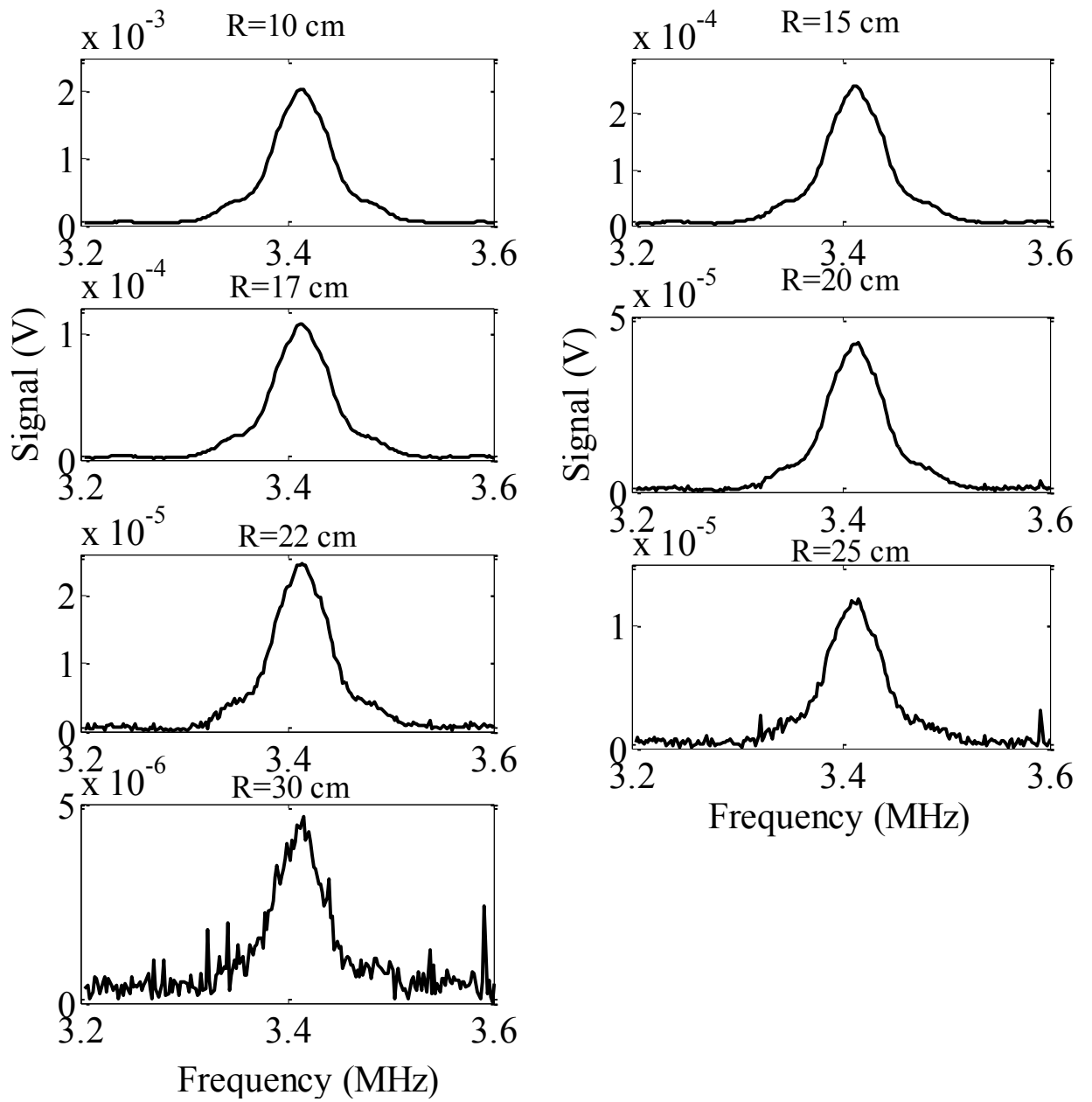
Figure 4.9. Received signal spectrum, S, for different separation distances.

The mutual coupling, M between the sensor coil and the interrogator coil was calculated for different distances using eqn. 3.26. The MATLAB® program in Appendix A.2 implements the calculation. The normalized received signal for a fixed exciting frequency f=3.4129MHz is plotted in Fig. 4.10 with the normalized M^2 value for different distances. It can be seen that the normalized received signal is in good agreement with the normalized M^2, showing that the path loss follows the theory established in section 3.5.
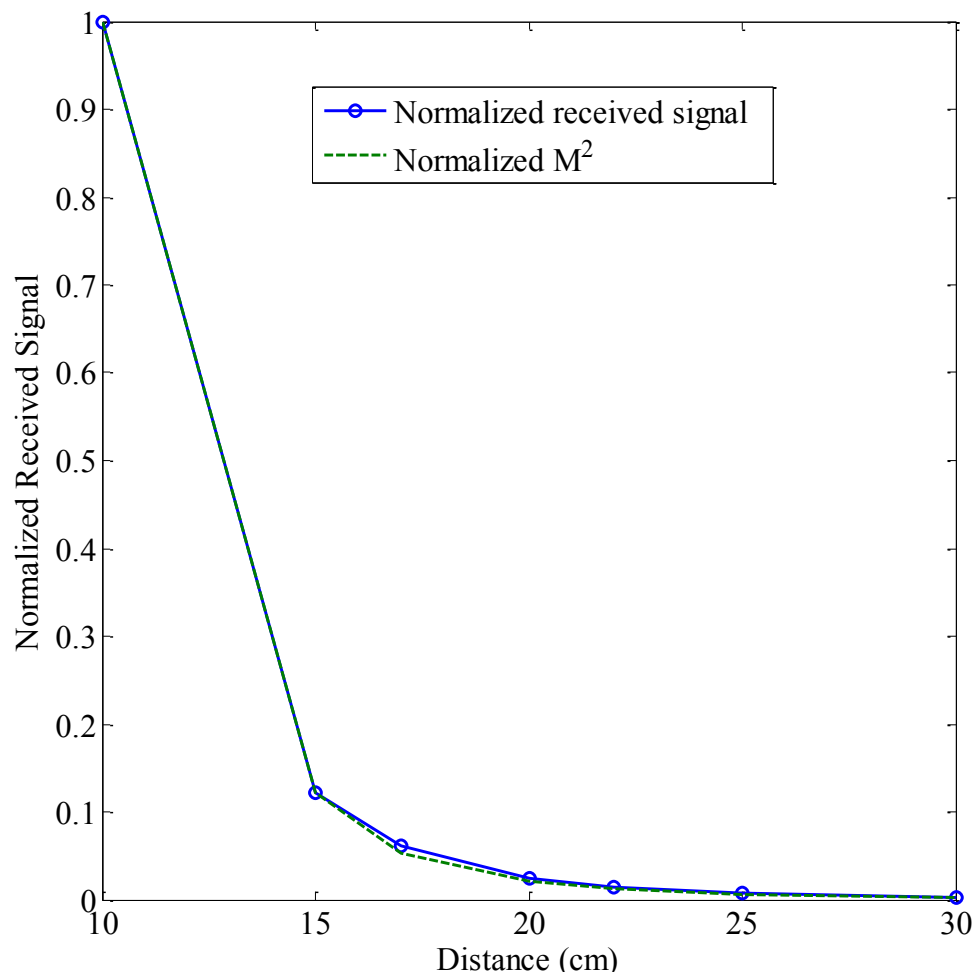
Figure 4.10. Normalized received signal and M^2 for sensor.

4.4 Signal at Different distances for Impedance Measurement Technique

In order to compare the time-domain interrogation technique with the impedance measurement method the interrogator coil input impedance spectrum was also measured with an impedance analyzer. The bandwidth of the system was set to 39.8Hz (BW=41.67 Hz in the TD measurements) and frequency was swept from 3.2 MHz to 3.6 MHz with 201 measurement points and no averaging, so that it was comparable with the time-domain gating measurements. Fig. 4.11 shows the spectrum measured with the impedance analyzer at different interrogation distances. With this method the maximum interrogation distance where a measurable peak was obtainable was 20 cm, which provided a 19.70 dB SNR at resonance. This interrogation distance is much less than that of the time-domain gating. Table 4.2 lists the resonant frequency and SNR at resonance for different separation distances. The SNR of the impedance measurement method at R=15 cm was comparable to that of the time-domain gating method at R=25 cm.
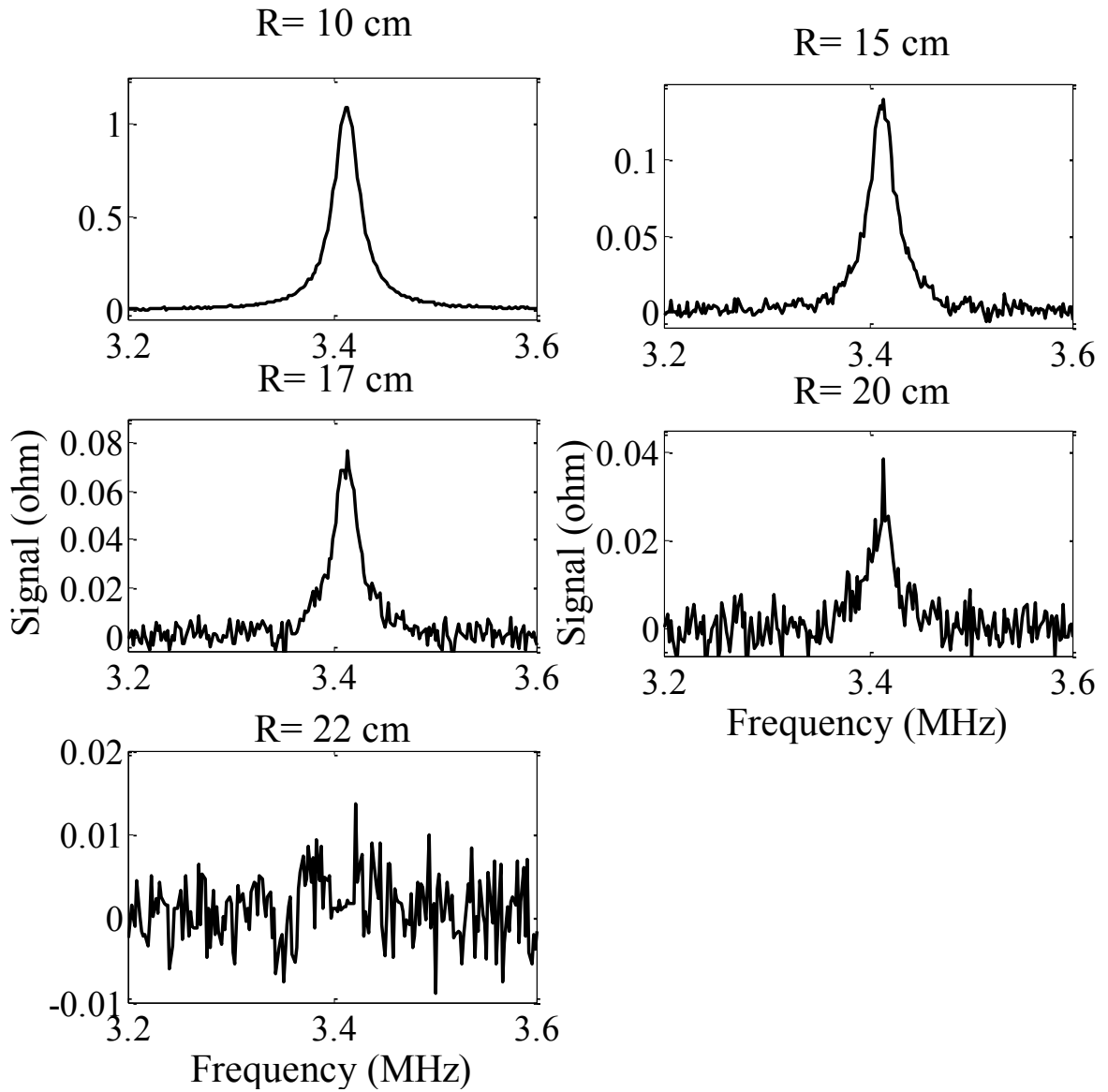
Figure 4.11. Real part of the impedance spectrum for different separation distances.

Table 4.2. Resonant frequency and SNR for different distances for impedance measurement.

Distance (cm)	Resonant Frequency (MHz)	SNR (dB)
10	3.4125	53.19
15	3.4125	34.13
17	3.4120	28.08
20	3.414	19.70

4.5 Effect of Surrounding Environment

To see the effect of interference from surrounding environment on the sensor, a section of rebar was placed in close proximity to the interrogator coil and then to the sensor as shown in Fig. 4.12. Response spectrum measured using both interrogation techniques is shown in Fig. 4.13. The spectrum shows that the time-domain gating eliminates any effect of surrounding object on measurements whereas measurements are sensitive to surrounding objects in the impedance measurement method.
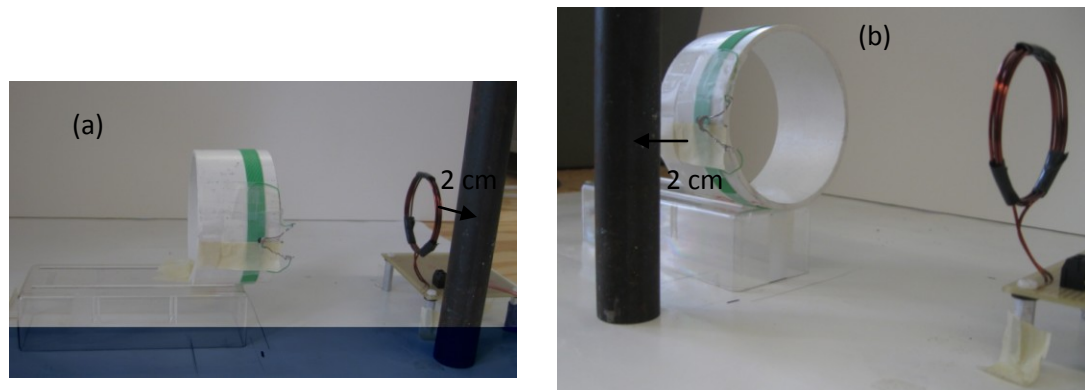
Figure 4.12. Section of rebar (a) placed close to the interrogator coil. (b) placed close to the sensor.

For the impedance measurement method, when the rebar was placed next to the interrogator coil, the interrogator coil impedance, $(R_1+j\omega L_1)$ in eqn. 2.9, increased which increased the background Z_{in}. The resonant frequency remained approximately same as the total sensor impedance Z_T was not affected. When the rebar was placed next to the sensor, Z_T in eqn. 2.9 was changed which resulted in shifting the resonant frequency. In time-domain gating the transient response from the sensor shown in eqn. 3.6 is measured

in the received mode. As eqn. 3.6 is not affected by the interrogator coil impedance, the measurements were not affected when the rebar was placed next to the interrogator coil. Results also show that the measurements were not significantly changed when the rebar was placed next to the sensor coil in time-domain gating method. These measurements will need future investigation because according to the theory when the rebar was placed very next to the sensor, the resonant peak should have shifted due to the change of sensor inductance.
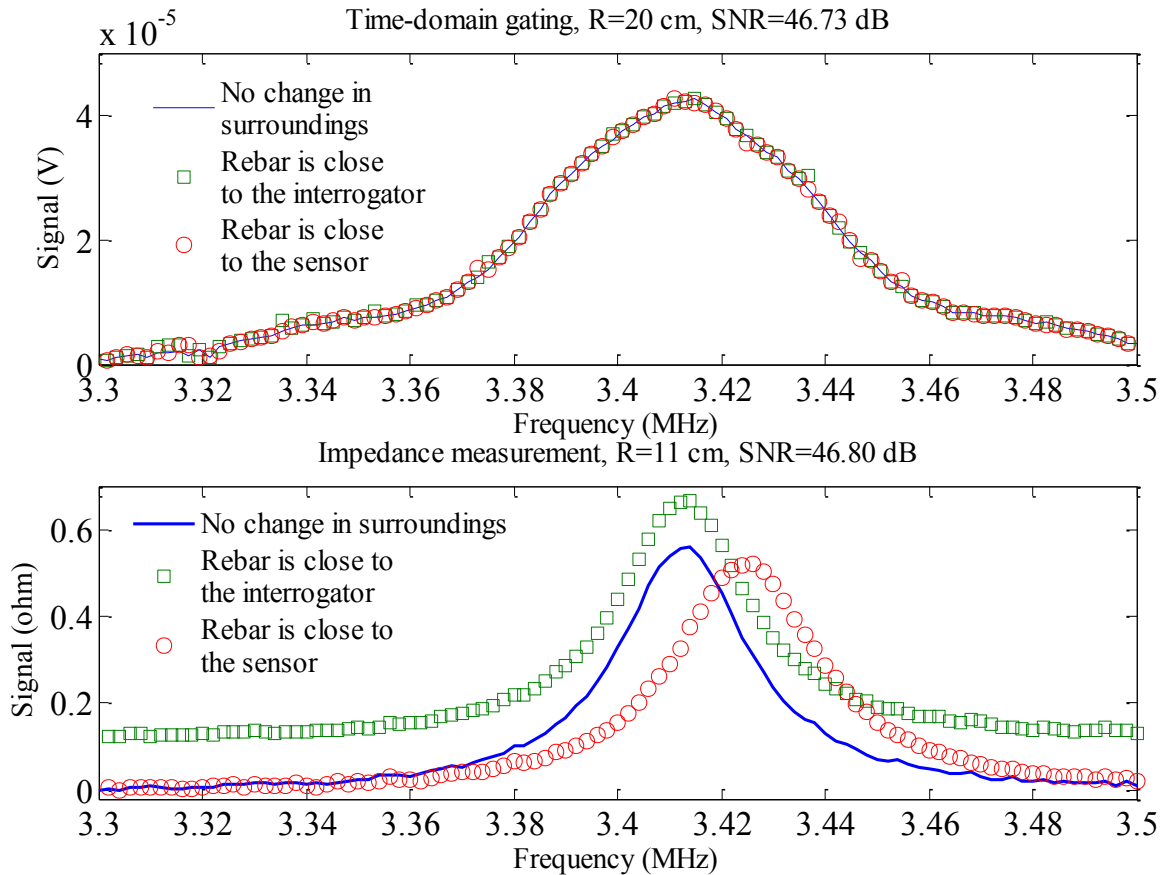
Figure 4.13. Spectrum for change in surrounding objects.

4.6 Measuring ΔC_P and ΔG_P of a Sensor

Coupled coil sensor works by changing either the f_0 or the Q as a function of the measurand. The f_0 and Q of the sensor described in section 4.1 was changed by varying the C_P and G_P of the sensor to test whether the time-domain gating can detect the change in f_0 and Q. The switching circuit shown in Fig. 4.14 was used to vary the parallel capacitance of the sensor coil. The schematic shows the values measured with an impedance analyzer. The shunt conductance of C_{P2} and C_{P3} were very small and neglected. Fig. 4.15 shows the response spectrum for different C_P values. ΔC_P values were obtained from the resonant frequencies using $\Delta C_P=(4\pi^2 f_0^2 L_S)-C_{P1}$. Table 4.3 lists the measured f_0 and measured ΔC_P from f_0 along with the actual ΔC_P values. This type of sensor with discrete loads could be used as a fused sensor in corrosion for example.
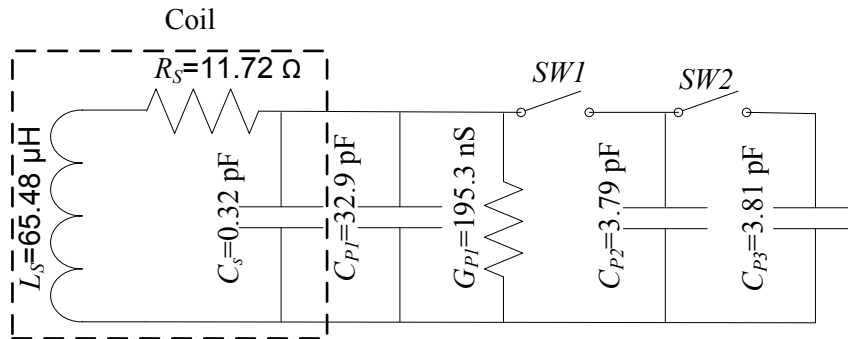
Figure 4.14. Switching circuit for measuring ΔC_P.
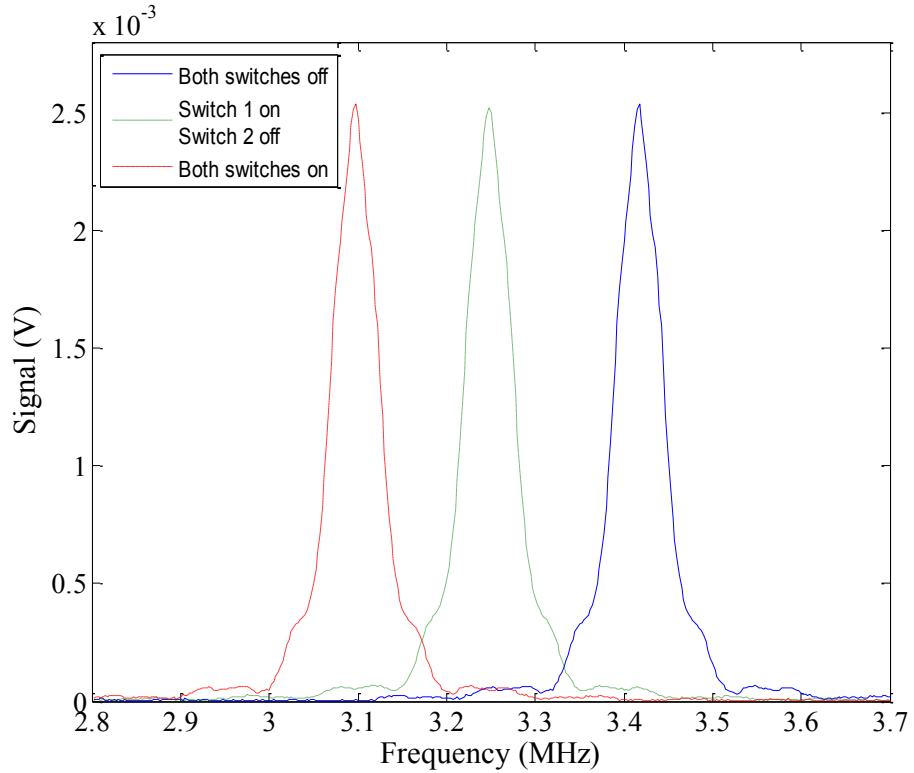
Figure 4.15. Response spectrum for different C_P values.

Table 4.3. Measured f_0, measured ΔC_P from f_0 and actual ΔC_P for the sensor.

Measured f_0 (MHz)	ΔC_P (pF) from f_0	ΔC_P (pF) measured using impedance analyzer	ΔC_{Perr} (pF)
3.4125	-0.01	0	0.01
3.2435	3.55	3.79	0.24
3.0929	7.22	7.6	0.38

Using the circuit shown in Fig. 4.16, the shunt conductance of the sensor was varied by connecting different valued resistors, R_p in parallel to the fixed capacitor. Using the time-domain gating, Q was measured from the received signal as described in section 4.3 and G_P were obtained from the Q values using eqn. 2.5. Fig. 4.17 shows the time

domain signal for different ΔG_P values. Table 4.4 lists the measured Q, the measured ΔG_P from Q and the actual ΔG_P of the sensor. Results indicate that time-domain gating interrogation technique can detect the change of C_P or G_P by measuring the f_0 or Q, respectively. The possible reasons for small errors in ΔC_P or ΔG_P measurements are the accuracy of the interrogation technique to measure f_0 or Q, the accuracy of the impedance analyzer for measuring the value of the sensor elements and the accuracy of the curve-fitting technique used for obtaining f_0 from the frequency response spectrum or for obtaining Q from the time-domain received signal from the sensor.
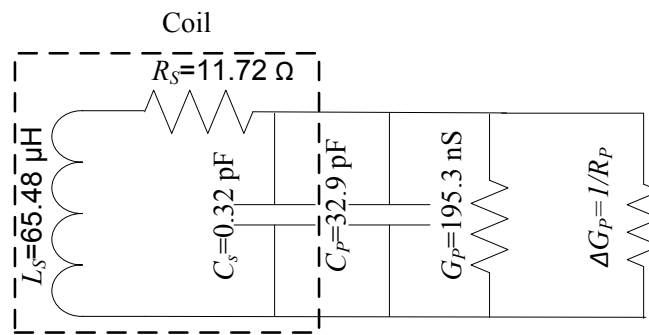
Figure 4.16. Switching circuit for measuring ΔG_P.
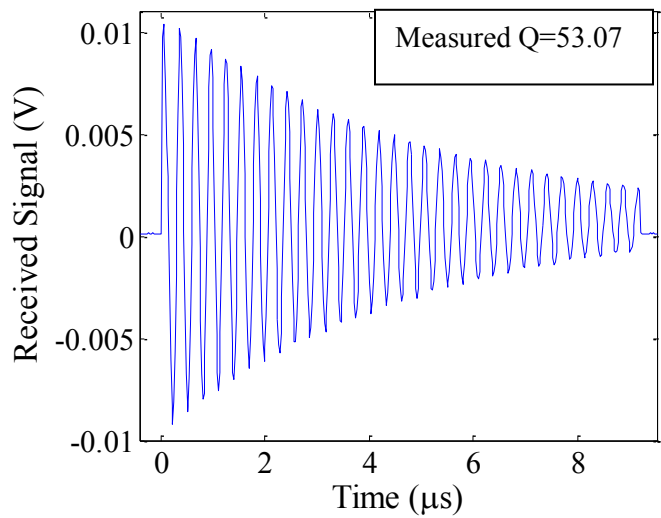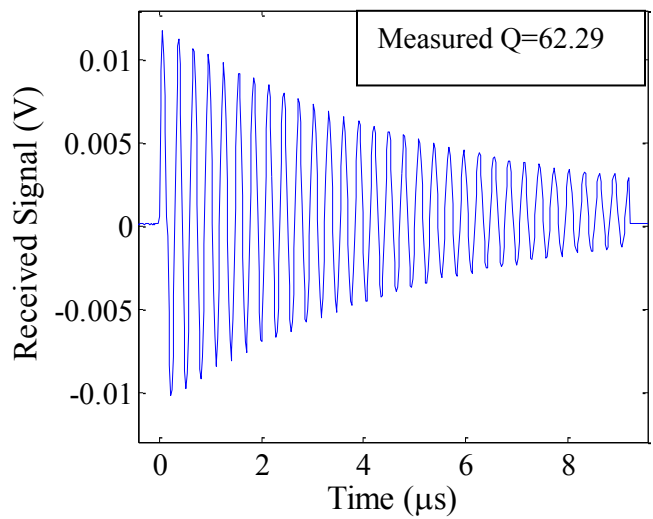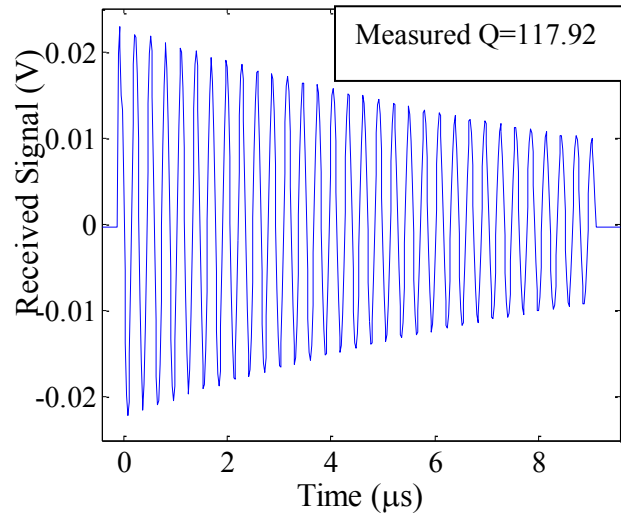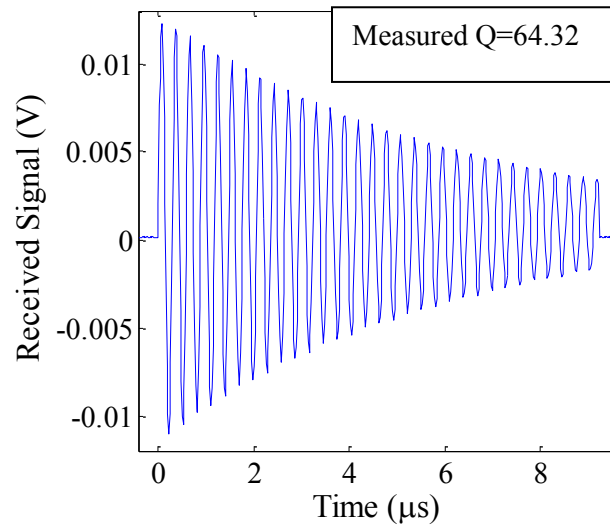
Figure 4.17. Time domain received signal for different ΔG_P values.

Table 4.4. Measured Q, measured ΔG_P and actual ΔG_P for the sensor.

Measured Q	ΔG_P (S) from Q	ΔG_P (S) measured using impedance analyzer	ΔG_{Perr} (S)
117.92	-1.01×10^{-7}	0	1.01×10^{-7}
62.29	5.29×10^{-6}	6.85×10^{-6}	1.56×10^{-6}
53.07	7.28×10^{-6}	8.46×10^{-6}	1.18×10^{-6}
64.32	4.88×10^{-6}	5.57×10^{-6}	6.4×10^{-7}

Chapter 5: Coupled Coil Relative Humidity Sensor

5.1 Introduction

Concrete foundations, masonry and stone facades are exposed to a considerable amount of water when exposed to snow and rain. The monitoring and estimation of moisture content inside the structure can be critical for their long service life. For concrete structures in contact with soil, water or moisture beneath the surface layers (base, subbase and subgrade) causes frost heave issues, subsurface erosion and loss of structural integrity. In addition, excessive humidity and damp environment inside many civil engineering materials are one of the main causes for mold growth. There is a serious environmental health issue of mold growth in civil structures due to its harmful nature to human health. This moisture content inside the structure can be an important indicator for determining the potential to mold growth. For all these reasons, it is important to detect the moisture content inside a civil structure to ensure reliability, effectiveness of the structure and a healthy environment [Ong et al., 2008], [Bornehag et al., 2001], [Peat et al., 1998]. Some of the current commercially available methods for monitoring moisture content inside civil structures are discussed below.

5.1.1 Concrete moisture meter

These meters have been used for decades to measure the moisture content inside concrete structures. They are typically a hand-held device that utilizes non-destructive impedance measurement for moisture determination. There are two kinds of moisture

meter. The pin-type measures electrical resistance across opposed sets of pins, which are pushed into the surface. A voltage is applied to the pins via a battery and leakage current is monitored. One advantage of pin-type meters is that those employing insulated pins can measure moisture content at varying depths in the structure. Fig. 5.1 shows a pin-type meter. Pinless meters use the capacitance method, which utilizes the relationship between the moisture content and the dielectric properties of the concrete. There is no pin intrusion into the surface. In one approach, parallel co-planar electrodes are mounted on the unit's base. The electrodes transmit radio frequency signals which penetrate into the concrete to a depth of approximately 1 inch. The meter can be moved across the surface to produce a capacitive image and identify pockets of moisture. However, a concrete moisture meter is affected by material and chemical inhomogeneities in the concrete. This can be due to the density of the concrete and aggregate size to the chemical properties of the slab [Concrete moisture meter, 2010]. These meters typically measure the moisture content to a depth of approximately only 1 inch from the surface and require an inspector to tour the structure pushing the pintype meter into the concrete or holding the pinless meters on the surface. Therefore, there is a need for wireless moisture monitoring sensor that can be embedded and measure the moisture content in any depth of the structure.

Figure 5.1. Concrete moisture meter.

5.1.2   SensCore humidity sensor

This type of embedded moisture sensor is composed by 4 stainless steel bars which are anchored to a stainless support. Fig. 5.2 shows a SensCore humidity sensor. The 4 bars are placed in the concrete at 4 different depths. The resistivity between pairs of bars is measured to determine the concrete resistivity across the depth. A low resistivity indicates higher humidity and vice versa. The concrete temperature also influences the resistivity and is therefore measured at two depths. The sensor is designed for installation in new structures or for repair work, when the concrete cover is placed. The sensor is connected to a datalogger which transmits the measured data to a central unit. The connection between the datalogger and the central unit can be wireless or wired. For a wired connection, the central unit provides power to the datalogger whereas for wireless connection the datalogger needs power source of its own. The data can be saved

in central unit's internal memory for manual retrieval or can be transmitted from the central unit by an ethernet connection to a local PC [Roctest humidity sensor], [Roctest datalogger], [Roctest central unit]. One of the major problems for the wireless SensCore humidity sensor is recharging or replacing the batteries of the datalogger.

Figure 5.2. SensCore humidity sensor [Roctest humidity sensor].

5.1.3 Wireless passive sensors

Embeddable wireless passive sensors are being developed for monitoring water content or relative humidity inside civil structures. This type of sensor consisted of a fixed inductor connected in parallel with a capacitor. The capacitance of the capacitor is dependent on its dimension and the dielectric constant of the medium. The dielectric constant of water, about 70–80, is much higher than that of most civil construction materials, which are generally less than 5. Therefore, the presence of water significantly increases the capacitance of the capacitor, resulting to lowering the sensor's resonant frequency. Thus by tracking the sensor's resonant frequency wirelessly, water content or relative humidity inside civil structures can be monitored [Harpster et al., 2002], [Ong et al., 2008]. They are not commercially available.

In this chapter an embeddable coupled coil relative humidity sensor is described. As it is passive, it does not have the problem of recharging or replacing batteries. The design of the sensor is simple and it is inexpensive to make and install. Therefore, this sensor can find application for wirelessly monitoring moisture content inside many types of structures or processes.

5.2 Description of the Sensor

A prototype coupled coil sensor was constructed based on the approach described in chapter 4. The sensor coil was made of wire of 1.2 mm diameter and contains 20 turns of 5.1 cm diameter, producing L_s=25.30 μH and R_S= 1.86 Ω. A commercial capacitive humidity sensor HCH-1000 [Honeywell, 2007] with moisture sensitive capacitance, C_P and conductance, G_P was connected in parallel with the coil. C_P varied in the range of 313.05 pF – 343.49 pF resulting in a change of f_0 between 1.788MHz-1.707 MHz and G_P varied in the rage of 198 μS-282.2 μS resulting in a change of Q between 17.77-13 for relative humidity between 20%-70%, respectively. Fig. 5.3 shows the relative humidity sensor. It should be noted that the capacitance also varies with temperature. According to the datasheet the temperature coefficient is 0.15-0.17 pF/°C.

Figure 5.3. Relative humidity sensor.

5.3 Relative Humidity Test Chamber

In order to test, the relative humidity sensor described in section 5.2 was placed in a chamber constructed from plexiglass as shown in Fig. 5.4. A small piece of foam soaked in water was kept in the chamber on a Petri dish. Dry air was passed through the chamber using a flow meter (Matheson Model No. 7640T W/602) to vary the relative humidity inside the chamber. A thermo-anemometer (Alnor Compuflow Model 8585) was used to continuously monitor the relative humidity and the temperature inside the chamber. The Q of this sensor was low because the HCH-1000 has high loss due to the conductance, G_P. Due to the low Q, the sensor signal was weaker and a small separation distance (4.5 cm) was chosen for the experiment.
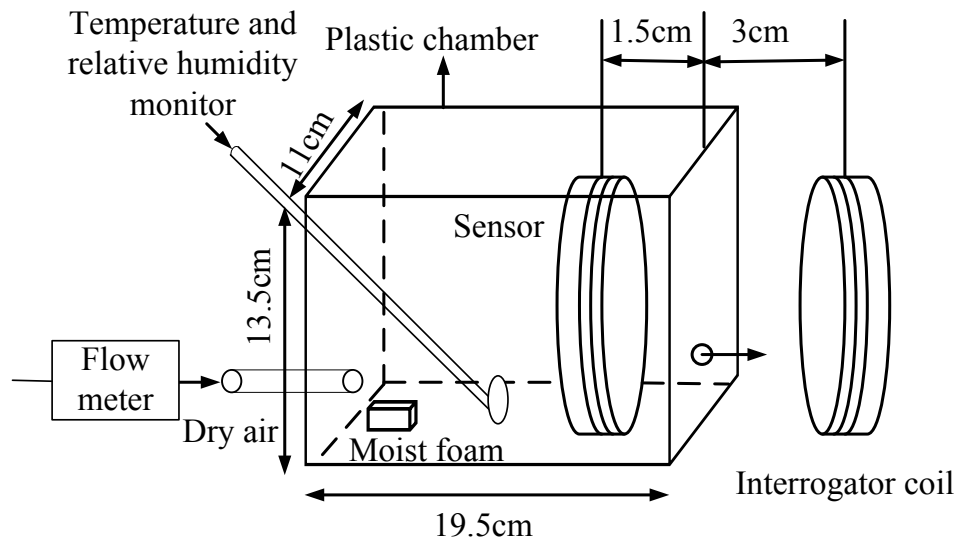
Figure 5.4. Setup of the plastic chamber, sensor and interrogator coil for relative humidity sensing.

5.4 Measurements

In our tests, the air temperature inside the chamber was kept constant at 23.5+0.6°C. The setup of the chamber, sensor and interrogator coil is shown in Fig. 5.4. The relative humidity (%RH) inside the chamber was varied from 20% to 70% as measured using the anemometer. The resonant frequency was determined at 5% intervals using the time-domain gating interrogation system described in chapter 3. The capacitance of HCH-1000 was obtained from the resonant frequency using eqn. 2.4. In a separate test, the capacitance of HCH-1000 was measured directly with the impedance analyzer in order to compare with the values obtained from the time-domain gating method. Fig. 5.5 shows the capacitances measured using both approaches. Results indicate that capacitances measured from resonant frequency are greater than the

capacitances obtained from direct measurement and have a maximum deviation of 1.26 pF. The possible reason for this deviation is the high loss of the sensor. According to the datasheet the capacitance of HCH-1000 changes linearly with relative humidity and the sensitivity varies from 0.55 pF/%RH to 0.65 pF/%RH [Honeywell, 2007]. A linear-curve was fitted to the capacitance data measured from the resonant frequency of the sensor. The results indicate a deviation of <2% RH from the linear fit. It can be seen that a linear curve fits well with the measured capacitance values. The slope of the curve was 0.596 pF/%RH which was within the datasheet specifications. From the linear curve fitting, eqn. 5.1 and eqn. 5.2 were obtained, which relate the relative humidity (*%RH*) to the capacitance, C_P and resonant frequency, f_0, of the sensor, respectively. Here unit of C_P is pF and f_0 is MHz.

$$\%RH = 1.68C_P - 509. \tag{5.1}$$

$$\%RH = \frac{1684}{f_0^2} - 509. \tag{5.2}$$
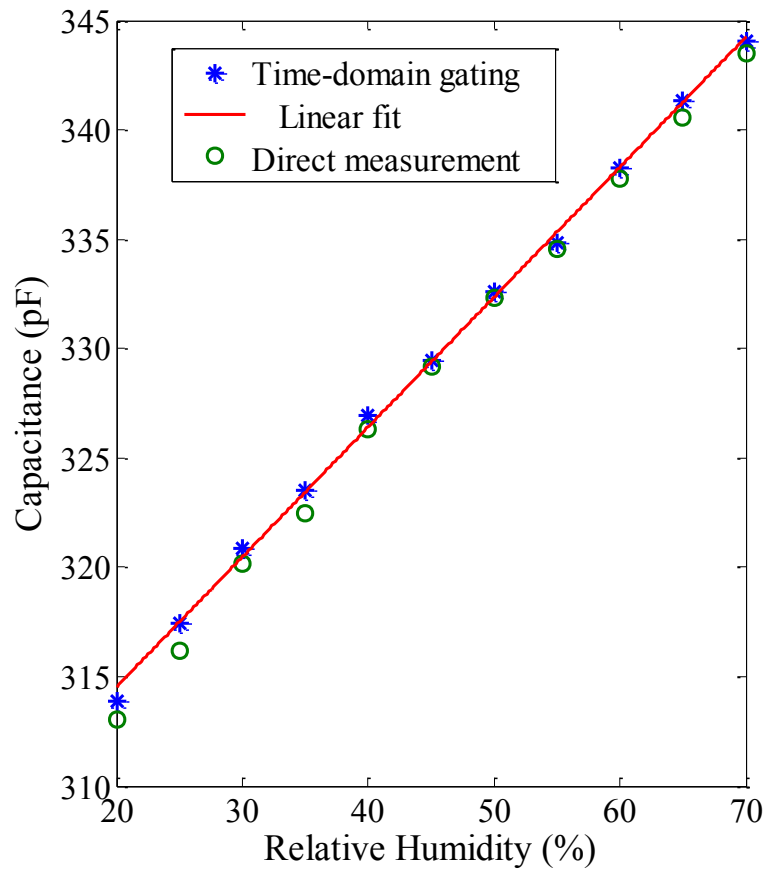
Figure 5.5. Capacitance of HCH-1000 measured directly with an impedance analyzer and from the resonant frequency measured by the RH sensor.

Results indicate that the time-domain interrogation technique is able to measure the capacitance change of HCH-1000 and less than 2% change in relative humidity can be detected with this relative humidity sensor. The sensor will have potential for monitoring relative humidity in a remote environment.

Chapter 6: Coupled Coil Corrosion Sensor

6.1 Introduction

Corrosion of reinforcing steel, which results in premature deterioration of concrete structures, is a worldwide problem. This type of damage can reduce the service life of the infrastructure and can create safety hazard. Ingress of Cl^- ions to the steel surface is considered as one of the most important causes of corrosion initiation of reinforcement steel. When a structure is first built, bare reinforcing steel is exposed to oxygen and water, and a very thin (approximately 1 μm) dense layer of either metal oxide or hydroxide is formed on the surface [Ervin & Reis, 2008]. Reinforcing bars are protected from corrosion by this thin layer, referred to as the passive layer. The highly alkaline environment of the surrounding concrete (pH value around 12.6) helps to maintain this passive layer on the rebar surface. However, Cl^- ions from de-icing salts used extensively to keep roads clear of snow and ice in winters, exposure to marine environment or admixtures present at the time of concrete mixing permeate the concrete and depassivate the reinforcing steel. When the Cl^- ions reach the reinforcement steel depth and destroy the passive layer, both oxygen and water must be present for reinforcing steel to corrode. Once the passive layer is destroyed, the corrosion propagation period starts. Once corrosion begins, it is self-sustaining. Rust formation at the outer surface of the reinforcement steel results in increase of the steel cross-section. Moreover, rust products occupy two to six times the volume of the original rebar. These rust products exert stress within the concrete which cannot be supported by the limited

plastic deformation of the concrete. As a result cracks are generated. The cracks degrade the ability of the surrounding concrete to confine the corrosion product and subsequently reduce the interfacial bond. Multiple cracks can eventually lead to concrete section loss (spalling). Spalls which in turn provide new means for water and Cl^- ions to reach the reinforcement steel and results in progressive deterioration of the concrete [Cabrera, 1996], [Virginia Technologies, Inc.], [Ervin & Reis, 2008].

The estimated cost to repair reinforced concrete structures is $200 per square meter of exposed surface. As a result, repair, maintenance, replacement cost of reinforced concrete nowadays consumes a major part of the current spending on civil infrastructure. If indirect costs (delays, inconvenience and lost productivity) are taken into account, the cost can run over 10 times as much per year. Corrosion is more than an economic issue. It can lead infrastructures to collapse, injuring and killing people. Therefore, inspection and monitoring techniques are needed for early detection of corrosion due to the large cost associated with it. Properly monitoring the corrosion performance of reinforcement steel and taking suitable measures at the appropriate time can save life and money [Song & Saraswathy, 2007], [Ervin & Reis, 2008], [Virginia Technologies, Inc.], [Cabrera, 1996], [Apostolopoulos & Papadakis, 2008].

6.2 Existing Techniques for Corrosion Monitoring

Besides visual and invasive inspection many electrochemical and non-destructive techniques are available for monitoring corrosion of reinforcement steel in concrete structures.

6.2.1 Open circuit potential (OCP) measurement

Monitoring open circuit potential is the most typical procedure to the routine inspection of reinforced concrete structures. The tendency of any metal to react with an environment is indicated by the potential it develops in contact with the environment. In reinforced concrete structures, concrete acts as an electrolyte and the reinforcement steel develops a potential depending on the concrete environment, which may vary from place to place. As in Fig. 6.1, the principle involved in this technique is essentially measurement of corrosion potential of rebar with respect to a standard reference electrode, such as saturated calomel electrode (SCE), copper/copper sulphate electrode (CSE), silver/ silver chloride electrode etc [Song & Saraswathy, 2007]. ASTM C876 *Standard Test Method for Half-Cell Potential of Reinforcing Steel in Concrete* describes interpretation of measurements of this technique. Potential readings are affected by a number of factors, which include polarization by limited diffusion of oxygen [Song & Saraswathy, 2007], [Anup, 1983], concrete porosity and the presence of highly resistive layers. OCP values can only provide information for corrosion probability and cannot indicate the rate of corrosion [Song & Saraswathy, 2007].

65
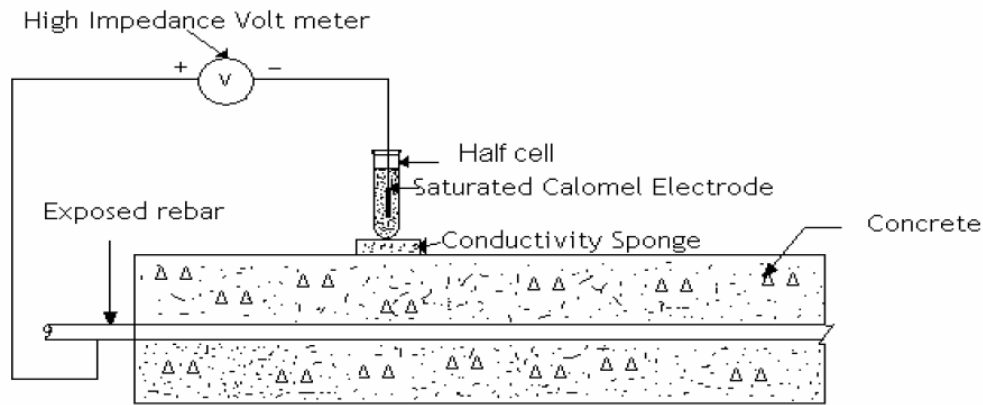
Figure 6.1. Schematic representation of open circuit potential measurement [Song & Saraswathy, 2007].

6.2.2 Surface potential measurement

During the corrosion process, electric current flows between the cathodic and anodic sites through the concrete. This flow can be detected by measurement of potential drop in the concrete. Surface potential measurement is a technique for identifying anodic and cathodic regions in concrete structures and indirectly detecting the probability of corrosion of rebar in concrete as in Fig. 6.2. Two reference electrodes are used for surface potential measurements. No electrical connection to the rebar is necessary in this technique. In this measurement, one electrode is kept fixed on the structure on a symmetrical point. The other electrode, called moving electrode, is moved along the structure. The potential of movable electrode is measured against the fixed electrode using a high impedance voltmeter. A more positive potential reading represents anodic area where corrosion is possible. In this manner a surface potential map is developed where a greater the potential difference between anodic and catholic areas, greater is the probability of corrosion [Song & Saraswathy, 2007].

66
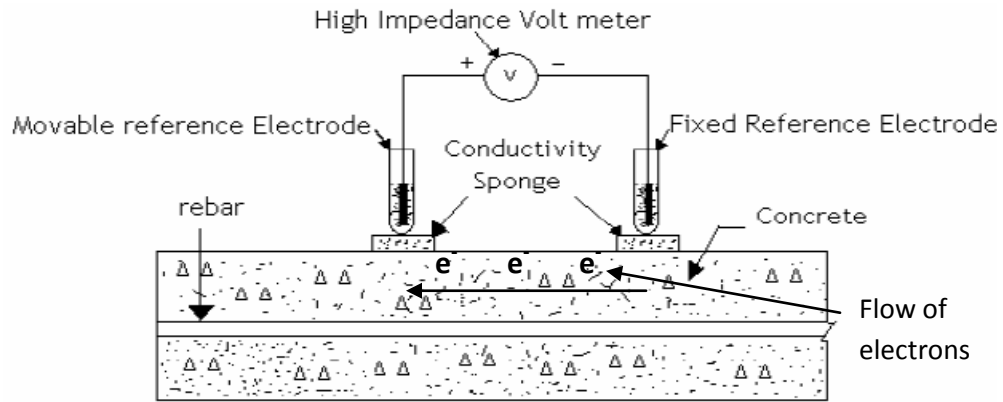
Figure 6.2. Schematic representation of surface potential measurement [Song & Saraswathy, 2007].

6.2.3 Linear polarization resistance measurement

The data obtained by this technique provides valuable insight into the corrosion rate of the reinforcement steel. As shown in Fig. 6.3 the technique requires only one connection to the reinforcement steel. In LPR measurements the reinforcement steel is perturbed by a small amount from its equilibrium potential. This is done potentiostatically by changing the potential of the reinforcement steel by a fixed amount, ΔE, and monitoring the current decay, ΔI, after a fixed time. Alternatively it is done galvanostatically by applying a small fixed current, ΔI, to the reinforcing steel and monitoring the potential change, ΔE, after a fixed time period. In each case the conditions are selected such that the change in potential, ΔE, falls within the linear Stern–Geary range of 10–30 mV [Song & Saraswathy, 2007]. The polarization resistance, R_p, of the steel is then calculated from

$$R_p = \frac{\Delta E}{\Delta I}.$$
(6.1)

From R_p the corrosion rate, I_{corr}, can be calculate as

$$I_{corr} = \frac{B}{R_p},$$ (6.2)

where B is the Stern-Geary constant. The value of B is 25 mV for active steel and 50 mV for passive steel [Gowers et al., 1994]. In order to determine the corrosion current density, J_{corr},

$$i_{corr} = \frac{I_{corr}}{A}.$$ (6.3)

The surface area A of the steel that is polarized needs to be known accurately. In a conventional LPR test the perturbation is applied from an auxiliary electrode on the concrete surface. The surface area of steel assumed to be polarized is that lying directly beneath the auxiliary electrode [Song & Saraswathy, 2007]. This technique suffers from the difficulty in quantifying the area of reinforcement steel surface, A, being measured.
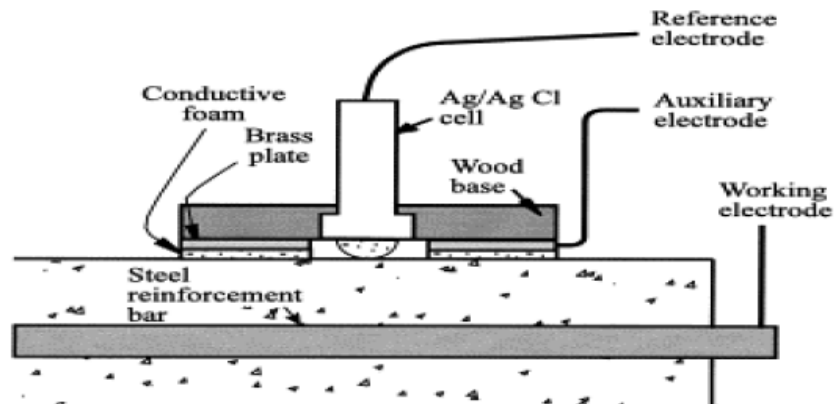
Figure 6.3. Schematic representation of linear polarization resistance measurement [Song & Saraswathy, 2007].

6.2.4 Galvanostatic pulse transient method

This is a transient polarization technique working in the time-domain. A short time anodic current pulse is imposed galvanostatically on the reinforcement steel from a counter electrode. The counter electrode is placed on the concrete surface. The applied current is in the range of 10 to 200 µA and the typical pulse duration is up to 10 s. The reinforcement steel is polarized in the anodic direction compared to its free corrosion potential. This results in change of the electrochemical potential of the reinforcement steel which is recorded by a reference electrode as a function of polarization time. This method has the same problem as the linear polarization resistance measurement technique in determining the area of reinforcement steel surface being measured [Song & Saraswathy, 2007].
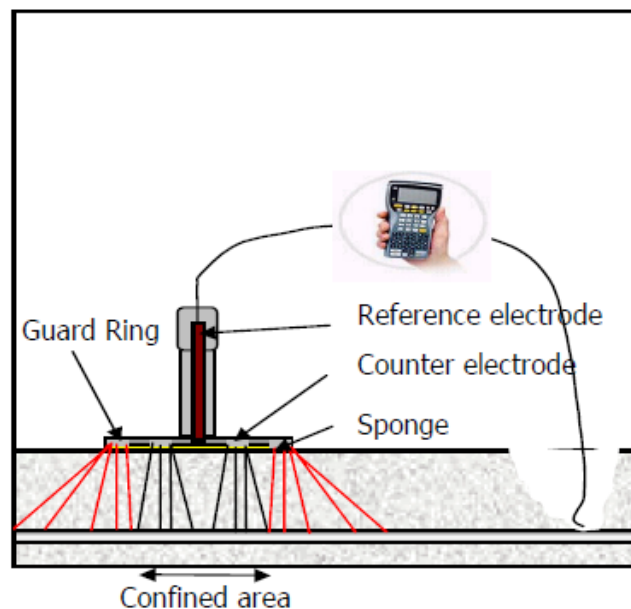
Figure 6.4. Schematic representation of galvanic pulse transient method [Song & Saraswathy, 2007].

6.2.5 Electrochemical impedance spectroscopy

In this technique an alternating voltage of to 20 mV is applied to the reinforcement steel and the resultant current and phase angle are measured at different frequencies. From studying the variation of the impedance with frequency, an equivalent electrical circuit is synthesized which gives same response as the corrosion system under study. The AC impedance technique gives more information than linear polarization resistance measurements, but it is very time-consuming to perform [MacDonald, 1991]. It can estimate a steady-state corrosion rate [Dhouibi et al., 2002]. This technique may be very attractive because it is applicable in a wide range of frequencies and can give detailed information about the mechanism and kinetics of the electrochemical reactions. Another advantage of this technique is the very small excitation amplitude, generally in the range of 5 to 10mV peak to peak. This minimally disturbs the steel, attached corrosion products or absorbed species during testing [Husain et al., 2004].

All of the above methods for corrosion monitoring require inspectors to tour a structure for installing analog probes into the concrete or placing the measurement device on concrete surface by hand. The demand of having an inspector on site increases the cost associated with the method. Moreover, they can be a safety risk to the inspector for some structures. Many of these methods are time-consuming as they require the structures to be temporarily shut down which creates an indirect cost associated with the method.

6.2.6   Optical fibre sensor

One type of optical sensor is based on the fact that the volume and diameter of embedded reinforcement steel will enlarge due to corrosion. One kind of optical fibre sensor is a Bragg grating sensor which is shown in Fig. 6.5. A fibre Bragg grating is obtained by producing a periodic variation in the index of refraction along a short section (about 10 -20mm) in the core of an optical fibre. The center wavelength of the reflected spectral band depends on the pitch length of Bragg grating or the grating period and the effective core refractive index. A fibre optic Bragg grating is wrapped on the reinforcement steel during installation. During corrosion, the increase in the reinforcement steel diameter results to the increase in fibre strain and change in pitch of the grating, which is measured by center wavelength [Zheng et al., 2009]. It can only detect corrosion in the area where it is connected to the reinforcement steel. Another kind of fibre optical fibre sensor employs distributed Brillouin scattering sensors [Zou et al., 2004]. This sensor is based on Brillouin loss technique where two counter propagating laser beams, a pulse and a cw, exchange energy through an induced acoustic field. When the beat frequency of the laser beams equals acoustic (Brillouin) frequency, the pulsed beam experiences maximum amplification from the cw beam. By measuring the depleted cw beam and scanning the beat frequency of the two lasers, one obtains a Brillouin loss spectrum centered about the Brillouin frequency. The sensing capability of Brillouin scattering arises from the dependence of Brillouin frequency on the local acoustic velocity and refractive index in glass, which has a linear temperature and strain dependence [Zou et al., 2004]. This sensor can be installed along the length of the

reinforcement steel and by using pulse delay can detect the exact location of occurring corrosion. The optical fibre sensors have minimal risk of electromagnetic interference, high bandwidth, high sensitivity and are small in size. However, they are fragile, susceptible to damage on installation, expensive to install and needed to connect fibre optics sensors, and other optical equipment.
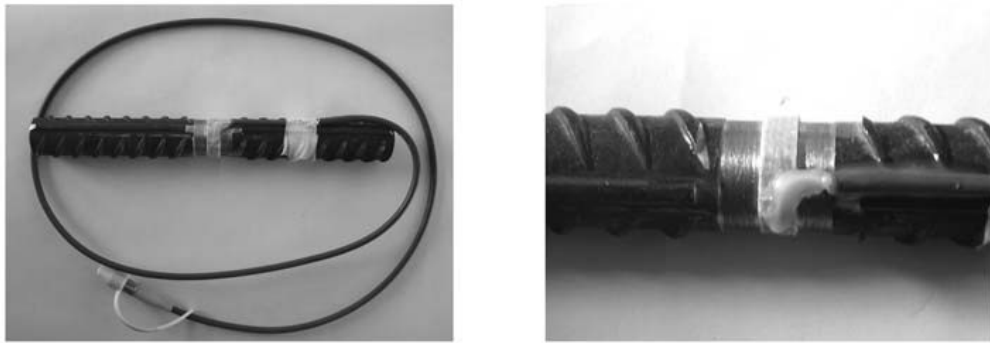
Figure 6.5. Optical fiber grating bound on surface of steel cylinder [Zheng et al., 2009].

6.2.7   Embedded corrosion instrument

Commercial embedded corrosion instrument by Virginia technologies inc. is an electronic corrosion sensor that monitors five key factors (linear polarization resistance, open circuit potential, resistivity, chloride ion concentration and temperature) in corrosion and communicates these through a digital network. Thus it provides real-time information on structural conditions. It integrates processing electronics with its sensors and thus can use digital communication. This eliminates data corruption by electromagnetic interference from power lines, radio waves and cellular telephones. It gathers and delivers all data without requiring inspectors to cut samples, interrupt use of a structure, or even visit the site [Virginia Technologies, Inc.]. As it is based on an active

powered wireless communication protocol, it faces the difficulty of recharging or replacing the batteries of the embedded sensors. This sensor is also expensive on a per-unit basis, making wide scale deployment costly.

Figure 6.6. Embedded corrosion instrument [Song & Saraswathy, 2007]

6.2.8 SensCore corrosion sensor

The SenCore corrosion sensor by Roctest measures two parameters of reinforced concrete structure: corrosion initiation and corrosion rate. These two measurements are performed at 4 different depths, between the concrete surface and the reinforcement steel depth. It is composed by 4 mild steel rebars that are anchored to a stainless steel support. The 4 dummy rebars are placed in the concrete at 4 different depths. The sensor is connected to a datalogger which transmits the measured data to a central unit. The connection between the datalogger and the central unit can be wireless or wired. For wired connection, the central unit provides power to the datalogger whereas for wireless connection the datalogger needs the power source of its own. The data can be saved in central unit's internal memory for manual retrieval or can be transmitted from the central unit by an ethernet connection to a local PC [Roctest corrosion sensor], [Roctest

datalogger], [Roctest centeral unit]. One of the major problems for the wireless SensCore humidity sensor is recharging or replacing the batteries of the datalogger.
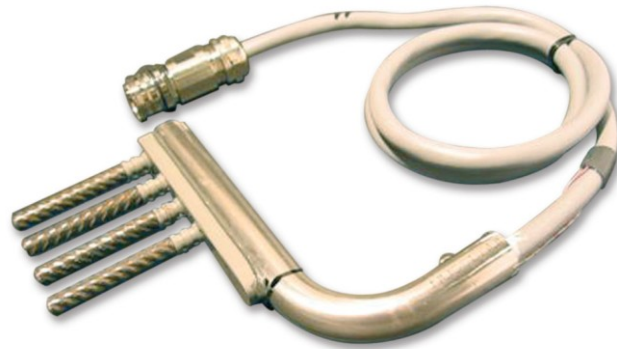
Figure 6.7. SensCore corrosion sensor [Roctest corrosion sensor].

6.2.9 Unpowered wireless corrosion sensor

This prototype sensor has been designed to be extremely simple and low cost. The sensors are embedded in the concrete, and are powered and interrogated through the use of inductively coupled magnetic fields. The sensor is a resonant circuit which is shown in Fig. 6.8 and comprises of two parallel capacitors connected by a wire. Initially the resonance of the sensor corresponds to the parallel combination of the two capacitors. As the transducer wire begins to corrode, the dip in the phase of the impedance becomes smaller. Once the wire is completely corroded, the second capacitor is removed from the circuit and the resonant frequency of the sensor is changed. The main advantage of this sensor is that it does not require any power source of its own. However, the sensor can only detect when a corrosion of threshold has been crossed. It cannot provide any intermediate information before corrosion reaches the threshold and disconnects the second capacitor from the sensor [Andringa, Neikrik, Dickerson, & Wood, 2005].
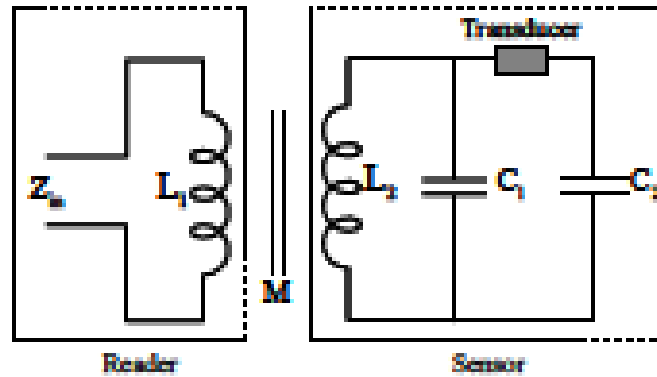
Figure 6.8. Circuit diagram of unpowered wireless corrosion sensor [Andringa et al., 2005] (© 2010 IEEE).

6.3 Coupled Coil Corrosion Sensor

In this chapter a coupled coil sensor that can detect the corrosion potential of reinforcement steel with respect to a reference electrode is presented. The reference electrode, which is immune to corrosion, is also embedded in the concrete. The sensor is powered and interrogated through the use of inductive coupling between the sensor coil and the interrogator coil. The sensor consists of an inductive coil connected in parallel with a varactor (voltage dependent capacitor) and reinforcement steel/reference electrode voltaic cell. When corrosion potential of reinforcement steel changes, the cell potential changes the capacitance, and therefore the resonant frequency of the sensor. The interrogator coil tracks the sensor's resonant frequency. As the sensor is passive and can be monitored wirelessly, it can be embedded in the concrete and can monitor the corrosion potential of reinforcement steel over the life time of the structure. The design of the sensor is simple and it is inexpensive to make and install. Therefore, this sensor has

75

the potential to find important application for corrosion assessment of reinforcement steel in concrete structures.

6.4 Sensor Operation

A block diagram of the coupled coil corrosion sensor is given in Fig. 6.9. Stainless steel is used as the reference electrode. In the sensor unit, an inductive coil is connected in parallel with a sensing element comprising the sensing circuit and reinforcement steel/stainless steel voltaic cell. The cell potential of the reinforcement steel/stainless steel voltaic cell is considered as the corrosion potential of reinforcement steel. A circuit diagram of this coupled coil sensor is shown in Fig. 6.10, and includes the interrogation circuit/coil coupled to it. The sensing circuit has a varactor whose small signal junction capacitance, C_j, in the reverse bias state is given by

$$C_j(V_C) = C_0(1 - V_C/\varphi)^{-\gamma},$$
(6.4)

where C_0 is the junction capacitance at zero bias, V_C is the reverse bias voltage, φ is the junction built in potential and γ is the doping profile factor. V_C depends on cell potential of the reinforcement steel/stainless steel voltaic cell, V_{cell}. So the capacitance of the varactor, C_j changes with V_{cell}. The reinforcement steel and stainless steel electrode are connected to the sensing circuit in a way so that when the reinforcement steel starts corroding, V_{cell} applies a negative voltage to the sensing circuit and sets the varactor in reverse bias state as in Fig. 6.10. The sensor coil and sensing circuit form a resonant circuit with a resonant frequency that depends on C_j and thus on V_{cell}. Assuming the losses are small and $C_l >> C_j$, the resonant frequency, f_0, of the sensor is approximated by

$$f_0 = \frac{\omega_0}{2\pi} = \frac{1}{2\pi\sqrt{L_S C_j(V_C)}},$$ (6.5)

where L_S is the inductance of the sensor coil. In the circuit R_3 and C_2 act as a low pass filter, M is the interrogator-sensor coil coupling factor, R_S is the series resistance of the sensor coil, R_{cell} is the cell resistance of the reinforcement steel/stainless steel voltaic cell, L_I is the inductance of the interrogator coil, R_I is the series resistance of the interrogator coil, V_G is the source amplitude and R_G is the source resistance. For small V_G, small M, and $R_{cell} \ll (R_2+R_3)$, $V_C \cong 0.99 V_{cell}$. Therefore, V_{cell} can be monitored by tracking the f_0 of the sensor. One of the important characteristics of this sensor is the high DC input impedance, $Z_s > 100$ MΩ, which prevents galvanic corrosion.
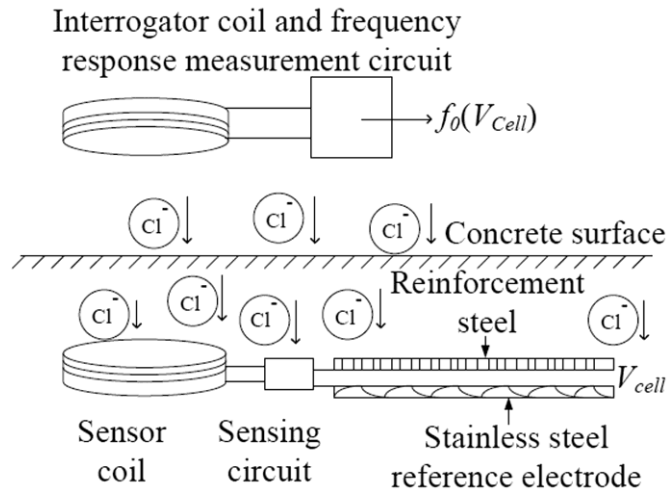
Figure 6.9. Block diagram of coupled coil corrosion sensor.
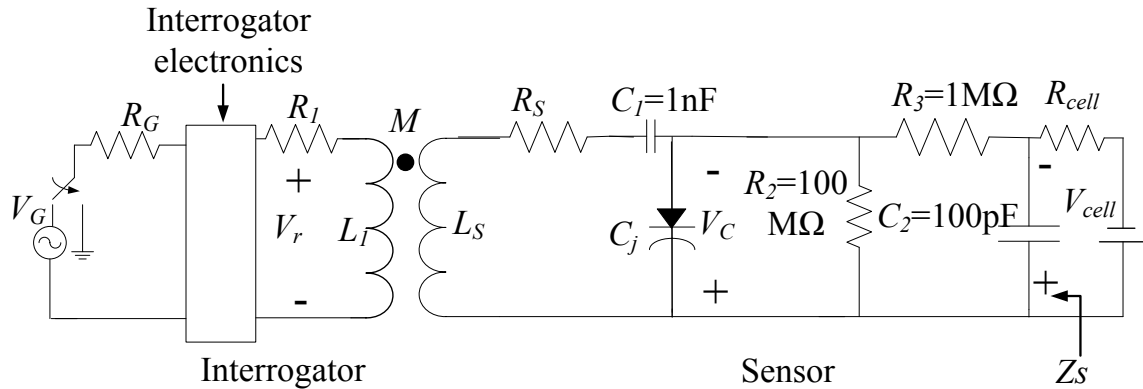
Figure 6.10. Circuit diagram of coupled coil corrosion sensor.

6.5 Interrogator and Sensor

For the interrogation of the sensor, the time-domain gating method described in chapter 3 was used. The instrumentation for interrogation was same as described in section 3.5. The sensor coil was made of insulated wire of 0.55 mm diameter formed as 19 turns of 8.4 cm diameter, producing L_s=66.98 µH and R_S= 11.72 Ω. The sensing circuit shown in Fig. 6.11 was fabricated on a 2 cm x 1 cm PCB board with surface mount capacitors and resistors. The varactor (NXP BB202) in the sensing circuit had a junction capacitance that varied in the range of 35.04 pF – 22.95 pF for reverse bias voltages between 0-1V, respectively.
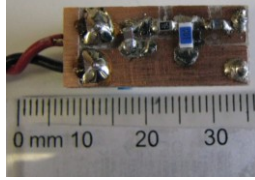
Figure 6.11. Sensing circuit for corrosion monitoring.

6.6   DC Calibration

Initially a DC voltage was applied directly to the sensing circuit using a power supply. The negative voltage applied to the sensing circuit was varied from 0 mV to 1000 mV. The sensor coil center was aligned concentrically with that of the interrogator coil with a separation distance, R= 14 cm and the source amplitude, V_G was set to 200 mV. Fig. 6.12 shows measured resonant frequencies of the senor as a function of negative voltages applied to the sensing circuit. It can be seen that the linear curve fits well with the measured resonant frequency values. The slope of the linear curve was 0.0183 MHz/25 mV. From the linear curve fitting eqn. 6.6 was obtained which relates the negative voltage applied to the sensing circuit, V to the resonant frequency of the senor, f_0. The error from the linear fit results from the non linear relation between C_j and V_C as seen from eqn. 6.4 and higher order parasitic. Note that the source impedance in this calibration is very small, whereas reinforcement steel/ stainless steel electrode the cell will have a larger source impedance.

$$V\ (mV) = 1368.87 f_0 (MHz) - 4524.80 .$$ (6.6)
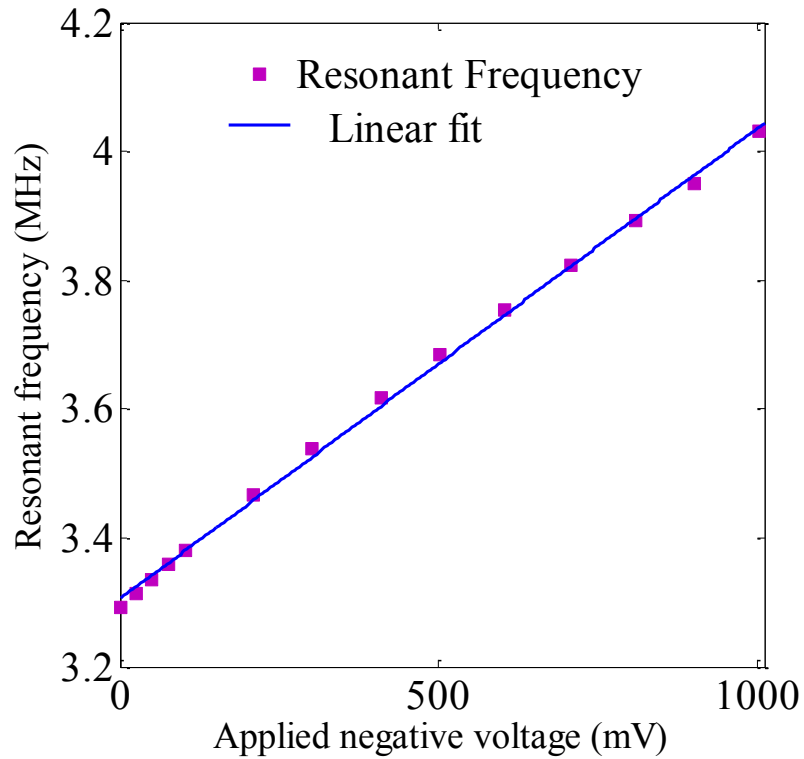
Figure 6.12. Resonant frequency versus negative voltage applied to the sensing circuit.

6.7   Accelerated Corrosion Test

The experimental set up for the accelerated corrosion test of a reinforcement steel /stainless steel cell embedded in mortar is shown in Fig. 6.13. For this test the sensor coil and sensing circuit were external. The reinforcement steel/ stainless steel electrode cell was connected to the sensing circuit and an A/D. The A/D was used to log the corrosion potential directly to a PC. The sensor coil center was aligned concentrically with that of the interrogator coil with a separation distance, R= 14 cm and the source amplitude, V_G was set to 200 mV.
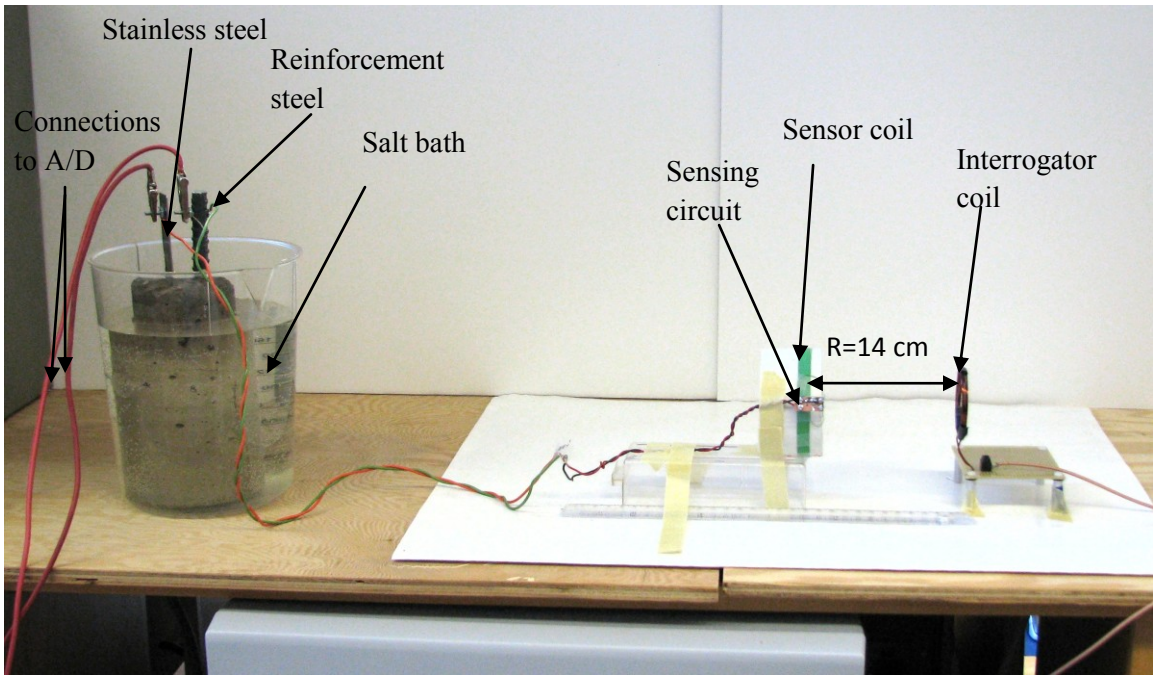
Figure 6.13. Experimental set up for accelerated corrosion testing.

6.7.1 Mortar Specimen

The cylindrical specimen was made from Quickrete mason mix (type S mortar, no. 1136). First the reinforcement steel /stainless steel pair was placed in the proper position in the cylindrical formwork. After thoroughly mixing 1.85 kg of mason mix with 285 gm of water, the mortar mix was placed in the cylindrical formwork (shown in Fig. 6.14a). The height and diameter of the mortar specimen were 17 cm and 7.5 cm respectively. The reinforcement steel bar was 20 cm long with 1.2 cm diameter, and the stainless steel electrode was 20 cm long and 2.4 cm wide with negligible thickness. The embedment length for the reinforcement steel/stainless steel pair was 14 cm. To guard against crevice corrosion, the reinforcement steel bar was painted with nitrile rubber at the end and in the region where it exits from the specimen block before embedding in the

mortar. The spacing between the reinforcement steel bar and the stainless steel electrode was 1.5 cm. After 10 days the specimen block was taken out of the formwork. Then the specimen was air cured for 26 days (shown in Fig. 6.14b). The sensing circuit was connected to the cell after the air curing. As stainless steel has a higher reduction potential than reinforcement steel, the reinforcement steel and stainless steel bars were connected to the negative and positive ends of the sensing circuit, respectively. The specimen was then submerged in water for 3 days and then in 5% NaCl solution for the remainder of the test as shown in Fig. 6.13.

Figure 6.14. (a) Mortar mix in the formwork.   (b) Specimen during air curing.

6.7.2   Results

The sensor's resonant frequency and the corrosion potential of the reinforcement steel, V_{cell} were monitored continuously. The corrosion potential of the reinforcement

steel was determined from resonant frequency using eqn. 6.6 (as obtained from the DC calibration). Fig. 6.15 shows the corrosion potentials from direct measurement of cell potential and from sensor's resonant frequency for 3 days in water and the first 11 days in the NaCl solution. The corrosion potential of the reinforcement steel started decreasing 2 days after submersion in NaCl solution, which indicated the presence of Cl^- ions inside the mortar specimen at the sensor location. It can be seen that for positive corrosion potentials the values obtained by direct measurement of cell potential are around 22 mV less than the values obtained by the sensor resonant frequency, whereas for negative corrosion potentials the values obtained by the direct measurement of cell potential are around 30 mV greater than the values obtained from the sensor resonant frequency. The possible reason for the offset difference is the finite resistance of the cell. The cell source resistance, R_{cell} was measured as R_{cell}=0.6 MΩ when V_{cell}= -367 mV. A very low source impedance was used in obtaining eqn. 6.6. Other possible sources for offset are errors in linear fit used to obtain eqn. 6.6, the precision of the power supply used for the DC calibration and the 5 mV resolution of the A/D which was used to log cell potential. The specimen was cleared open after the 11th day in NaCl solution. Fig. 6.16 shows the reinforcement steel had some corrosion product on its surface after the test.
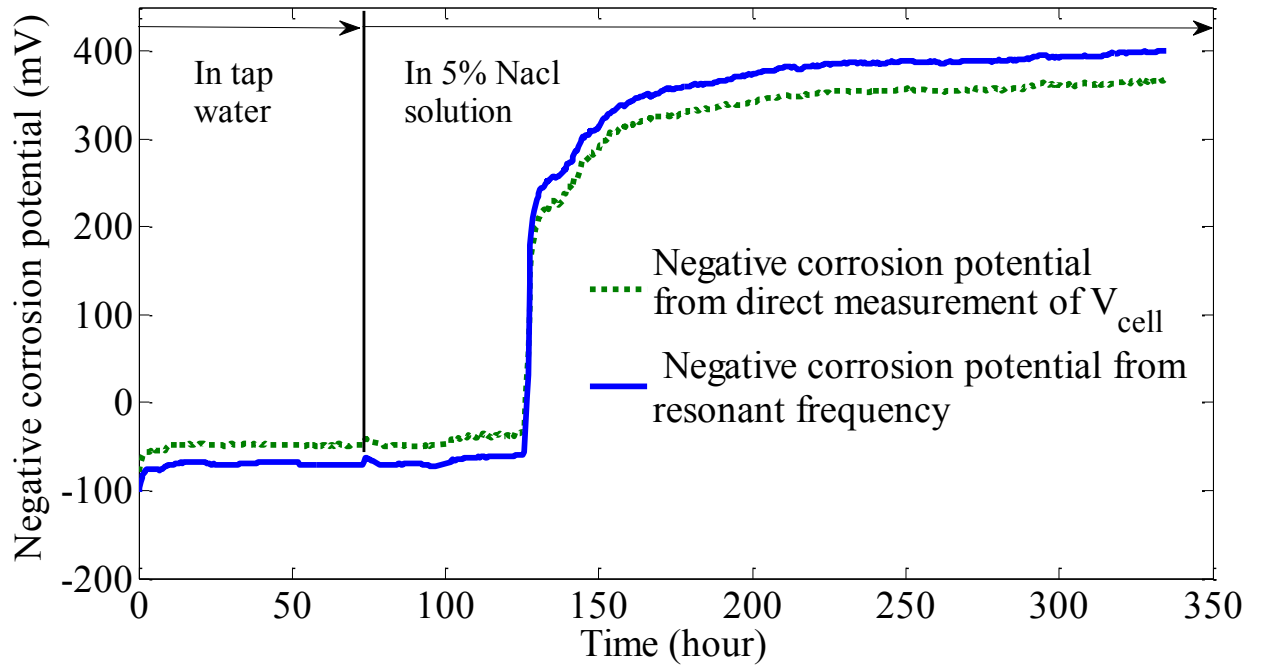
Figure 6.15. Corrosion potential of reinforcement steel from direct measurement of V_{cell}

and from sensor resonant frequency versus time.
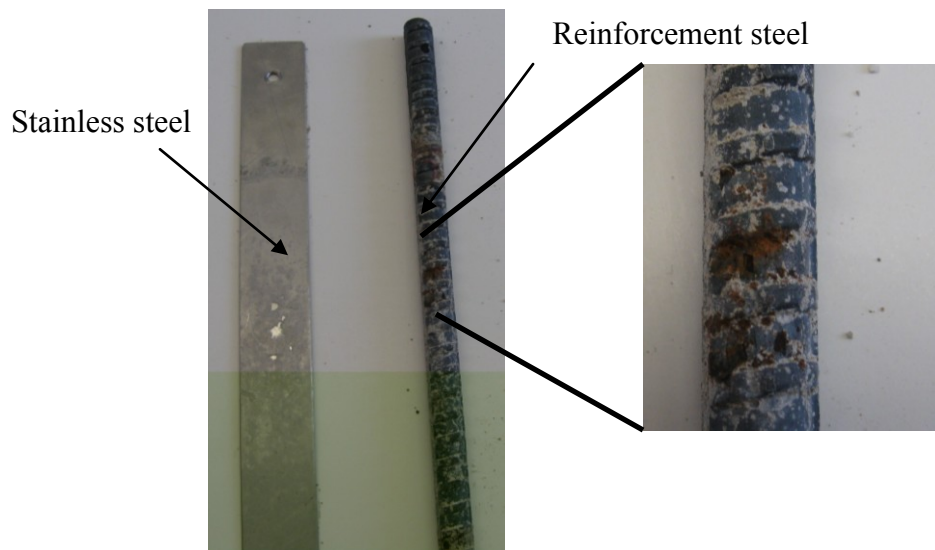
Figure 6.16. Reinforcing steel and stainless steel bars after removal from the mortar

specimen.

6.8   Sensor Performance

It is important to maintain a minimum separation distance between the interrogator coil and the sensor coil so that the coupling factor between them remains small. A small coupling factor is important to ensure the interrogator signal is small so that non-linear effects are minimal. However, as the separation distance between the sensor coil and the interrogator coil increases, the received signal amplitude from the sensor decreases as discussed in section 3.5. An experiment was conducted to measure the variation of the sensor's resonant frequency with the separation distance for our set up. Results showed that if the sensor coil center was aligned concentrically with that of the interrogator coil, any distance less than 8 cm pushes the varactor into a non-linear operating region. This problem can be avoided by a lower interrogator source signal. Table 6.1 lists the resonant frequencies for different distances when directly measured V_{cell} =-367 mV. A maximum separation distance of 18 cm was needed to maintain a measurement error less than 0.09%. This translates to a voltage resolution of 3.28 mV.

In practice, the sensor will be embedded in concrete structures and possibly surrounded by iron rebars and wire mesh. As the time-domain gating method was used for the interrogation technique, the sensor's resonant frequency should not be affected by any surrounding object. Fig. 6.17 shows the response of the sensor for different operating conditions, including monitoring through a concrete block (which shows no distinguishable difference).

Table 6.1. Variation of sensor's resonant frequency with distance.

Distance (cm)	Directly measured corrosion potential (mV)	Resonant frequency (MHz)	Corrosion potential from eqn. 6.6 (mV)
8	-367	3.5646	354.6740
10	-367	3.565	355.2215
12	-367	3.5652	355.4953
14	-367	3.5663	357.0011
16	-367	3.5671	358.0962
18	-367	3.567	357.9593
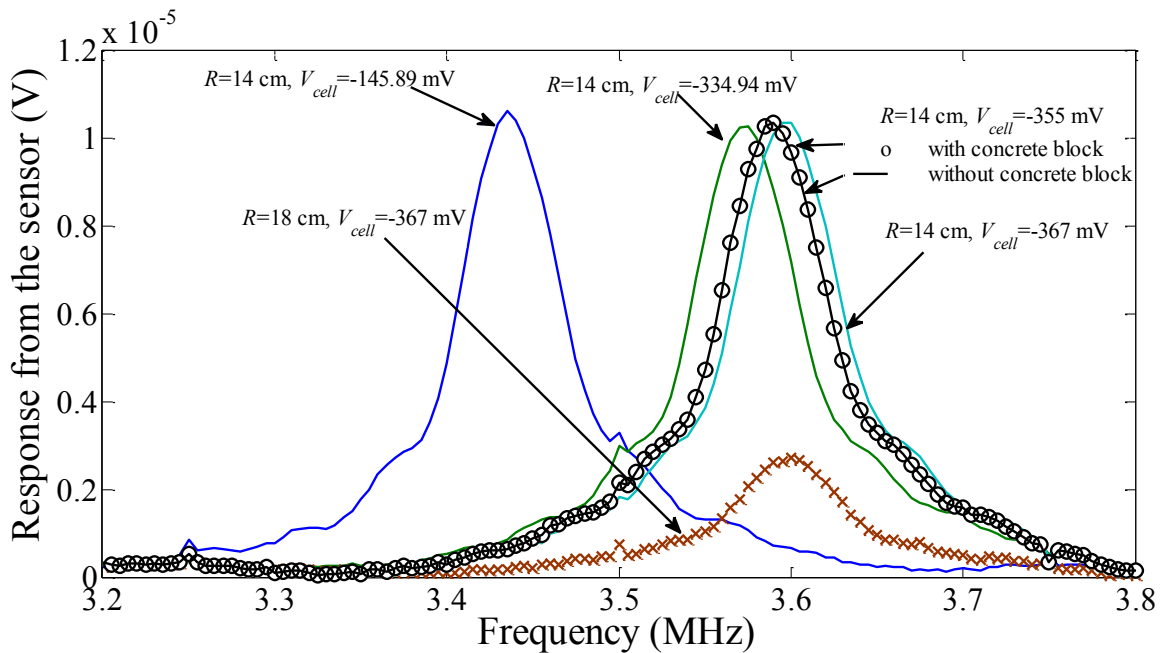
Figure 6.17. Response of the corrosion sensor for different operating conditions.

6.9   Embedded Corrosion Sensor

The experimental set up for measuring the corrosion potential with an embeddable coupled coil sensor is shown in Fig. 6. 18. The prototype embeddable sensor was constructed by hermetically sealing the sensor coil and the sensing circuit in a plastic cylinder as shown in Fig. 6.19. The coil has L_S= 60.53 µH and R_S= 10.52 Ω. The sensing

circuit was the same as described in section 6.5. Wires to connect the sensing circuit to the reinforcement steel/stainless pair or to the power supply were taken out of the container. Point where the wires came out of the container was sealed properly with epoxy. The interrogator, interrogation technique and instrumentation were same as described in section 6.5. The sensor coil center was aligned concentrically with that of the interrogator coil with a separation distance, R= 12 cm.
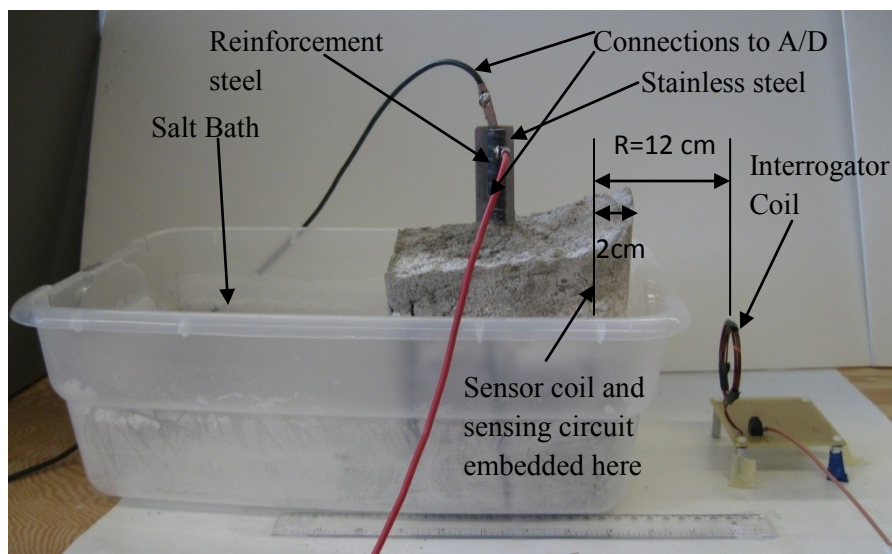
Figure 6.18. Experimental set up for accelerated corrosion test with the embedded corrosion sensor.
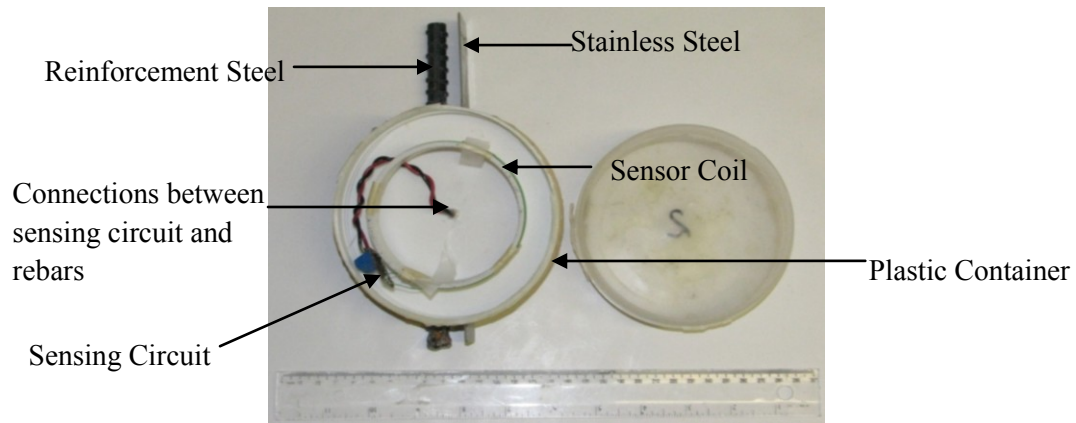
Figure 6.19. Embeddable corrosion sensor.

6.9.1 DC Calibration

A DC voltage was applied directly to the sensing circuit using a power supply. The negative voltage applied to the sensing circuit was varied from 0 mV to 325 mV. Fig. 6.20 shows the resonant frequency of the sensor, f_0 has a linear response to the negative voltage applied to the sensing circuit, V as

$$V(mV) = 1304.61 f_0(MHz) - 4207.25.$$ 　　　　　　　　　　(6.7)
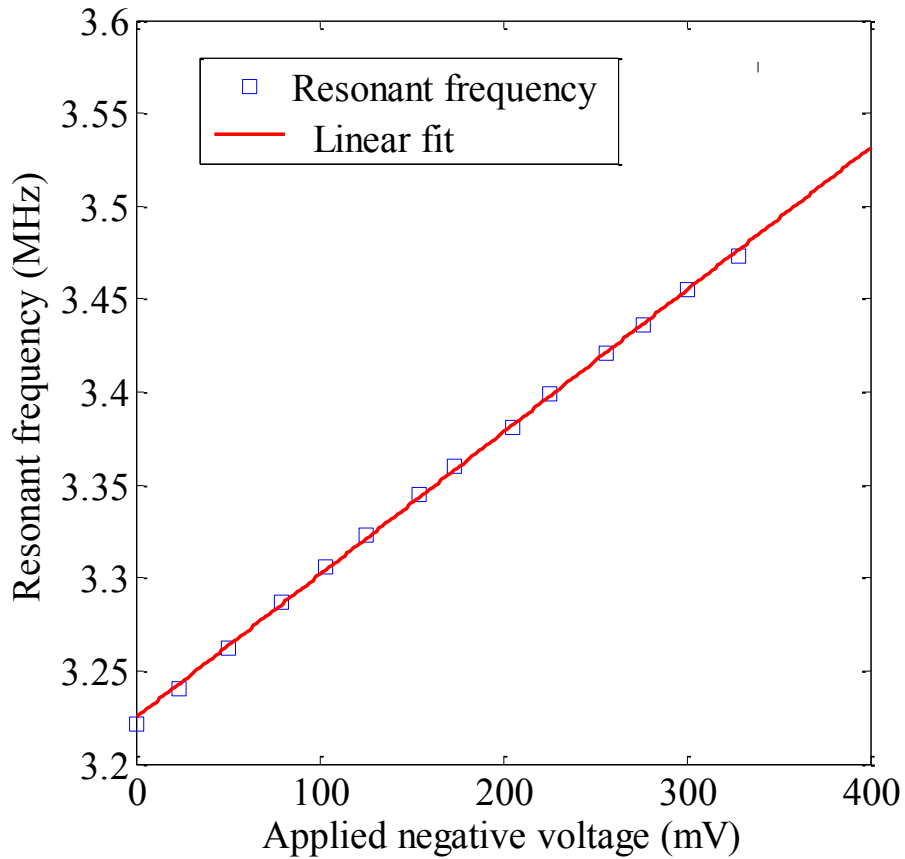
Figure 6.20. Resonant frequency versus negative voltage applied to the sensing circuit of the embedded sensor.

6.9.2 Accelerated Corrosion Test

The reinforcement steel/stainless steel electrode pair was connected to the sensing circuit. The wire connection spots on the reinforcement steel and stainless steel were coated with epoxy to prevent corrosion in this area. The specifications for the reinforcement steel/stainless steel pair were same as the ones described in section 6.7.1. The reinforcement steel and stainless steel bars were connected to the negative and positive ends of the sensing circuit, respectively. The reinforcement steel and stainless steel bars along with the sealed container were embedded in a 17cm x 15cm x 18.5cm

mortar specimen. The procedure to make the specimen was identical to the procedure described in section 6.7.1. The embedment length for the reinforcement steel/stainless steel pair was 14.5 cm. To guard against crevice corrosion, the reinforcement steel bar was painted with nitrile rubber at the end and in the region where it exits from the specimen block before embedding in the mortar. The spacing between the reinforcement steel bar and the stainless steel electrode was 1.2cm. The distance from the center of the sensor coil to the mortar surface was 2 cm. After 8 days, the specimen block was taken out of the formwork and air cured for 14 days. Fig. 6.19 shows the corrosion sensor and Fig. 6.18 shows the sensor embedded in the mortar block.

The specimen was submerged in water for 3 days and then in 5% NaCl solution for 11 days. The experimental set up for the accelerated corrosion test for the embedded corrosion sensor is shown in Fig. 6.18. The sensor's resonant frequency and the cell potential were monitored continuously. The corrosion potential of the reinforcement steel was determined from resonant frequency using eqn. 6.7. Fig. 6.21 shows the corrosion potentials obtained by direct measurement of cell potential and obtained from sensor's resonant frequency for 3 days in water and 11 days in the 5% NaCl solution. The corrosion potential of the reinforcement steel started decreasing 1 day after submersion in NaCl solution, which indicated the presence of Cl$^-$ ions inside the mortar specimen. It can be seen that the directly measured negative cell potentials are around 10 mV greater than the values obtained from the resonant frequency. As described previously possible reasons for the offset difference are the finite resistance of the cell, R_{cell} (measured value 0.72 MΩ for V_{cell}= -249 mV) rather than the low impedance used in obtaining eqn. 6.7,

errors in linear fit used to obtain eqn. 6.7, the precision of the power supply used for the DC calibration and the 5 mV resolution of the A/D which was used to log cell potential. The offset voltage value for the embedded sensor is lower than the offset voltage value for the sensor described in section 6.5. One possible reason for this is the errors in linear fit to obtain eqn. 6.7 are smaller than those in linear fit to obtain eqn. 6.6. Also, it should be noted that the distance between the sensor coil and the interrogator coil, R was smaller for the embedded sensor than that of the sensor described in section 6.5. The specimen was taken out from the salt bath after the 11th day and was dried for a week. The specimen was cleared to expose the sensor and the electrodes. Fig. 6.22 and Fig. 6.23 show rust formation on the surface of the reinforcement steel bar and the embedded sensor after the test, respectively.
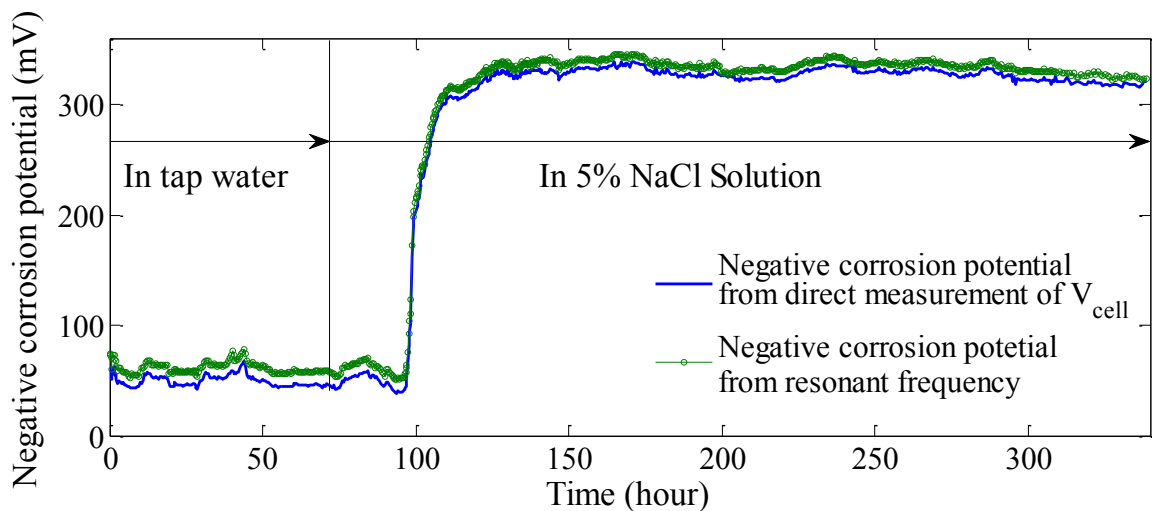
Figure 6.21. Corrosion potential of reinforcement steel from direct measurement of V_{cell} and embedded sensor resonant frequency versus time.
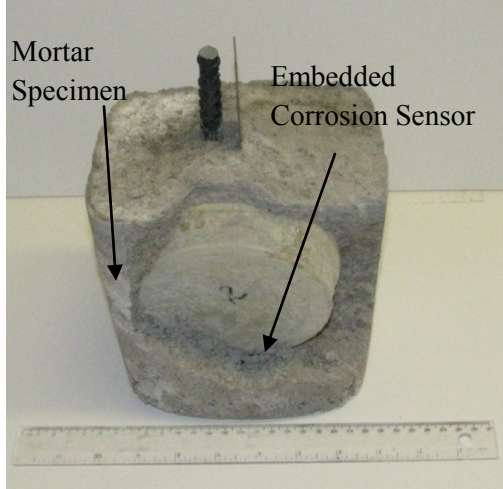
Figure 6.23. Concrete block while cracking.

Figure 6.22. Reinforcement steel after accelerated corrosion test.

6.10 Sensor Performance

Experiment results indicate that if the sensor coil center was aligned concentrically with that of the interrogator coil, a minimum separation distance, R_{min}=8 cm is required for tuning the capacitance of the varactor with the corrosion potential. Table 6.2 lists the resonant frequencies for different distances when V_{cell} =-249 mV. A maximum separation distance of 18 cm was needed to maintain a measurement error less than 0.14%. Fig. 6.24 shows the response of the sensor for different operating conditions.

Table 6.2. Variation of sensor's resonant frequency with distance.

Distance (cm)	Directly measured corrosion potential (mV)	Resonant frequency (MHz)	Corrosion potential from eqn. 6.7 (mV)
8	-249	3.4245	253.5379
10	-249	3.4263	255.8826
12	-249	3.4241	253.0169
14	-249	3.4254	254.7103
16	-249	3.4277	257.7063
18	-249	3.4289	259.2694
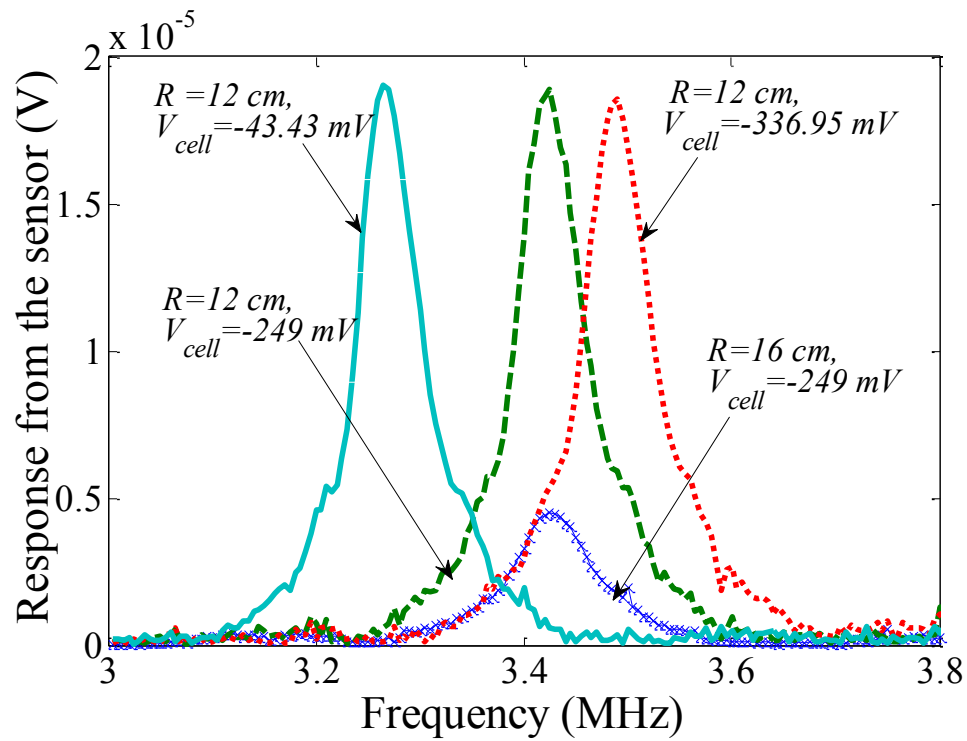
Figure 6.24. Response of the embedded corrosion sensor for different operating conditions.

Chapter 7: Coupled Coil pH Sensor

7.1 Introduction

pH is one of the essential parameters desired in a chemical sensor. pH is an important chemical parameter to monitor and control in numerous fields e.g. SHM, environmental monitoring, industrial processing applications, biomedical applications, chemical processing, etc. The value of pH is a crucial factor for assessing the deterioration and future performance of a reinforced concrete structure. When a structure is first built, a passive layer is formed on the surface of reinforcing bars. The surrounding concrete of the rebars are highly alkaline. In healthy concrete the pH is around 12.6 which helps to maintain this passive layer on the surface of the reinforcing bars. This passive layer protects the bars from corrosion. A pH value above 9.5 is required to maintain this passive layer on the surface of the rebars. Carbon dioxide gas (CO_2) in the atmosphere can be dissolved by the concrete pore solution and react with some calcium compounds to form carbonates. This lowers the pH of the concrete which results in depassivation of the rebars [Du et al., 2006], [Yeo et al., 2006]. Measuring pH of the soil is an important application of pH sensor for environmental monitoring. pH of soil, more precisely pH of the soil solution, is a factor that affects plant's absorption of different essential nutrients (Nitrogen (N), Potassium (K), and Phosphorus (P)) for growth and fighting off diseases. These nutrients are most available to plants when the soil pH is between 6 and 7. Acidic soil reduces the activity of the soil organic matters decomposing microorganisms, decreasing the liberation of nutrients. It also causes toxicity problems

due to Al^{3+} ions [Lemos et al., 2007], [Spector, 2001]. Another important application of pH in environmental monitoring is measuring the pH of water. In general, the lower the pH of water, the higher the level of corrosivity. Water with a low pH (<6.5) can contain elevated levels of toxic metals. This causes premature damage to metal piping and more importantly health risks. It also causes problems such as metallic or sour taste, staining of laundry, and the characteristic "blue-green" staining of sinks and drains. Water with high pH (>8.5) typically does not pose a health risk but causes problems like an alkali taste, formation of deposit on dishes, basins and formation of insoluble precipitates on clothing, etc [Fawell et al., 2003]. pH sensors are used extensively in food industry due to the importance of pH in food quality and production. Monitoring and controlling the pH value is very important in butter manufacturing processes for example, Cream is cooled after pasteurization at a very strict pH value of 6.70 to 6.85 to generate sweet butter. In order to manufacture sour butter, citric acid extracts are added to acidify the cream to 4.6-5.0 pH. Butter has to be acidified to a pH of 4.1 or less to ensure that pathogens are not multiplied. Otherwise it must be kept at temperatures below 5°C. A pH value of 4.0 to 5.8 is recommended for baked bread in order to prolong its shelf life. A pH value of 2.5 to 5.5 tends to prolong the shelf life of fresh fruit and inhibit the multiplication of micro-organisms. For ready-made food a pH value of around 4.5 is the simplest way to ensure the stability of the product [MBH Engineering Systems, 2008]. One of the most important application areas for pH sensors is bio-sensing. Development of biomedical sensor technology is becoming crucial as the health care system is facing an enormous challenge due to an ageing population and the need for continuous or intermittent

monitoring of different health parameters for diagnosis as well as treatment of diseases. pH sensors are found in different biomedical applications e.g. for *in vivo* monitoring of blood pH changes [Papeschi et al., 1981], *in vivo* measurement of oesophageal and gastric pH [Papeschi et al., 1984]. pH sensors also offer chemists a reliable tool to monitor the pH in chemical synthesis and sensitive reactions. Therefore, there is great demand for developing highly sensitive pH sensors with high accuracy and resolution.

7.2   Existing techniques for pH monitoring

7.2.1   pH Combination Electrode

It consists of a measuring sensing electrode and a reference electrode. The sensing electrode provides a potential proportional to the pH value of the sample and the reference electrode ideally provides a stable and consistent potential independent of the activity of the sample. Therefore, the pH combination electrode provides the potential difference between the reference and the sensing electrode, which is proportional to the pH of the sample. Common reference electrodes in use are Silver/Silver Chloride (Ag/AgCl) and Mercury/Calomel (Hg_2Cl_2). The Silver/Silver Chloride reference is the most frequently employed because it has universal applicability, a wide operating temperature range and is relatively non-toxic. The most common type of sensing electrode is the glass electrode [Reagecon, 2005]. A glass electrode consists of an electrode membrane that responds to pH, a highly isolating base material to support the unit, solution inside the glass electrode, an internal electrode, a lead wire, and a glass electrode terminal. The most critical item in this system is the electrode membrane. The membrane glass generates a potential that accurately corresponds to the pH of the

solution. Almost all electrodes can operate in the 1 to 12 pH range. Generally, silver chloride is used as the material for the internal electrode. Potassium chloride solution maintained at pH 7 is usually used as the internal solution. Glass pH electrodes have extremely high cell resistance from 50 to 500 MΩ. They are also fragile and not fit for measurement where the environment is highly alkaline. Glass electrodes are commercially available and are used widely in chemical and industrial applications. The combination electrode is connected to a high impedance voltmeter to measure the potential difference. pH meters are also used extensively with glass electrodes that display the measurements in pH units instead of volts.

Metal/Metal oxide electrodes have been developed as pH sensing electrodes because they are robust in structure, small in size and quick in response. The metal oxide electrodes developed for this purpose include oxides of Ir, Pt, Pd, Rh, Ti, Sn, Al, Ru, Os, Ta, Mo, W, Co, etc., among which iridium oxide is the most common one. Compared with other metal oxide electrodes, iridium oxide electrodes exhibit better stability in a wide pH range, higher resolution, and quicker response in high-temperature, high pressure, and aggressive media. They are not commercially available but found in different applications e.g. in situ measurement pH at the reinforcing steel/concrete interface [Du et al., 2006], *in vivo* monitoring of blood pH changes [Papeschi et al., 1981], *in* vivo measurement of oesophageal and gastric pH [Papeschi et al., 1984].
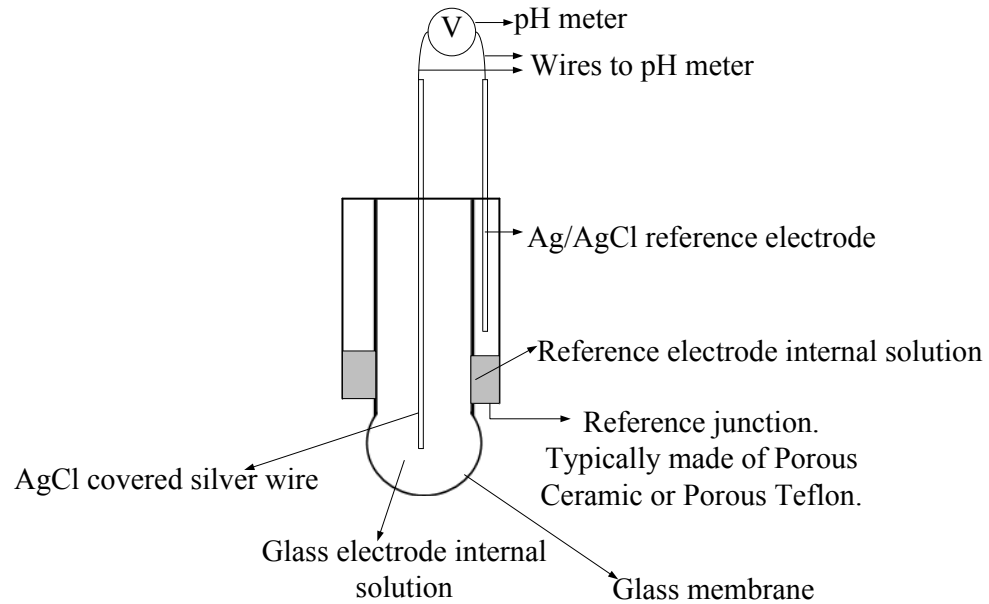
Figure 7.1. pH combination electrode with glass electrode as sensing electrode.

7.2.2 Ion sensitive field effect transistor or ISFET

ISFET pH probe is a non-glass solid state probe that uses a silicon transistor chip to measure pH values. In an ISFET the gate metal electrode of a MOSFET is replaced by an electrolyte solution which is in contact to a reference electrode. The metal part of the reference electrode is considered as the gate of the MOSFET. For the gate oxide, SiO_2 is used. This gate oxide is placed directly in contact with the electrolyte solution. In the ISFET, the source-drain current, I_d, flows from the drain to source via a channel. In a standard MOSFET the channel resistance depends on the electric field perpendicular to the direction of the current as well as on the potential on the gate oxide. Therefore, I_d is influenced by the interface potential at the oxide/aqueous solution. Although the electric resistance is a function of, and provides a measure for the gate oxide potential, the direct

measurement of the resistance is not able to provide the absolute value of this potential. However, for a fixed source-drain potential, V_{ds}, changes in the gate potential due to the oxide-aqueous solution potential can be compensated by modulation of an applied V_{gs} to the reference electrode. The adjustment to V_{gs} is carried out in such a way that the V_{gs} applied to the reference electrode are exactly opposite to the changes in the gate oxide potential for a fixed V_{ds} and I_d. This is performed by ISFET based amplifier circuit with feedback which allows obtaining constant source-drain current [Wroblewski, 2005]. The ISFET pH probe can be double or triple the cost of glass electrodes and they do not provide the stability and accuracy afforded by glass electrodes. They are highly temperature dependent and are not usually used in conjunction with chlorine or other chemicals. They work only with meters which are calibrated for ISFET based probes.
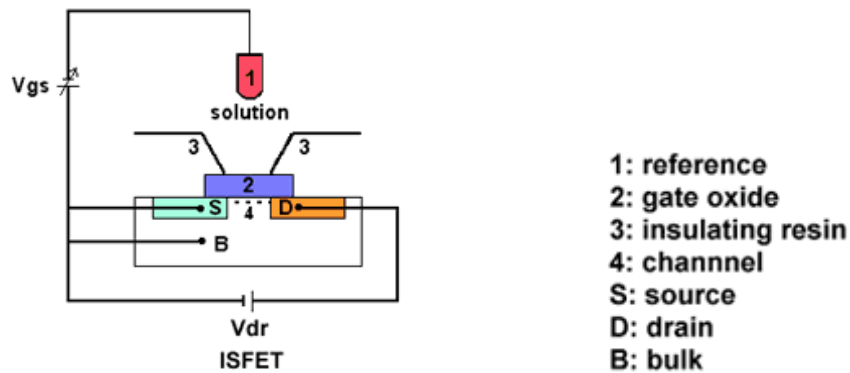
Figure 7.2. Schematic representation of an ISFET [Wroblewski, 2005].

pH combination electrode and ISFET probes require a wire connection to meter. For some applications, it can be difficult to get access to the solution needed to be measured. The need of an inspector in many applications also increases the cost and safety risk associated with the sensing.

7.2.3   Wireless passive pH sensor

Hydrogel-based LC sensor-The basic structure of this type of sensor is a passive LC resonator. Hydrogel is confined between a stiff porous membrane and a thin glass diaphragm. The diaphragm is the movable plate of a mechanically variable capacitor which is connected in parallel with an inductive coil. As small molecules of hydrogen ions pass through the porous membrane, the Hydrogel swells and deflects the flexible glass membrane. This results in a change of the resonant frequency of the sensor [Lei et al., 2004]. An interrogator coil, which is inductively coupled to sensor coil, keeps track of the sensor's resonant frequency.

Polymer-based magnetostrictive magnetoelastic sensor- This type of sensor is based on the acoustic vibration of a mechanical structure (usually a beam) in response to a magnetic field impulse. The vibration amplitude response is captured with a pick-up coil and converted to a frequency spectrum using an FFT algorithm, from which the resonant frequency of the sensor is determined. The resonant frequency of the sensor is a function of sensor length, density, elasticity and Poisson's ratio of sensor's material. Arrays of miniaturized magnetoelastic sensors can be made from Metglas alloy. The magnetoelastic sensors are coated with a pH responsive copolymer. Coating the sensor applies a mass load and changes the resonant frequency. As the mass load increases the resonant frequency decreases. Upon immersion in a liquid, the polymer swells as dependent upon solution pH, which increases the mass load on the sensor, lowering the resonant frequency [Jain et al., 2001].

pH sensor based on magnetic higher-order harmonic fields- This type of sensor is made of a magnetically soft film, acting as the sensing element, with an element providing a permanent DC magnetic field (biasing the sensing element) and sandwiching a reversibly swelling Hydrogel. Due to non-linearities, the sensing element generates higher-order harmonic fields when subjected to a low frequency ac magnetic field. The higher-order harmonic fields are detected with a remotely located detection coil. In the presence of a DC magnetic biasing field generated from the biasing element, the pattern of the higher-order harmonic magnetic fields vary depending on the field strength of the DC biasing field. The Hydrogel converts variations in pH into changes in its dimensions. This physically varies the separation distance between the sensing and biasing elements, resulting in a change in the biasing field experienced by the sensing element allowing remote pH measurement [Horton et al., 2009].

The common drawbacks of the Hydrogel-based LC sensor, Polymer-based magnetostrictive magnetoelastic sensor and magnetic higher-order harmonic fields based sensor are the long response time and the highly non-linear response [Horton et al., 2009], [Jain et al., 2001], [Sridhar & Takahata, 2009].

7.3 Wireless Passive Sensor Based on pH Electrode Potential Measurement

A wireless coupled-coil passive pH sensor for high-resolution remote pH monitoring is presented here. Improving the response time and achieving a linear response with high sensitivity over a large dynamic range were the key factors for

developing this new pH sensor. The sensor is based on a passive LC coil resonator whose resonant frequency is monitored remotely by measuring the impedance of an interrogator coil coupled to the sensor coil. The sensor consists of an inductive coil connected in parallel with a varactor (voltage dependent capacitor) and a pH combination electrode. When the pH of the contact solution changes, the resulting electrode potential changes the capacitance, and therefore the resonant frequency of the sensor.

7.4   pH Sensor Operation

A circuit diagram of the coupled coil pH sensor is shown in Fig. 7.3, and includes the interrogation circuit/coil coupled to it. In the sensor unit, an inductive coil is connected in parallel with a sensing element comprising the sensing circuit and the pH combination electrode. The sensing circuit has a varactor whose small signal junction capacitance, C_j, in the reverse bias state is given by

$$C_j(V_C) = C_0(1 - V_C/\varphi)^{-\gamma},$$

(7.1)

where C_0 is the junction capacitance at zero bias, V_C is the reverse bias voltage, φ is the junction built in potential and γ is the doping profile factor. V_C depends on the potential difference developed at the pH combination electrode in contact with a solution, V_{pH}. The capacitance of the varactor, C_j changes with V_{pH}. The sensor coil and sensing circuit form a resonant circuit with a resonant frequency that depends on C_j and thus on V_{pH}. Assuming the losses are small and $C_l >> C_j$, the resonant frequency, f_0, of the sensor is approximated by

$$f_0 = \frac{\omega_0}{2\pi} = \frac{1}{2\pi\sqrt{L_S C_j(V_C)}}, \tag{7.2}$$

where L_S is the inductance of the sensor coil. In the circuit R_3 and C_2 act as a low pass filter, M is the interrogator-sensor coil coupling factor, R_S is the series resistance of the sensor coil, R_{pH} is the cell resistance of the pH combination electrode, L_1 is the inductance of the interrogator coil, and R_1 is the series resistance of the interrogator coil. For a small source oscillation amplitude, small M, and $R_{pH} \ll (R_2 + R_3)$, $V_C \cong V_{pH}$. Therefore, V_{pH} can be monitored by tracking f_0 of the sensor. One of the important characteristics of this sensor is the high DC impedance, Z_s which prevents galvanic corrosion.
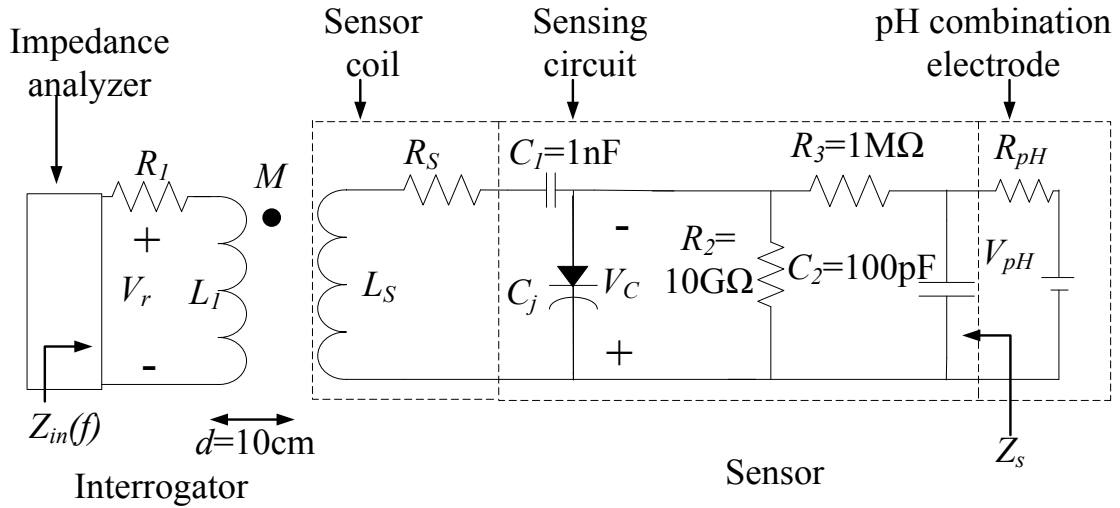
Figure 7.3. Equivalent circuit diagram of wireless passive pH sensor.

7.5 Interrogator and Sensor

For the interrogation of the sensor, the impedance measurement method described in section 2.2 was used where $Z_{in}(f)$ is measured using an impedance analyzer (Agilent 4294A). The instrumentation and interrogator coil for interrogation was same as described in section 2.2.3. The voltage oscillation level of the impedance analyzer was set to 25 mV. The sensor coil was made of insulated wire of 0.55 mm diameter formed as 19 turns of 8.4 cm diameter, producing measured L_s=66.98 µH and R_S= 11.72 Ω. The sensing circuit, which is shown in Fig. 7.4, was fabricated on a 2.8 cm x 1 cm PCB board with surface mount capacitors and resistors. The varactor (NXP BB202) in the sensing circuit had a junction capacitance that varied in the range of 35.04 pF – 22.95 pF for reverse bias voltages between 0-1V, respectively. PHE-4201 (by Omega Engineering, Inc.) was used as the pH combination electrode. For measurements the sensor coil center was aligned concentrically with that of the interrogator coil with a separation distance, R= 10 cm. The experimental set up for measuring pH of a solution with the coupled coil pH sensor is shown in Fig. 7.5.
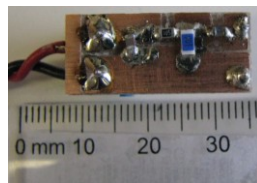
Figure 7.4. Varactor-based sensing circuit.
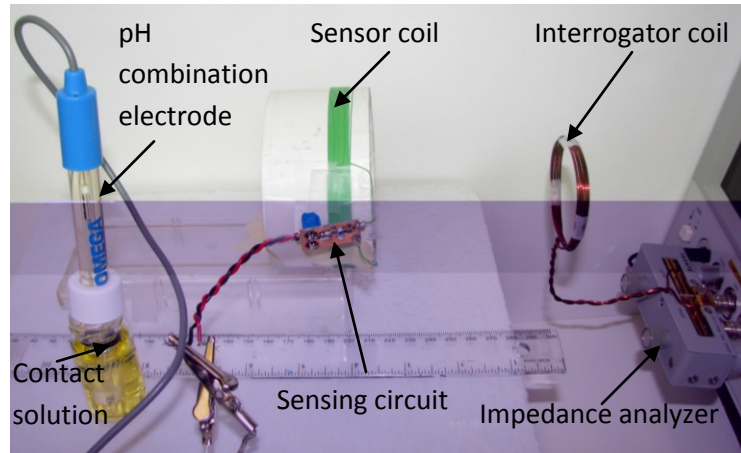
Figure 7.5. Experimental set up for wireless coupled coil pH sensor.

7.6 pH Sensor Experiment and Result

Solutions of different pH were made with pH hydration buffer capsules (Micro essential laboratory) and measured with a pH-meter (VWR sympHony). First, the voltage difference developed at the pH combination electrode, V_{pH}, was measured with a high input impedance HP 3455A digital voltmeter for the different pH solutions. Fig. 7.6 shows the V_{pH} has a very linear response, with a maximum deviation of < 0.05 pH from the linear fit, which is given by eqn. 7.3. Also, R_{pH} was measured employing a DC load test, which measured the change in current from the battery while measuring the voltage drop. Table 7.1 lists the R_{pH} for different pH solutions indicating the combination electrode has a source impedance of approximately 100 MΩ. This is approximately 1% of the sensor impedance of $Z_S \sim 10$ GΩ.

$$V_{pH}(mV) = -56.25\,pH + 395\,. \tag{7.3}$$

Table 7.1. R_{pH} for different pH solutions.

pH	R_{pH} (MΩ)
4.01	96.70
6.27	95
6.6	70
6.75	122.22
7.02	110.76
7.21	128.57
7.3	110
7.42	115.38
7.52	125
7.65	110.52
7.75	122.22
7.87	117.57
8.11	113.11
10.02	109.75
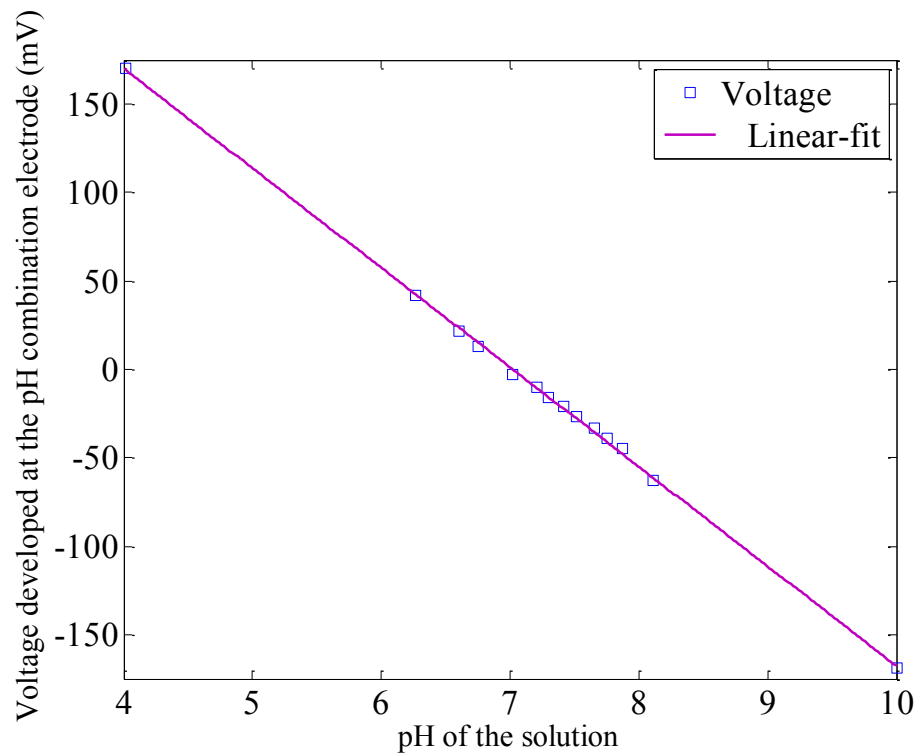
Figure 7.6. Voltage difference developed at the pH combination electrode versus measured pH

of the contact solution.

106

Fig. 7.7 shows the measured resonant frequency for different pH solutions. A linear fit given by eqn. 7.4 over the 4-10 pH dynamic range indicates a sensitivity of 50 kHz/pH with a maximum deviation of <0.1 pH from the linear fit. As observed in previous sensors, section 6.6, there is a small second order non-linearity observed in the result. The resonant frequency was measured three times for each solution with a maximum deviation of 1.2 kHz (0.024 pH) for all the measurements.

$$f_0\,(\text{MHz})=0.050pH+2.951. \tag{7.4}$$
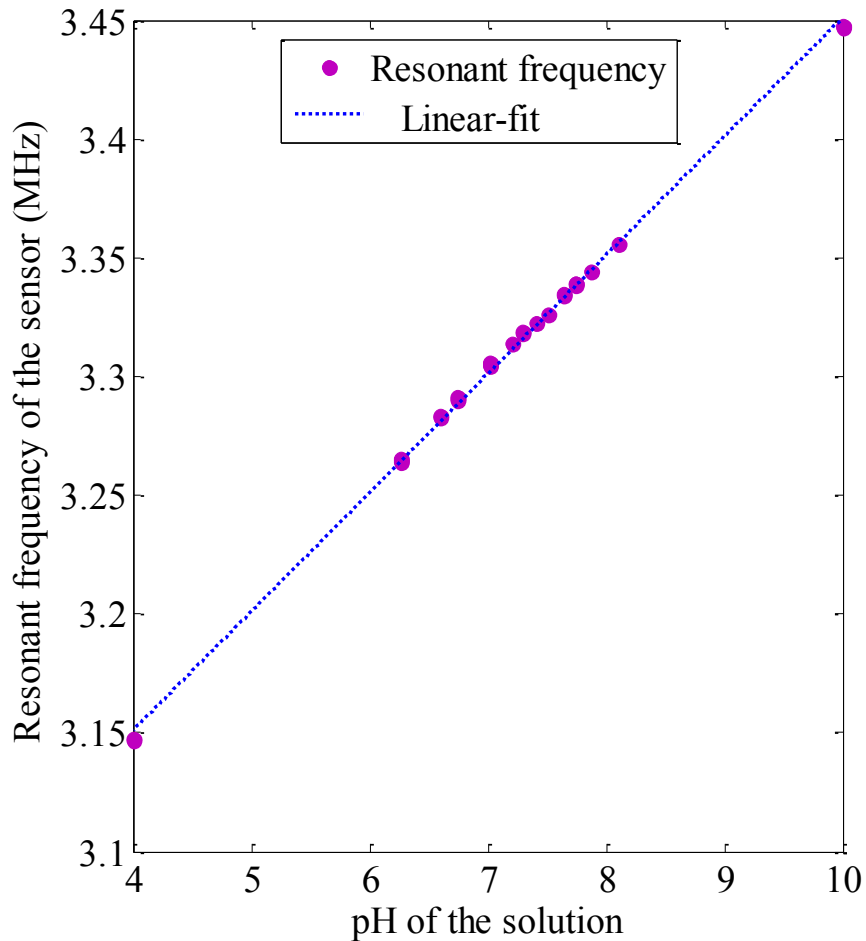
Figure 7.7. Resonant frequency of the sensor versus measured pH of the contact solution.

7.7   DC Test and Effect of R_{pH}

Using a high precision power supply, a specified voltage was applied to the sensing circuit and resonant frequency of the sensor was measured. The power supply has a low source resistance. So an external resistance, which was equal to R_{pH}, was added to mimic the actual source resistance of the combination electrode as the source resistance and resonant frequency of the sensor was measured. Fig. 7.8 shows the resonant frequency of the sensor as a function of voltage applied to the sensing circuit from power supply (with and without the added source resistance) and pH combination electrode. Results show that there is no significant difference between the resonant frequencies when the voltage was applied using a power supply with and without the source resistance. This indicates that R_{pH} does not have significant effect on the sensor's resonant frequency. However, the resonant frequencies for the voltage applied using a pH combination electrode shows a small deviation from those for voltages applied using a power supply, especially at pH=4.01. The possible reasons for this deviation are the cable connecting the pH combination electrode to the sensing circuit, and the sensor being highly sensitive to the surroundings when connected to the pH combination electrode. Also the precision of the power supply, contamination of the solutions, loading effect of the voltmeter and the accuracy of the V_{pH} measurement should be taken into consideration.
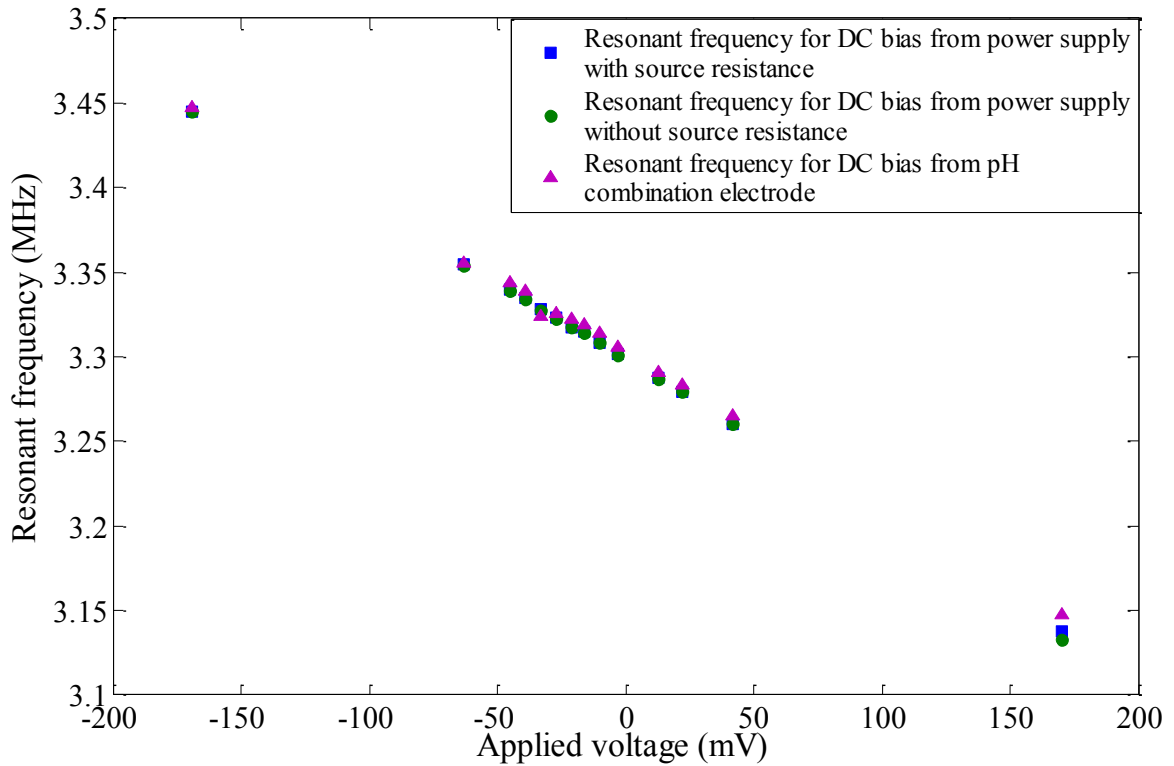
Figure 7.8. Resonant frequency versus voltage applied to the sensing circuit.

7.8 Sensor Performance

It is important to maintain a minimum separation distance between the interrogator coil and the sensor coil to ensure a small V_{osc} for linear operation of the varactor. Also, as the separation distance between the sensor coil and the interrogator coil increases, the received signal amplitude from the sensor decreases. An experiment was conducted to measure the variation of the sensor's resonant frequency with the separation distance for the set up. Results show that if the sensor coil center was aligned concentrically with that of the interrogator coil, any distance less than 8.5 cm pushes the varactor into a non-linear operating region. Table 7.2 lists the resonant frequencies for

different distances when measured pH of the solution is 7.02. A maximum separation distance of 18 cm was needed to maintain a measurement error less than 0.08%.

Table 7.2. Variation of sensor's resonant frequency with distance.

Distance (cm)	pH of the contact solution (pH meter)	Resonant frequency (MHz)	pH of the contact solution (from eqn. 7.4)
8.5	7.02	3.3051	7.08
10	7.02	3.3055	7.09
12	7.02	3.3057	7.09
14	7.02	3.3068	7.12
16	7.02	3.3076	7.13
18	7.02	3.3075	7.13

Fig. 7.9 shows the frequency response of the sensor for different operating conditions. The response time of the sensor was less than 30 s for each frequency sweep. An experiment was also conducted to show the variation of minimum separation distance with the voltage oscillation level of the impedance analyzer, V_{osc}. Table. 7.3 lists the minimum separation distance, R_{min} and the resonant frequency at R_{min} for different V_{osc} indicating the R_{min} can be decreased by lowering V_{osc}.
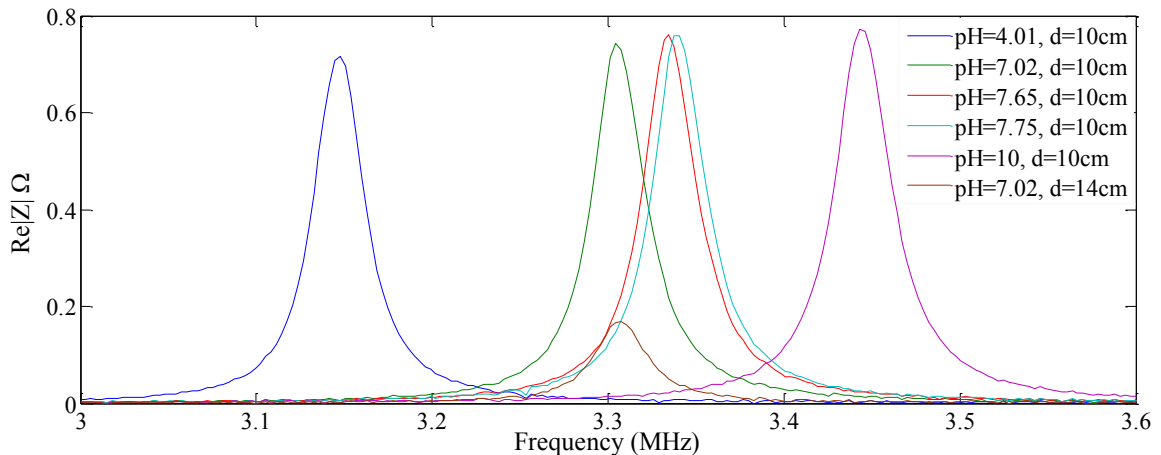
Figure 7.9. Frequency response of the pH sensor for different operating conditions.

Table 7.3. R_{min} and the resonant frequency at R_{min} for different $V_{osc.}$

V_{osc} (mV)	R_{min} (cm)	Resonant frequency at R_{min} (MHz) for pH=7.02
50	11	3.3047
40	9.7	3.3042
30	8.8	3.3058
25	8.5	3.3055
20	7	3.3061
10	6	3.3052

A wireless passive pH sensor based on pH electrode potential measurement is described. This simple and cost effective sensor was based on a passive LC coil resonator. pH of different solutions can be wirelessly monitored by measuring the change of sensor's resonant frequency. Results obtained from the experiment exhibited a linear relationship between resonant frequency of the sensor and pH of the contact solution over a 4 to 10 pH dynamic range. A 50 kHz/pH sensitivity and 30 s response time were achieved with a 0.1 pH resolution. This sensor will find applications for remote pH monitoring in numerous fields.

Chapter 8: Conclusions and Future Works

The research studied coupled coil sensors for remote passive monitoring applications. In the first part of the thesis an interrogation technique for coupled coil resonant sensors employing time-domain gating was demonstrated. Results for the C_P-G_P sensitive sensor showed that this technique could measure the f_0 or the Q factor of the sensor enabling determination of the change of C_P or G_P. It provided extended interrogation distance/improved accuracy in the determination of the resonant frequency and eliminated the response from the interrogator coil, the exciting signal and surrounding objects. Thus it was not as sensitive to the surrounding environment compared to the impedance measurement technique. The time-domain gating method was used to determine the resonant frequency of a relative humidity sensor. Results show a linear relationship between the capacitance of the sensor and the relative humidity with a 0.594 pF/%RH sensitivity. This sensor was able to detect changes in %RH with less than 2% error.

An embedded coupled coil low cost prototype sensor that can detect the corrosion potential of reinforcing steel was described in the second part of the thesis. An accelerated corrosion test was performed using the sensor. Results of the test indicate that corrosion potential could be monitored with a resolution less than 10 mV and with 19 kHz/25 mV sensitivity. This embedded corrosion sensor can remotely monitor the corrosion potential of reinforcing steel and has potential to assess the corrosion state of reinforcing steel.

The last part of the thesis described a coupled coil pH sensor based on pH electrode potential measurement. A linear response over a 4 to 10 pH dynamic range and 50 kHz/pH sensitivity were achieved with a 0.1 pH resolution. A 30 s response time of this sensor overcomes the long response time and highly nonlinear response of polymer based passive pH sensors.

In the present work an RF lock-in amplifier was used as received signal detector for the time-domain gating interrogation technique. However, the response spectrum measured with the lock-in amplifier does not directly provide the Q of the sensor. To obtain the Q, the received signal in the time-domain was observed with an oscilloscope and fitted with a function of the form $Ae^{-t/\tau} sin(2\pi f_0 + \phi)$ with unknown parameters A, τ, f_0, and ϕ. From τ and f_0, Q is determined. Future research can explore a detector that can provide f_0 and Q directly from the time-domain response. A portable interrogator for the corrosion sensor would enable the corrosion sensor to be tested in the field. The pH combination electrode used in the current pH sensor is not suitable for SHM application because of fragility and large size. A new pH combination electrode pH105 (by ExStik), which is specially made for monitoring pH of the concrete is commercially available as an alternative. In future an embedded pH sensor can be made with this electrode and research used to measure the pH of concrete structures.

Appendix A

MATLAB® Code

A.1 Quadratic Curve-fitting Algorithm for Determining Resonant Frequency

```matlab
%fit.m
%Written by Sharmistha Bhadra
%29 August, 2009

clearvars

% f contains the frequency vector
f=[
]
% v contains the received signal voltage or the impedance response
vector
v=[
];

% Converting the reived signal or the impedance response to power. p is
the
% power vector
for i=1:100
    p(i)=v(i)*v(i);
end

%a contains the maximum power value
a=max(p)
j=1;

% Include points  where power >=0.5a. l and fi vector contains the
power
% and frequency respectively for all those points. Fit 1/l against fi
% to a parabola (ax^2+bx+c). Resonant frequency=-b/(2*a)
for i=1:200
    if p(i)>=a/2
        l(j)=p(i)
        fi(j)=f(i);
        pin(j)=1/p(i);
        j=j+1;
    end

end
p8 = polyfit(fi,p,2);
f_resonant=-p8(2)/(2*p8(1))
```

A.2 Determining Self Inductances of the coils and Mutual Coupling Between the Coils

```matlab
%indcal.m
%  calculate L and M for 2 coaxial coils;
%


%
%experiment m
%dmean contains the distance between the interrogator coil and the
sensor
%coil in meter
dmeas=[0.1 0.15 0.17 0.2 0.22 0.25 0.30];

%Signal at resonance for different distances
zrmeas=[2.03896845E-03
2.50096690E-04
1.07263567E-04
4.21000000E-05
2.45957353E-05
1.18175896E-05
4.53609847E-06

];
m2mnorm=zrmeas/zrmeas(1);
%
% values in meters
%
u0=4*pi*1e-7;
% n1 is the number of turn for the interrogator coil, r1 is the radius
of
% the interrogator coil and rw1 is the radius of the wire of the
% interrogator coil
n1=5;
r1=0.0255;
rw1=0.0006;
sig1=5.8e7;
% n2 is the number of turn for the sensor coil, r2 is the radius of
% the sensor coil and rw2 is the radius of the wire of the
% sensor coil
n2=19;
r2=0.042;
rw2=2.74e-4;
sig2=5.8e7;
%
freq=3.4122e6;
%
   wrad=freq*2*pi;
   sk1=1.0/sqrt(pi*freq*u0*sig1);
   res1=(n1*2*pi*r1)/(sig1*sk1*2*pi*rw1);
   sk2=1.0/sqrt(pi*freq*u0*sig2);
```

```matlab
    res2=(n2*2*pi*r2)/(sig2*sk2*2*pi*rw2);
    res1
    res2
%
%   self inductance
%
%
    k2=(4*r1*(r1-rw1))/((2*r1-rw1)*(2*r1-rw1));
    k=sqrt(k2);
    [ke,ee]=ellipke(k2);
    lfe=((2/k-k)*ke-(2/k)*ee);
    ind1=n1*n1*u0*sqrt(r1*(r1-rw1))*lfe;
%
    k2=(4*r2*(r2-rw2))/((2*r2-rw2)*(2*r2-rw2));
    k=sqrt(k2);
    [ke,ee]=ellipke(k2);
    lfe=((2/k-k)*ke-(2/k)*ee);
    ind2=n2*n2*u0*sqrt(r2*(r2-rw2))*lfe;
%
    ind1
    l1app=n1*n1*u0*r1*(log(8*r1/rw1)-2)
    l1bapp=n1*n1*u0*pi*r1/2;
    ind2
    l2app=n2*n2*u0*r2*(log(8*r2/rw2)-2)
    l2bapp=n2*n2*u0*pi*r2/2;
%
%   mutual inductance
%
for j=1:7
    dist=dmeas(j);
    drm(j)=dist;

%
    k2=(4*r1*r2)/(dist*dist+(r1+r2)*(r1+r2));
    k=sqrt(k2);
    [ke,ee]=ellipke(k2);
    mfe=((2/k-k)*ke-(2/k)*ee);
    mut=n1*n2*u0*sqrt(r1*r2)*mfe;
    mm(j)=mut;
    m2num(j)=mut*mut;
%
    mmapp(j)=n1*n2*(u0*pi*r1*r1*r2*r2)/(2*dist*dist*dist);
    l1rm(j)=ind1;
    l2rm(j)=ind2;
%
end
%
m2nnorm=m2num/m2num(1);
%
%
plot(drm*100,m2nnorm,'-',dmeas*100,m2mnorm,'--');

%
```

A.3 MATLAB®/Simulink Model of Lock-in Amplifier

The time-domain received signal is fed into input port 1. The lock-in frequency is set to the frequency. Harmonic is set to 1. The simulation is run for 1 s. The R value is shown in the Display.
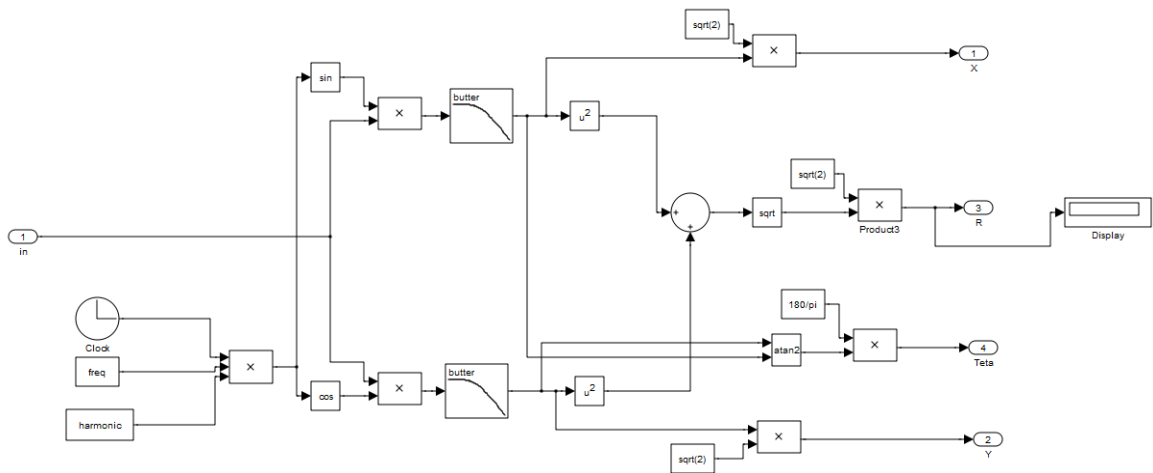
Figure A.1. Schematic for Simulink model of lock-in amplifier.

Appendix B

B.1 User's Guide to the LabVIEW® 7.1 Program for Time-domain Gating

As shown in Fig. B.1, a shortcut to execute the LabVIEW® 7.1 program called progfile.vi is located on the host PC's desktop. First this progfile.vi icon is needed to be clicked. After clicking, the front panel will appear on the screen which is shown in Fig. B.2.

Figure B.1. Shortcut to progfile.vi showing on the desktop of host PC.

Parameters needed to be specified in the front panel for the frequency sweep. How many times the sweeping will be done is specified in No. of Iteration field. Each sweeping will be done in 10 minutes interval. Sweeping number starts with 0. Each sweeping will be saved in one .xls file. The file location is specified in Path field. The file name is specified in File Name field. The file's name format is File Name followed by the sweeping number. The amplitude of the source is specified in the Amplitude field. The unit of the amplitude is V_{p-p}. In the Start and Stop Frequency field the start and stop

frequency of the sweeping needed to be defined. There is option to choose the unit (kHz/MHz) for these frequencies. The number of measurement points between the start and stop frequency is specified in Number of Samples field. After specifying all these parameters clock the run button on the top of the front panel. The sweeping will start and once the sweeping is done the file will be saved in the specified directory.
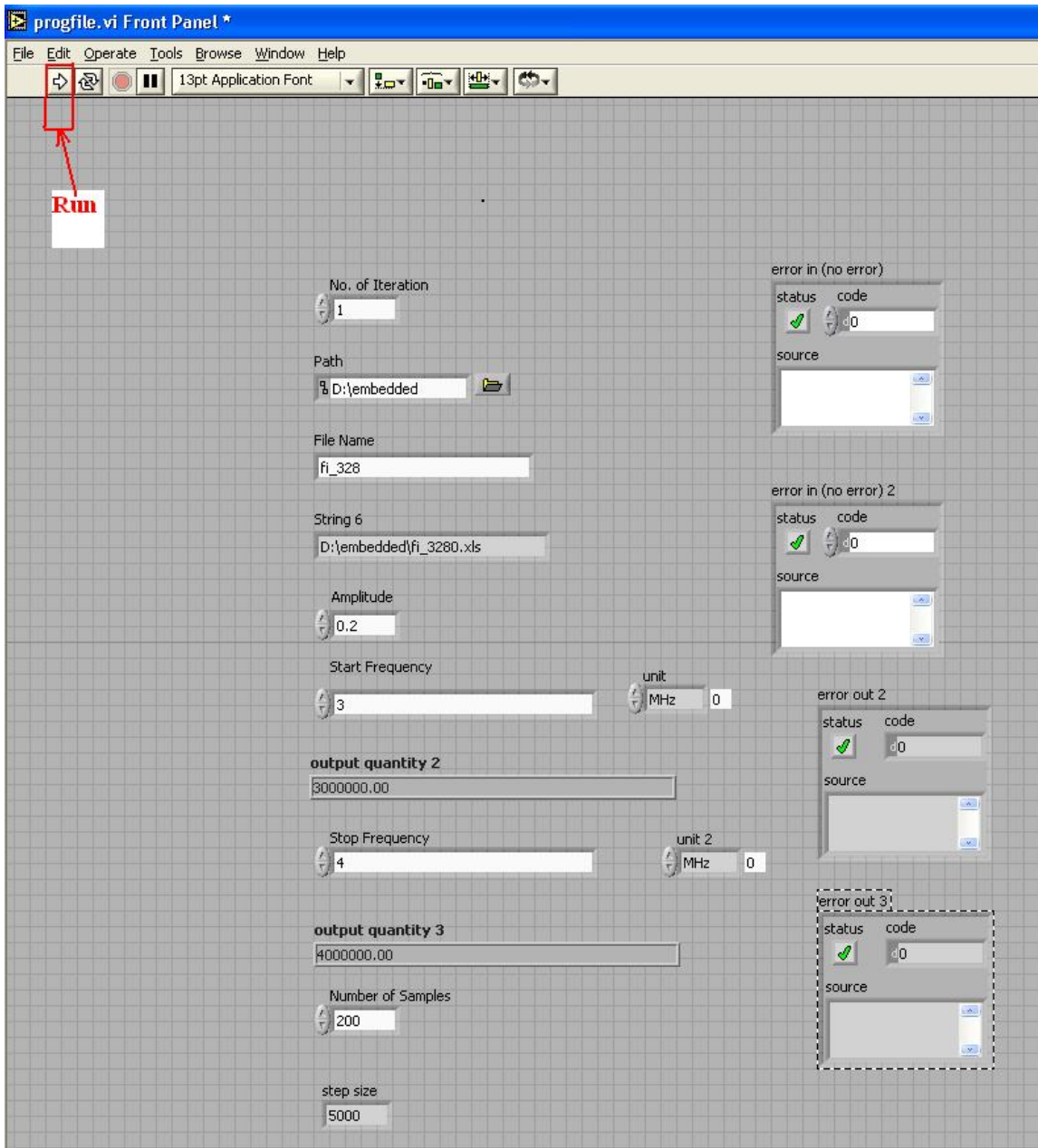
Figure B.2. Front panel of progfile.vi.

References

1. Andringa, M. M., Neikrik, D. P., Dickerson, N. P., & Wood, S. L. (2005). Unpowered wireless corrosion sensor for steel reinforced concrete. *IEEE Sensors* , (pp. 155-158).

2. Anup, H. (1983). *Corrosion of Reinforcement in Concrete Construction.* (A. P. Crane, Ed.) Chichester: Ellis Horwood Ltd.

3. Apostolopoulos, C. A., & Papadakis, V. (2008.). Consequences of steel corrosion on the ductility properties of reinforcement bar. *Construction and Building Materials , 22* (12), 2316-2324.

4. Bornehag, C. G., Blomquist, G., Gyntelberg, F., Järvholm, B., Malmberg, P., Nordvall, L., et al. (2001). Dampness in buildings and health. *Indoor Air , 11* (2), 72–86.

5. Buff, W. (2002). SAW sensors for direct and remote measurement. *IEEE Ultrasonic Symposium*, *1*, pp. 435 - 443.

6. Butler, J. C., Vogliotti, A. J., Verdi, F. W., & Walsh, S. M. (2002). Wireless, passive, resonant-circuit, inductively coupled, inductive strain sensor. *Sensors and Actuators A , 102* (1), 61-66.

7. Cabrera, J. G. (1996). Deterioration of concrete due to reinforcement steel corrosion. *Cement and Concrete Composites , 18* (1), 47-59.

8. Cai, Q. Y., & Grimes, C. A. (2000). A remote query magnetoelastic pH sensor. *Sensors and Actuators: B , 71*, 112-117.

9. Cai, Q. Y., Cammers-Goodwin, A., & Grimes, C. A. (2000). A wireless remote query magnetoelastic CO2 sensor. *J Environ. Monit. , 2*, 556-560.

10. Cai, Q. Y., Jain, M. K., & Grimes, C. A. (2000). A wireless, remote query ammonia sensor. *Sensors and Actuators B , 77*, 614-619.

11. *Concrete moisture meter*. (2010, March 25). Retrieved May 10, 2010, from Wikipedia: http://en.wikipedia.org/wiki/Concrete_moisture_meter.

12. Dhouibi, L., Triki, E., & Raharinaivo, A. (2002). The application of electrochemical impedance spectroscopy to determine the long-term effectiveness of corrosion inhibitors for steel in concrete. *Cement Concrete Composites , 24*, 35-43.

13. Du, R., Hu, R., Huang, R., & Lin, C. (2006). In situ measurement of Cl-concentrations and pH at the reinforcing steel/concrete interface by combination sensors. *Anal. Chem. *, 3179-3185.

14. Ervin, B. L., & Reis, H. (2008). Longitudinal guided waves for monitoring corrosion in reinforced mortar. *Measurement Science and Technology , 19* (5), 055702(19pp).

15. Fawell, J. K., Lund, U., & Mintz, B. (2003). *pH in Drinking-water.* (M. Sheffer, Ed.) Retrieved May 11, 2010, from http://www.who.int/water_sanitation_health/dwq/chemicals/en/ph.pdf.

16. Gowers, K., Millard, S., Gill, J., & Gill, R. (1994). Programmable linearPolarisation meter for determination of corrosion rate of reinforcement in concrete structures. *British Corrosion Journal , 29* (1), 25-32.

17. Grimes, C. A., & Kouzoudis, D. (2000). Remote query measurement of pressure, fluid-flow velocity, and humidity using magnetoelastic thick-film sensors. *Sensors and Actuators: A , 84*, 205-212.

18. Grimes, C. A., Kouzoudis, D., & Mungle, C. (2000). Simultaneous measurement of liquid density and viscosity using remote query magnetoelastic sensors. *Rev. Sci. Instrum. , 71* (10), 3822-3824.

19. Grimes, C. A., Kouzoudis, D., Dickey, E. C., Qian, D., Anderson, M. A., Shahidian, R., et al. (2000). Magnetoelastic sensors in combination with nanometer-scale honeycombed thin film ceramic TiO2 for remote query measurement of humidity. *J Appl. P* , 1121-1232.

20. Grimes, C. A., Mungle, C. S., Zeng, K., Jain, M. K., Dreschel, W. R., Paulose, M., et al. (2002). Wireless Magnetoelastic Resonance Sensors: A Critical Review. *Sensors , 2*, 294-313.

21. Grimes, C. A., Ong, K. G., Loiselle, K., G., S. P., Kouzoudis, D., Liu, Y., et al. (1999). Magnetoelastic sensors for remote query environmental monitoring. *Smart Mater. Struct. , 8*, 639–646.

22. Grimes, C. A., Ong, K. G., Loiselle, K., Stoyanov, P. G., Kouzoudis, D., Liu, Y., et al. (1999). Magnetoelastic sensors for remote query environmental monitoring. *Smart Mater. Struct. , 8*, 639-646.

23. Grimes, C. A., Stoyanov, P. G., Kouzoudis, D., & Ong, K. G. (1999). Remote query pressure measurement using magnetoelastic sensors. *Rev. Sci. Instrum. , 70* (12), 4711-4714.

24. Harpster, T. J., Stark, B., & Najafi, K. (2002). A passive wireless integrated humidity sensor. *Sensors and Actuators A , 95* (2-3), 100-107.

25. Hernando, A., Vazquez, M., & Barandiaran, M. (1988). Metallic glasses and sensing applications. *J Phys. E:Sci. Instrum. , 21*, 1129-1139.

26. Honeywell. (2007, July). *HCH-1000 Series*. Retrieved July 5, 2009, from http://sensing.honeywell.com/index.cfm/ci_id/146573/la_id/1/document/1/re_id/0.

27. Horton, B. E., Pereles, B. D., Ruan, C., Tan, E. L., & Ong, K. G. (2009). Wireless passive pH sensor based on magnetic higher-order harmonic fields. *Sensor Letters , 7* (4), 599-604.

28. Husain, A., Al-Bahar, S., Salam, S. A., & Al-Shamali, O. (2004). Accelerated AC impedance testing for prequalification of marine construction materials. *Desalination , 165*, 377-384.

29. Jain, M. K., Cai, Q., & Grimes, C. A. (2001). A wireless micro-sensor for simultaneous measurement of pH, temperature,and pressure. *Smart Materials and Structures , 10* (2), 347-353.

30. Jain, M. K., Schmidt, S., Ong, K. G., Mungle, C., & Grimes, C. A. (2000). Magnetoacoustic remote query temperature and humidity sensors. *Smart Mater. Struct. , 9*, 502-510.

31. Kouzoudis, D., & Grimes, C. A. (2000). The frequency response of magnetoelastic sensors to stress and atmospheric pressure. *Smart. Mater. Struct. , 8*, 885-889.

32. Lei, M., Baldi, A., Pan, T., Gu, Y., Siegel, R. A., & Ziaie, B. (2004). A hydeogel-based wireless chemical sensor. *17th IEEE International Conference on MEMS*, (pp. 391 - 394).

33. Lemos, S., Nogueira, A. R., Torre-Neto, A., Parra, A., & Alonso, J. (2007). Soil calcium and pH monitoring sensor system. *J. Agric. Food Chem. , 55*, 4658-4663.

34. Loiselle, K. T., & Grimes, C. A. (2000). Viscosity measurements of viscous liquids using magnetoelastic thick-film sensors. *Rev. Sci. Instrum. , 71* (3), 1441-1446.

35. MacDonald, D. (1991). *Evaluation of electrochemical impedance technology for detecting corrosion of rebar in reinforced concrete* . National Research Council, Washington.

36. MathWorks. (2002, July 1). *Lock in Amplifier.* Retrieved August 04, 2009, from http://www.mathworks.com/matlabcentral/fileexchange/1902-lock-in-amplifier.

37. MBH Engineering Systems. (2008 , 2October 29). *The importance of pH in food quality and production*. Retrieved May 12, 2010, from http://www.mbhes.com/ph_&_food.htm.

38. Modzelewski, C., Savage, H. T., Kabacoff, L. T., & Clark, A. E. (1981). Magnetomechanical coupling and permeability in transversely annealed Metglas 2605 alloys . *IEEE Trans. Magn , 17* (6), 2837-2839.

39. Nowak, M., Delome, N., Conseil, F., & Jacquemod, G. (2006). A novel architecture for remote interrogation of wireless battery free capacitive sensors. *13th IEEE International Conference on Electronics, Circuits and Systems.*

40. O'Handley, R. C. (2000). *Modern Magnetic Materials: Principles and Applications.* New York: John Wiley & Sons, Inc.

41. Ong, J. B., You, Z., Mills-Beale, J., Tan, E. L., Pereles, B. D., & Ong, K. G. (2008). A wireless, passive embedded sensor for real time monitoring of water content in civil engineering materials. *IEEE Sensors Journal, , 8* (12), 2053-2058.

42. Ong, K. G., Puckett, L. G., Sharma, B. V., Loiselle, M., Grimes, C. A., & Bachas, L. (2002). Wireless, passive, resonant-circuit sensors for monitoring food quality. *Photonics* , 150-159.

43. Papeschi, G., Bordi, S., Carlagrave, M., Criscione, L., & Ledda, F. (1981). An iridium-iridium oxide electrode for in vivo monitoring of blood pH changes. *Journal of Medical Engineering & Technology , 5* (2), 86-88.

44. Papeschi, G., Merigliano, S., Zaninotto, G., Baessato, M., Ancona, E., & Larini, M. (1984). The iridium/iridium oxide electrode to in vivo measurement of oesophageal and gastric pH. *Journal of Medical Engineering & Technology , 8* (5), 221 - 223.

45. Peat, J. K., Dickerson, J., & Li, J. (1998). Effects of damp and mould in the home on respiratory health: A review of the literature. *Allergy , 53* (2), 120–128.

46. Pohl, A. (2000). A review of wireless SAW sensors. *ieee transactions on ultrasonics, ferroelectrics, and frequency control , 47* (2), 317-331.

47. Pohl, A., & Seifert, F. (1996). Wirelessly interrogable SAW sensors for vehicular applications. *IEEE Instrumen. Meas. Conf.*, (pp. 1465–1468). Brussels, Belgium.

48. Reagecon. (2005, April 21). *The theory of pH measurement.* Retrieved May 04, 2010, from http://www.reagecon.com/TechPapers/phfaqv4.pdf.

49. Robinson, M. P., & Clegg, J. (2005). Improved determination of Q-factor and resonant frequency by a quadratic curve fitting method . *IEEE Transaction on Electromagnetic Compatibility , 47* (2), 399-402.

50. Roctest corrosion sensor. (n.d.). *Concrete corrosion sensor*. Retrieved January 16, 2010, from

    http://www.roctest.com/modules/AxialRealisation/img_repository/files/documents/SensCore-161010.pdf.

51. Roctest humidity sensor. (n.d.). *Concrete humidity sensor*. Retrieved November 06, 2009, from

http://www.smartec.ch/PDF/SDS%2016.1011%20SensCore%20Humidity%20and%20Temperature%20Sensor.pdf.

52. Roctest central unit. (n.d.). *Wireless central unit*. Retrieved November 6, 2009, from http://www.roctest.com/modules/AxialRealisation/img_repository/files/documents/SensCore-162011.pdf.

53. Roctest datalogger. (n.d.). *Wireless data logger*. Retrieved November 06, 2009, from http://www.roctest.com/modules/AxialRealisation/img_repository/files/documents/SensCore-162010.pdf.

54. Ruiz-Garcia, L., Lunadei, L., Barreiro, P., & Robla, J. I. (2009). A review of wireless sensor technologies and applications in agriculture and food industry: state of the art and current trend. *Sensors , 9*, 4728-4750.

55. Smith, J. P., & Hinson-Smith, V. (2006). The new era of SAW devices. *Anal. Chem. , 78* (11), 3505–3507.

56. Song, H., & Saraswathy, V. (2007). Corrosion monitoring of reinforced concrete structures - a review. *International Journal of Electrochemical Science , 2*, 1-28.

57. Spector, C. (2001, September 25). *About soil pH*. Retrieved May 10, 2010, from http://soil.gsfc.nasa.gov/soil_pH/plant_pH.htm.

58. Sridhar, V., & Takahata, K. (2009). A hydrogel-based passive wireless sensor using a flex-circuit inductive transducer. *Sensors and Actuators: A , 155* (1), 58-65.

59. Tesche, F. M., Ianoz, M. V., & Karlsson, T. (1997). *EMC analysis methods and computational models.* New York: John Wiley & Sons Inc.

60. Virginia Technologies, Inc. (n.d.). *Embedded Corrosion Instrument*. Retrieved October 5, 2009, from http://www.vatechnologies.com/eciNeed.htm.

61. Vojtko, J. (2007). Selected types of neural networks for magnetoelastic sensor error suppression. *Journal of Electrical Engineering, 58* (4), 232-235.

62. Wroblewski, W. (2005). *Field effect transistors (FETs) as transducers in electrochemical sensors.* Retrieved May 6, 2010, from http://csrg.ch.pw.edu.pl/tutorials/isfet/.

63. Wang, X. (2008). *Wireless Corrosion Sensor*. B. Sc. thesis, University of Manitoba, Winnipeg, MB, Canada.

64. Yeo, T. L., Cox, M. A., Boswell, L. F., Sun, T., & Grattan, K. T. (2006). Monitoring ingress of moisture in structural concrete using a novel optical-based sensor approach. *Journal of Physics: Conference Series , 45*, 186–192.

65. Zeng, K., & Grimes, C. A. (2004). Threshold-crossing counting technique for damping factor determination of resonator sensors. *Review of Scientific Instrument , 75* (12), 5257-5261.

66. Zeng, K., Ong, K. G., Mungle, C., & Grimes, C. A. (2002). Time domain characterization of oscillating sensors: Application of frequency counting to

resonance frequency determination. *Review of Scientific Instrument , 73* (12), 4375-4380.

67. Zheng, Z., Sun, X., & Lei, Y. (2009). Monitoring corrosion of reinforcement in concrete structures via fiber Bragg grating sensors. *Front. Mech. Eng. , 4* (3), 316–319.

68. Zou, L., Graham, A. F., Shahraam, A. V., Yu, Q., Chen, L., & Bao, X. (2004). Distributed Brillouin scattering sensor for discrimination of wall-thinning defects in steel pipe under internal pressurl. *Applied Optics , 43* (7), 1583-1588.